# POLITECNICO DI TORINO

## Master's Degree in Aerospace Engineering

Master's Degree Thesis

# Modeling of channel wall erosion in Hall Effect Thrusters

**Supervisor**

Prof. Lorenzo CASALINO

**Co-Supervisors**

Dr. Ing. Mario PANELLI

Dr. Ing. Francesco BATTISTA

**Candidate**

Matteo PASSET

10/2022

# POLITECNICO DI TORINO

## Master's Degree in Aerospace Engineering

Master's Degree Thesis

# Modeling of channel wall erosion in Hall Effect Thrusters

**Supervisor**

Prof. Lorenzo CASALINO

**Co-Supervisors**

Dr. Ing. Mario PANELLI

Dr. Ing. Francesco BATTISTA

**Candidate**

Matteo PASSET

10/2022

# Summary

Hall Effect Thrusters (HETs) are used for satellites applications, particularly orbiting at Low/Geo Earth Orbit (LEO/GEO) for telecommunications and government spacecraft because of their efficiency and competitiveness if compared to other electric propulsion devices. Furthermore, HETs have great potential because, in the future, they could be used for orbit transfers and interplanetary space missions. The erosion of HETs channel walls represents the main limiting factor of thrusters lifetime. Experimental characterization of erosion is expensive and time consuming, since thrusters lifetime is in the order of thousands of hours, hence the need of computational models which can accurately predict erosion is increasingly important. Computational tools can be a very handy tool also during the design process as it can help designers foresee how changes in the project will affect lifetime. In this thesis an effort has been put into developing an erosion model which can predict erosion in HETs using data for sputtering of Xe ions on ceramics in energy ranges close to HETs operating conditions.

In particular a brief overview of electric propulsion, focusing on HETs, is given. Erosion process, sputtering and plasma modeling, past and current erosion models will be presented. An erosion model will be developed, based on experimental data for sputtering at very low energies and at high temperature. It will be applied to a model of the SPT-100, coupled with plasma data provided by the HYPICFLU code, and results will be compared to experimental wall profiles.

The aim of this thesis is to develop an erosion model as self consistent as possible, which uses as few empirical coefficients as possible, so that it could be used to predict erosion in HETs accelerating channel without knowing a priori the erosion profiles on which to adapt the coefficients such as the Threshold Energy $E_{th}$.

# Table of Contents

# List of Tables

# List of Figures

# Acronyms

**BC**

Boundary Conditions

**BN**

Boron Nitride

**BNSiO$_2$**

Boron Nitride Silica

**CEX**

Charge Exchange

**CIRA**

Italian Aerospace Research Centre

**CP**

Chemical Propulsion

**DS**

Debye sheath

**EDF**

Energy Distribution Function

**EP**

Electric Propulsion

**GEO**

Geostationary Earth Orbit

**HET(s)**

Hall Effect Thruster(s)

**JPL**

Jet Propulsion Laboratory

**MD**

Molecular dynamics

**MPD**

Magnetoplasmadynamic Thruster

**MS**

Magnetically Shielded

**PIC**

Particle In Cell

**PPT**

Pulsed Plasma Thruster

**PPU**

Power Processing Unit

**QCM**

Quartz Crystal Microbalance

**RAAS**

Radiation Activated Adatom Sublimation

**RHS**

Right Hand Side

**SEM**

Scanning Electron Microscope

**SPT**

Stationary Plasma Thruster

**TS**

Thermal Spike

**US**

UnShielded

**VDF**

Velocity Distribution Function

# Chapter 1

# Introduction

## 1.1  Electric Propulsion History

Electric propulsion was first studied by Robert Goddard in 1906 who accelerated a working fluid, through electric power, producing thrust. Goddard noticed that despite accelerating charged particles to high velocities via an applied electric field, the tube walls remained relatively cool, in contrast to what happens with chemical propulsion. He went on to conclude that particles accelerated by electrostatic means could be the basis of a high-exhaust velocity propulsion systems.

In successive years several scientists, including Hermann Julius Oberth, proposed electric propulsion concepts for a variety of space applications predicting the mass-saving capabilities of EP as key to its future application in space propulsion and attitude control outside the atmosphere. Ernst Stuhlinger, who went on to direct NASA Marshall Space Flight Center's work on arcjets and ion propulsion systems, noted that in chemical rockets the ratio of takeoff weight to final weight after propellant consumption was 25-to-1, and argued that lighter-weight electric propulsion systems would make such planetary trips more feasible.

In the following decades the work focused on transforming ideas into quantitative conceptualizations with careful analysis. The dawning of EP can be dated back to 1949 [1], analysing the possibilities of nuclear thermal energy to generate electric power which would be used to accelerate the propellant electrostatically. By the end of the 1950s Significant electric propulsion research programs were established by almost every large rocket and aircraft firm, and by the early 1960s the first experimental ion thrusters were launched into orbit by the U.S. and Russia. The first extensive application of electric propulsion was by Russia using Hall thrusters for station keeping on communications satellites and since then over 238 Hall thrusters have been operated.

Altough being used mainly for station keeping, electric propulsion has been

successfully used in deep space as well. For instance, the Japanese used an Ion thruster to provide the prime propulsion for the Hayabusa asteroid sample return mission [2]. A remarkable example is *Deep space* 1, launched in 1998 with the main scope of testing new space technologies, which was the first mission to operate with an ion thruster. The thruster was finally turned off in 2001, having operated for 16,265 hours [3]. Another noticeable mission is $SMART - 1$, which, launched in 2003 by the Ariane-5 launcher, used a Hall Effect Thruster with Xenon as propellant, as the sole mean of propulsion [4].

In the past 30 years, electric propulsion use has been steadily growing for various different applications, from station keeping applications in order to reduce propellant mass, to use as primary propulsion in deep space. As shown in Fig. 1.1 the use of EP on small satellite has increased exponentially, implying the potential for strong near-term growth in small satellites flights that use micro-electric propulsion systems. [5]

In the coming years, as the acceptance of reliability and cost benefits grows, EP systems are set to take part in many future missions, from small satellites to interplanetary spacecrafts.
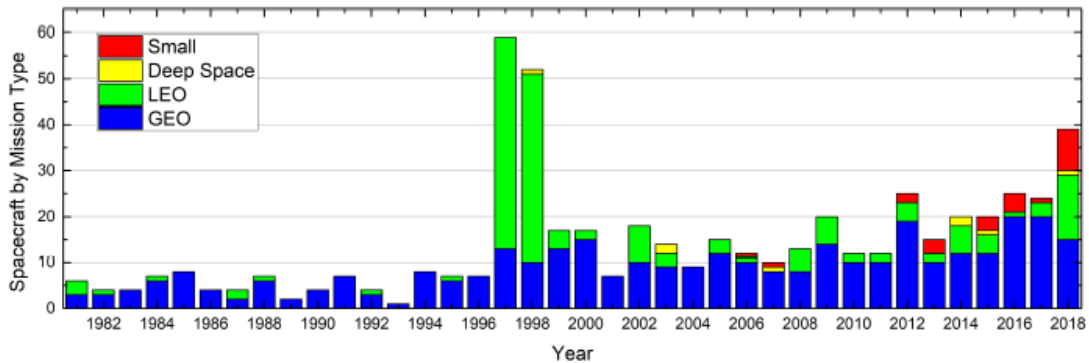


**Figure 1.1:** Number of EP-based spacecraft launched in the years 1981-2018, per mission type [5].

## 1.2 Physics Principles

The basic principle of space propulsion is to accelerate a fluid and, by the third law of dynamics, gaining momentum from it. In contrast to atmospheric propulsion, one needs to take on board all the mass which will be expelled, so great effort is put in search and development of more propellant-efficient motors, hence increasing the payload to take-off mass ratio. Assuming an isolated system, momentum conservation holds, and Newton's third law can be expressed as:

$$m\dot{v} = \dot{m}u_e \qquad (1.1)$$

where $m$ and $\dot{v}$ are the mass and acceleration of spacecraft, $\dot{m}$ is the mass flow rate of the ejected working fluid and $u_e$ is the exhaust velocity. From Newton's second law, we know that $F = ma$, and thrust being a force we have:

$$T = \dot{m}u_e \qquad (1.2)$$

It is easy to see that the greater the exhaust velocity, the greater the thrust for a given mass flow.

In chemical propulsion the working fluid, generally an oxidizer and a fuel, is accelerated via a chemical reaction. These propulsion systems are highly scalable by varying flow rate, however the exaust velocity is limited by the energy liberated in the chemical reaction as Eq. 1.3, assuming a complete reaction, shows:

$$u_e = \sqrt{2E_{ch}} \qquad (1.3)$$

where $E_{ch}$ is the chemical energy of the reaction, which depends on the reactants. Despite the low specific impulse, related to the exhaust velocity by the gravitational acceleration (1.4), they are characterized by a high thrust-to-mass ratio, which make them ideal as launchers.

$$I_{sp} = \frac{u_e}{g_0} \qquad (1.4)$$

where $u_e$ is exhaust velocity and $g_0$ is the gravitational acceleration on Earth.

In contrast, electric thrusters typically have a low thrust-to-mass ratio, coupled with a high specific impulse. EP devices make use of electrical power to accelerate a propellant by different possible electrical and/or magnetic means [6]. As EP use an external power source, there is no inherent limitation to the fluid's internal energy, hence very high specific impulses can be achieved which allow a more efficient use of propellant hence an increase of payload fraction. They are however limited by the available electrical power on board the spacecraft, therefore EP is most suitable for long duration, low thrust missions, like orbit maintenance or long term constellation flight.

Table 1.1 shows the performance range of the main thruster types.

The integration of the thrust over the total time during which the propulsion is provided defines the total impulse, which is often a mission requirement:

$$I = \int T dt \qquad (1.5)$$

For a certain total impulse $I$, a high exhaust velocity $u_e$ leads to a minor usage of propellant, as indicated in Eq. 1.6, where $m_p$ is the mass of the propellant.

| Thruster | Specific Impulse [s] | Thrust [N] |
|---|:---:|---:|
| Cold gas (CP) | 50/75 | $10^{-6}$ /3 |
| Monopropellant (CP) | 200/250 | 0.01/100 |
| Bipropellant (CP) | 300/450 | $0.01/10^7$ |
| Solid motors (CP) | 200/300 | $1/10^6$ |
| Hybrids (CP) | 215/300 | $1/10^6$ |
| Resistojet (EP) | 200/350 | 0.2/0.3 |
| Arcjet (EP) | 500/1000 | 0.2/1 |
| Ion thruster (EP) | 1000/3600 | $10^{-3}/0.2$ |
| Hall thruster (EP) | 1500/2000 | $10^{-3}/2$ |
| PPT (EP) | 600/2000 | $10^{-3}/2$ |

**Table 1.1:** Specific impulse and thrust range for different thrusters [7], [8].

$$I = I_{sp} m_p g_0 \tag{1.6}$$

Integrating Eq. 1.1 it is possible to obtain the famous Tsiolkovsky rocket equation, which relates the initial and final mass of the spacecraft ($m_0$ and $m_f$) including the mass of the rocket, casing, engine, tank, and payload, the exhaust velocity and the maximum change of velocity achievable (Eq. 1.7):

$$\Delta v = u_e \ln \frac{m_0}{m_f} \tag{1.7}$$

However, $\Delta v$ is often used as a parameter of the mission, as shown in Tab. 1.2 for various missions. It is possible to notice that, since a spiral manoeuvre is much longer than an impulsive one, the closer the mission is to the central body the greater the gravitational losses, hence a greater $\Delta v$ required. It is then useful to rewrite Eq. 1.7 in terms of mass fraction given $\Delta v$ and $u_e$.

$$\frac{m_f}{m_0} = e^{-\frac{\Delta v}{u_e}} \tag{1.8}$$

It is clear that by maximizing the exhaust velocity for a given mission, the mass fraction will be maximized. Being $m_f = m_0 - m_p$ it is possible to get Eq. 1.9 where it is possible to see that the greater $u_e$ the smaller the propellant mass, hence grater payload [9].

$$m_p = m_0(1 - e^{-\frac{\Delta v}{u_e}}) \tag{1.9}$$

| Mission | $\Delta v$, $\frac{km}{s}$ |
|---|---|
| Escape from Earth surface (impulsive) | 11.2 |
| Escape from 480 km orbit (impulsive) | 3.15 |
| Escape from 480 km orbit (spiral) | 7.593 |
| Earth to Mars (impulsive) | 5.5 |
| Earth to Mars (spiral) | 6 |
| Earth orbit to Mars orbit and return* | 14 |
| Earth surface to Mars surface and return* | 34 |
| Earth orbit to Venus orbit and return* | 16 |
| Earth orbit to Mercury orbit and return* | 31 |
| Earth orbit to Jupiter orbit and return* | 64 |
| Earth orbit to Saturn orbit and return* | 110 |

**Table 1.2:** Characteristic velocity increments for planetary transfer missions (*Hohmann's maneuver) [9].

One could now argue that the main focus should then be on producing motors with the highest possible $u_e$, but there is catch: the faster the propellant is accelerated the grater the energy required. Since in the final mass in Eq. 1.8 is included, in case of EP, the power source used to generate the energy to accelerate the propellant, the remaining payload would tend to zero. It is possible to consider this aspect through the energy conversion efficiency of the thruster $\eta$ and the specific mass of the power generation system $\alpha$ [9]:

$$\eta = \frac{\dot{m}u_e^2}{2P} = \frac{u_e T}{2P} \tag{1.10}$$

$$\alpha = \frac{m_{ps}}{P} \tag{1.11}$$

Where the product between $\dot{m}$ and $u_e$ represent the propulsive power, $P$ is the electric power and $m_{ps}$ is the weight of power system.

From Eq. 1.10 and Eq. 1.11, it is possible to get an expression of $m_{ps}$ as function of the specific impulse, being $u_e = I_{sp}g_0$:

$$m_{ps} = \alpha P = \frac{\alpha T g_0 I_{sp}}{2\eta} \tag{1.12}$$

Rewriting in term of the specific impulse depending on $\alpha$, $\eta$ and $\Delta t$ (mission time):

$$I_{sp} = \frac{1}{g_0}\sqrt{\frac{2\eta\Delta t}{\alpha}} \qquad (1.13)$$

or exhaust velocity:

$$u_{e_{opt}} = \sqrt{\frac{2\eta\Delta t}{\alpha}} \qquad (1.14)$$

There is an optimal value of exhaust velocity, or specific impulse, that maximizes the payload mass, as shown in Fig. 1.2, that depends on the power system, thruster's parameters, and mission time, but is independent of the thrust [9].
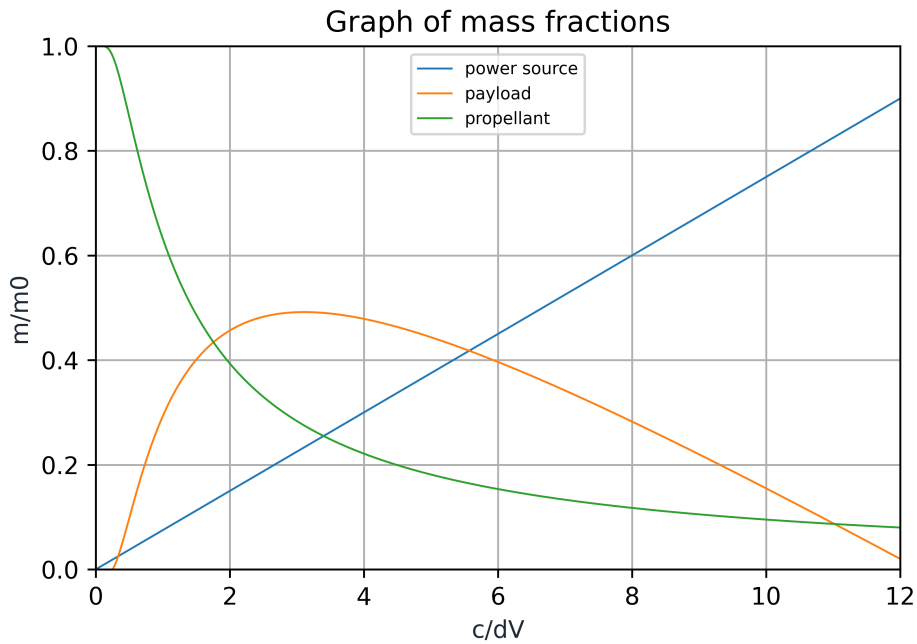


**Figure 1.2:** Optimal specific impulse, plotted in python.

## 1.3 Electric Thrusters' Classification

Electric thrusters can be divided into three different categories, based on the acceleration method used to produce thrust: electrothermal, electrostatic, and electromagnetic. In the following, common EP types are described [2], [8], [10]. In Fig. 1.3 is reported the number of EP-based GEO satellites launched in the past years, where it is possible to see the increasing adoption of Hall thrusters, which are the subject of this study [5].
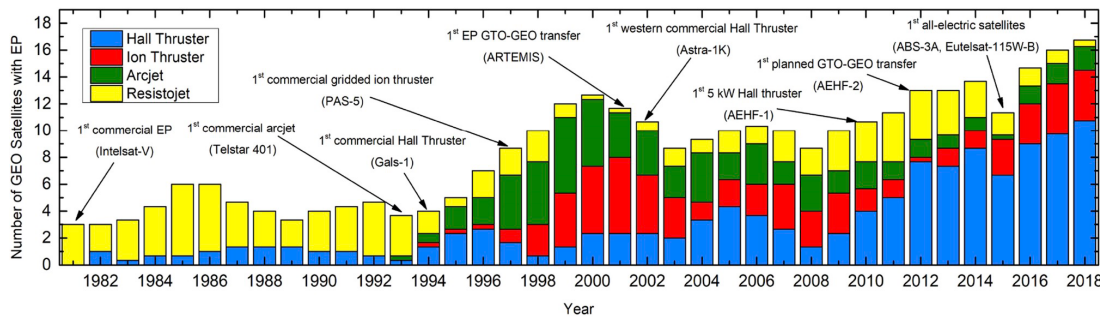
**Figure 1.3:** Number of EP-based GEO satellites launched in the years 1981–2018, divided into electric thruster subclasses [5].

### 1.3.1 Electrothermal

In the electrothermal thruster, the propellant is heated by electric power and then is accelerated through a conventional converging-diverging nozzle to convert the acquired energy into kinetic energy producing thrust. Typically, electrothermal thrusters are resistojets and arcjets.

In resistojets the propellant is heated by passing through a resistively heated chamber or over a resistively heated element before entering a downstream nozzle, therefore the specific impulse is limited by the material heating. Arcjets bypass this limit by heating the propellant via an high current arc in line with the nozzle feed system, which allows to reach higher propellant temperature.

Specific impulse is comparable to that achieved by chemical devices given that both systems are limited by the working temperature limit of the material. Specific impulse is limited to less than 500 s for resistojets and to less than about 700 s for arcjets.

### 1.3.2 Electrostatic

In electrostatic thrusters, plasma generation is used to ionize a large fraction of the propellant. The positively charged ions are then accelerated by an electrostatic field and at the exit of the thruster, are neutralized by a negative particle beam. Two main propulsion types fall in this category: gridded-ion and Hall effect thrusters.

Gridded-ion thrusters accelerate ions via electrostatic grids at voltages up to and exceeding 10 kV. Modern gridded-ion thrusters utilize noble gases as propellant. The thrust density is constrained by space-charge limitations (Child-Langmuir law), and the grid is subject to erosion by impingement of charged particles.

Hall effect thruster is probably the most successful in-space EP technology by quantity of units flown. They utilize a cross-field discharge described by the Hall effect to generate the plasma. The axial electrostatic field accelerate the ions to

high velocities, while the radial magnetic field inhibits electron motion that would tend to short out the electric field. HET are characterized by a simpler design than gridded-ion, have good efficiency, high specific impulse and higher thrust-to-weight ratio as they are not subject to space-charge limitations.

### 1.3.3 Electromagnetic

In electromagnetic thrusters the propellant is ionized and accelerated using a combination of electric and magnetic forces. There are two main types of electromagnetic thrusters: Pulsed Plasma Thrusters (PPT) and Magnetoplasmadynamic thrusters (MPD).

In PPT a pulsed discharge is used to ionize a small fraction of a solid propellant ablated into a plasma arc, and electromagnetic effects in the pulse to accelerate the ions to high exit velocity. MPDs use a very high current arc to ionize the propellant. Then electromagnetic forces accelerate the charged propellant. Often both current and magnetic field are generated by the plasma discharge, so MPD use very high power to generate sufficient force for high specific impulse, thereby they generate high thrust compared to other EP systems.

In table 1.3 are shown the above mentioned EP system's performance parameters.

| | Resistojet | Arcjet Thruster | Ion | HET | MPD | PPT |
|---|---|---|---|---|---|---|
| | $(N_2H_4, Xe)$ | $(N_2H_4, NH_3)$ | $(Xe)$ | $(Xe)$ | $(Ar, H_2, L)$ | Teflon |
| Power range, [W] | 500-1500 | 300-2000 | 200-4000 | 300-6000 | 1-100K | 1-200 |
| $I_{sp}$, [s] | 100-300 | 500-600 | 3000 | 1600 | 2000-10000 | 500-1500 |
| $\eta$ | 80% | 35% | 65% | 50% | 50% | 7% |
| Peak Voltage [V] | 28 | 100 | 900 | 300 | 200 | 1K-2K |
| Thruster mass, [kg/kW] | 1-2 | 0.7 | 3-6 | 2-3 | - | 120 |
| PPU mass, [kg/kW] | 1 | 2.5 | 6-10 | 6-10 | - | 110 |
| Lifetime, [h] | 500 | >1000 | 30000 | >7000 | 1000 | $10^7$pulse |

**Table 1.3:** Typical performance parameters of electric thrusters [10], [11].

## 1.4 Plasma Physics

Plasma is an electrically conducting medium composed of roughly equal numbers of positively and negatively charged particles, which exibits a collective behaviour, produced when the atoms in a gas become ionized, that is they lose (or gain) an electron. It is sometimes referred to as the fourth state of matter, distinct from solid, liquid and gaseous state [12]. Because of the presence of free charges, Plasma

is a good conductor where electrons move faster than ions, creating difference in potential.

Plasmas do not usually occur naturally at the surface of the Earth, therefore must be produced artificially. Plasma may be produced by direct application of heat for atoms with low ionization energies, via chemical reactions or application of electric fields. A convenient unit for measuring temperature in the study of plasmas is the electron volt (eV), which is the energy gained by an electron in vacuum when it is accelerated across one volt of electric potential. It is possible to distinguish between low and high temperature plasmas, where the temperature usually refers to the temperature of the electrons. In the case of EP devices like gridded-ion and Hall Effect thrusters, we regard low temperature plasma, with electron temperature in the region of $eV$, corresponding to tens of thousands of Kelvin, sufficient to trigger dissociation and ionization. Heavy species temperature, however, is close to room temperature [13].

## 1.4.1 Plasma characteristics

The energy in a plasma is stored in the movement of the plasma species, according to their degrees of freedom, each of which is described by a *distribution function* which, for an homogeneous plasma in space, corresponds to the Maxwell-Boltzmann distribution (Eq. 1.15), representing the probability to find a single species at a specific location in space in the plasma to exhibit a specific energy.

$$f(v) = \left( \frac{m}{2\pi k_B T} \right)^{3/2} exp \left( \frac{\frac{1}{2}mv^2}{k_B T} \right) \tag{1.15}$$

From the distribution function it is possible to calculate the average energy of a particle as:

$$\langle E \rangle = \frac{\int \frac{1}{2}mv^2 f(v) d^3v}{\int f(v) d^3v} = \frac{3}{2} k_B T \tag{1.16}$$

In most low temperature plasmas one has to characterize different species with several distribution functions at different temperatures.

Another fundamental characteristic of a plasma is its ability to shield out electric potentials that are applied to it. Electrons and ions cannot move independently from each other, as any separation is counteracted by the electric field that is formed. A plasma remains in a so-called *quasineutral* state as a whole, that is the overall electric potential is small. To small enough distance, called *Debye lenght*, $\lambda_D$, the differently charged particles in the plasma may cause a deviation from the quasineutral potential, as shown in Fig. 1.4.

Considering a sphere of electrons forming around the ions, the radius of the sphere, out of which the shielding would not be complete, is approximately where
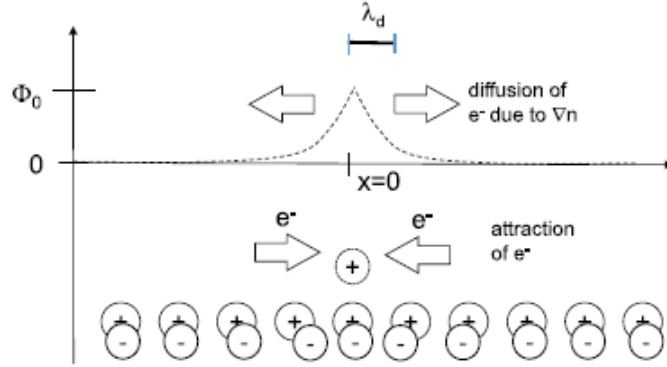
**Figure 1.4:** Response of the plasma to an additional positive charge at $x = 0$ [13].

the potential energy equals the thermal energy of the particles [14]. The length scale of this disturbance is $\lambda_D$. In more rigorous terms, the *Debye lenght* is represented by Eq. 1.17, where $\epsilon_0$ is the permittivity of air, $k_B$ is the Boltzmann constant, $T_e$ is the electron temperature, $e$ is the charge of the electron and $n$ is the charge density.

$$\lambda_D = \sqrt{\frac{\epsilon_0 k_B T_e}{e^2 n}} \tag{1.17}$$

The *Debye length* describes the smallest length scale of a volume to confine a plasma, defining the transition from plasma collectivity to individual particle behaviour.

## 1.5 Particles motion

Plasma is difficult to analyze as its density falls in an intermediate range. The transport of species can be either described by the *single particle picture*, where the movement of species is described using Newton's law of motion, or by a *fluid picture*, where the transport is described as the movement of a fluid element consisting of an ensemble of particles [13]. In this section will be considered the motion of charged particles in the presence of prescribed electric and magnetic field, assumed not to be affected by the charged particle motion itself [14].

The movement of species with charge $q$, mass $m$, under the influence of electric $E$ and magnetic $B$ fields is described by the Lorentz force:

$$m\frac{dv}{dt} = q(\mathbf{E} + \mathbf{v} \times \mathbf{B}) \tag{1.18}$$

The presence of an external applied magnetic field allows the creation of high performance plasma and for an excellent confinement of the plasma species, as

10

their movement is bound by the magnetic field lines. This magnetic confinement can be different for electrons and for ions, as it will be shown in the next section.

### 1.5.1   Uniform E and B fields

Let's first consider the presence of a uniform and constant magnetic field **B** and a negligible electric field **E**. Equation 1.18 will simplify into:

$$m\frac{dv}{dt} = q\mathbf{v} \times \mathbf{B} \tag{1.19}$$

The charged particle will follow a simple gyration motion, called *cyclotron gyration*, which frequency (*cyclotron frequency*) is defined as:

$$\omega_c = \frac{|q|\mathbf{B}}{m} \tag{1.20}$$

The *Larmor radius* is defined as:

$$r_L = \frac{v_\perp}{\omega_c} = \frac{mv_\perp}{|q|\mathbf{B}} \tag{1.21}$$

It must be noted that both the frequency and radius depend on the mass of the particle. This property is used in HET to confine electrons for better ionization, as we shall see in future chapters. The movement of the charged species consist of a circular motion around a fixed *guiding center*. The motion has a diamagnetic character, that is the particles will orbit in a way that their movement will cause an opposing magnetic field, as illustrated in Fig. 1.5.
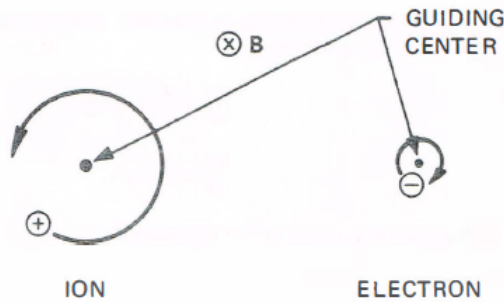


**Figure 1.5:** Larmor orbits in a uniform magnetic field [14].

In addition to this motion, there might be an additional velocity along **B** which is not affected by **B**. This causes a translation of the guiding center, and the resulting motion is, in general, a helix, as shown in Fig. 1.6
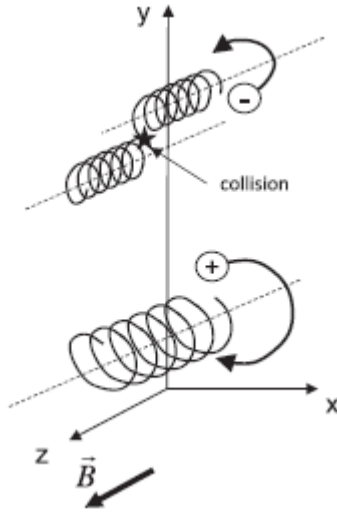
**Figure 1.6:** Larmor orbits in a uniform magnetic field [13].

Let us now consider the presence of a finite electric field $\mathbf{E}$ lying perpendicular to $\mathbf{B}$. The motion will now be a combination of the Larmor gyration plus a drift of the guiding center in the direction $\mathbf{E} \times \mathbf{B}$. The latter motion, called *drift velocity*, can be expressed by the following formula:

$$v_{\mathbf{E}\times\mathbf{B}} = \frac{\mathbf{E} \times \mathbf{B}}{\mathbf{B}^2} \tag{1.22}$$
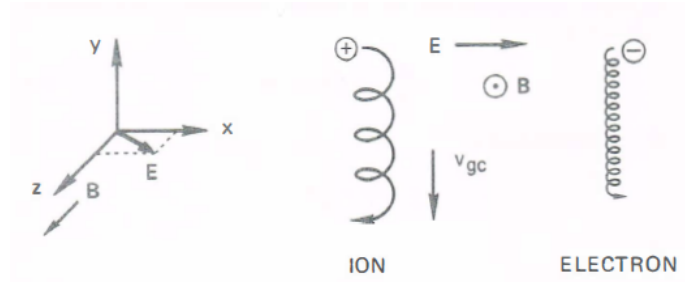


**Figure 1.7:** Particle drifts in crossed electric and magnetic fields [14].

It is important to note that the drift velocity describes only the movement of the guiding center and is independent of the charge $q$, the mass $m$ and the velocity perpendicular to $\mathbf{B}$, $v_\perp$, hence both electrons and ions will move in the same direction (Fig. 1.7).

## 1.5.2   Nonuniform B field

Let's now consider a magnetic field **B** which magnitude varies along its direction (Fig. 1.8). A longitudinal field gradient occurs, hence the magnetic field lines thicken in regions of higher magnetic field. Since the lines of force converge or diverge, there is necessarily a radial component of **B**. This gives rise to a force which can trap a particle in a magnetic field, generating the so-called *magnetic bottle* or *magnetic mirror*.
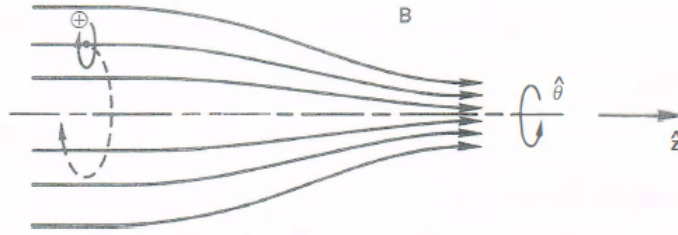


**Figure 1.8:** Non uniform magnetic field [14].

For simplicity, consider a single particle whose guiding center lies on the axis. The tangential velocity is a constant during a gyration, and, depending on the sign of the charge $q$, corresponds to $|v_\perp|$. The conservation of magnetic moment and kinetic energy conservation hold. We define the *magnetic moment* of the gyrating particle to be:

$$\mu = \frac{1}{2}\frac{mv_\perp^2}{\mathbf{B}}$$ (1.23)

As a particle moves in a region of stronger magnetic field, for instance, the *Larmor radius* (Eq. 1.21) will decrease, but in order to keep $\mu$ invariant $v_\perp$ must also increase. The total energy of the particle must remain constant, hence, by Eq. 1.24, $v_\parallel$ (the velocity parallel to the field lines) must necessarily decrease. The opposite would happen for a particle moving toward a decreasing **B**.

$$v_\perp^2 + v_\parallel^2 = v_{\perp 0}^2 + v_{\parallel 0}^2 = v_0^2$$ (1.24)

In other words, a single charged particle moving from a weak magnetic field to a stronger one would slow down until, if it encounters a strong enough **B**, a complete stop. Then particle would then be reflected back to the weaker magnetic field, hence the name *magnetic mirror*.

This phenomenon is at the basis of plasma confinement, as schematically shown in Fig. 1.9. It is strongly dependent on the angle of incidence $\theta$ of the particle with respect to the magnetic flux vector and on the magnetic field strength. If $\theta$ is too
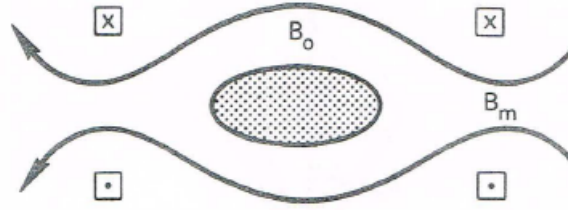
**Figure 1.9:** A plasma trapped between magnetic mirrors [14].

small, or **B** not strong enough, the particle will not be trapped. This limit can be represented by the so-called *loss cone*, represented in Fig. 1.10. The boundary of the cone can be represented by the following formula:

$$\sin^2 \theta_m = \frac{B_0}{B_m} = \frac{1}{R_m} \tag{1.25}$$

Where $B_0$ and $B_m$ are respectively the magnetic field strength in the region of lowest and maximum intensity, and $R_m$ is defined as the *magnetic mirror ratio*.
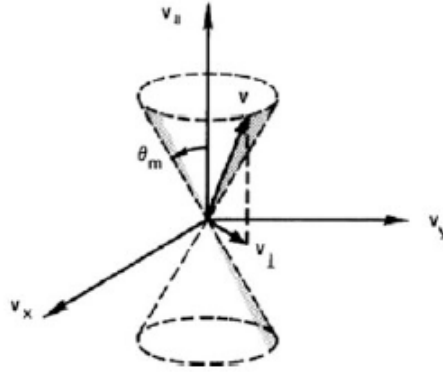


**Figure 1.10:** The loss cone [14].

14

# Chapter 2

# Hall Effect Thruster

Hall Effect Thrusters (HET) are a specific type of electric propulsion which use a combination of an electric (**E**) and magnetic (**B**) field. In particular, HETs are characterized by an annular channel with an interior anode, a magnetic circuit that generates a primarily radial magnetic field across the channel, and a cathode external to the channel. The cathode emits electrons, which, being outside of the motor, generate a drop in potential thus producing an axial electric field, as schematically shown in Fig. 2.1, with the two possible cathode positions.



**(a)** Outer hollow cathode [2]    **(b)** Central hollow cathode [8].
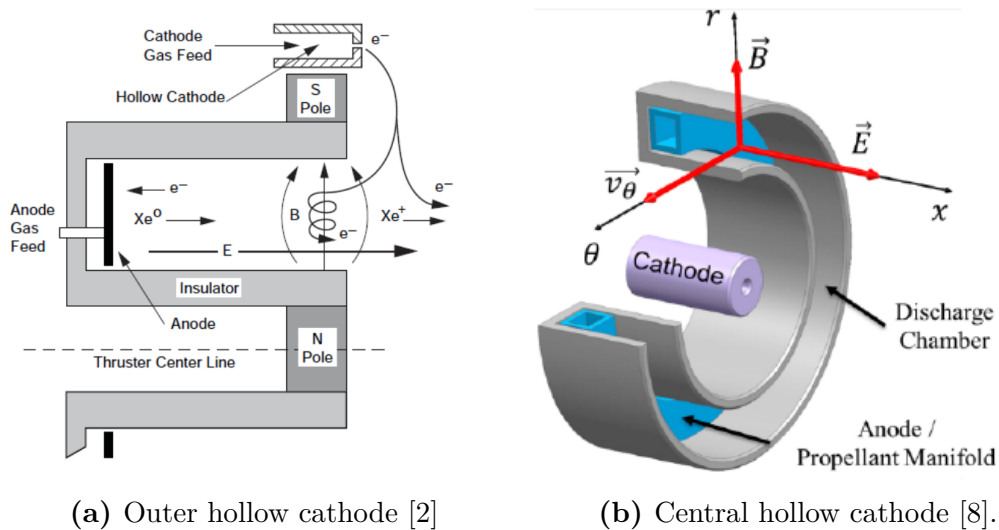
**Figure 2.1:** Hall Effect Thrusters schematic.

Despite **B** being critical for the correct operation of the motor, HETs are considered electrostatic devices as ions are accelerated by the applied electric field. However, since the acceleration occurs in the plasma region near the channel exit,

space charge density is not a limitation, and can reach higher thrust densities than gridded-ion motors [2].

A neutral propellant, often xenon, is injected from the anode at the base of the channel. The hollow cathode emits electron, a fraction of which enters the chamber and ionizes the propellant via collisions with neutral atoms, the other part goes on to neutralize the ions in the plume. The magnetic field strength is such that electrons become magnetized and trapped in a closed azimuthal Hall drift at about the thruster centerline [15]. They then diffuse by collisional processes and electrostatic fluctuations to the anode and channel walls. A schematic value of the radial magnetic field $B_r$ and axial electric field $E_z$ is shown in Fig. 2.2.
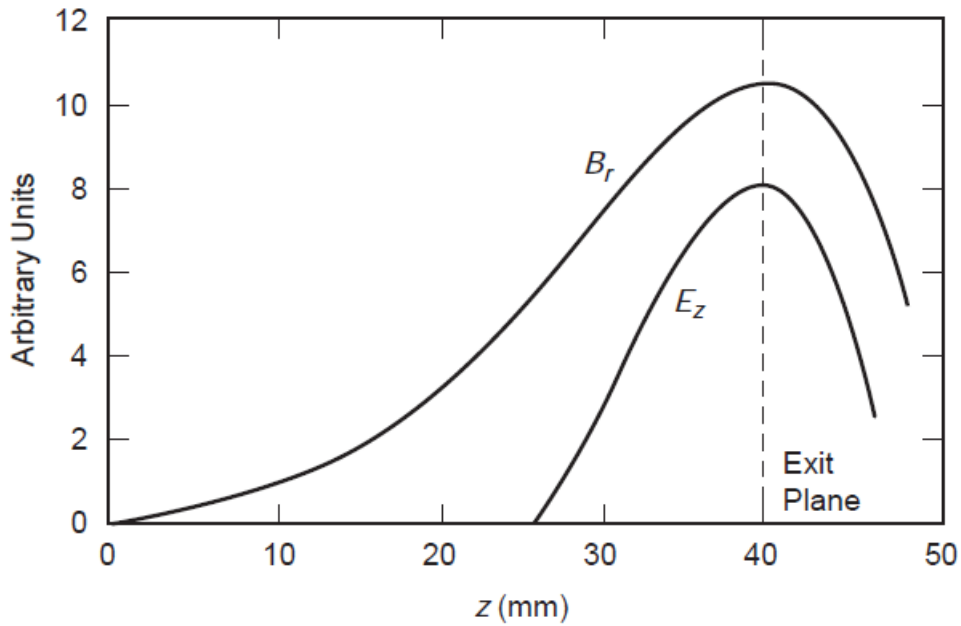


**Figure 2.2:** Typical HET axial electric field and radial magnetic field along the channel length [2].

The radial magnetic field typically is maximum near the thruster exit plane, and it is designed to fall near zero at the anode in dielectric-wall Hall thrusters. Due to the reduced electron mobility and high electron temperature in the region of strong magnetic field, the axial electric field is also maximized near the exit plane.

For the correct confinement of the electrons, and reduced mobility to the anode, their Larmor radius (see Eq. 1.21) must be less than the characteristic length $L$:

$$r_{e,L} = \frac{v_{th}}{\omega_{c,e}} = \frac{m_e}{qB}\sqrt{\frac{8K_B T_e}{\pi m_e}} << L \qquad (2.1)$$

16

where $r_{e,L}$ is the Larmour radius of electrons, $v_{th}$ is the velocity of electrons due to their thermal motion, $\omega_{c,e}$ is the electron cyclotron frequency, $m_e$ is the mass of electrons, $K_B$ is the Boltzmann constant while $L$ is the depth of the acceleration channel. Electrons must also be considered magnetized, that is they make many orbits around a field line before a collision with an ion or neutral atom occurs resulting in a cross-field diffusion. This can be described by the *Hall parameter* (Eq. 2.2) which considers the total collision frequency $\nu$ and the cyclotron frequency $\omega_c$. For electrons to be magnetized $\Omega_c$ must be large compared to unity [2].

$$\Omega_e = \frac{\omega_c}{\nu} \tag{2.2}$$

Meanwhile, the Larmor radius of the ions is much greater, due to their greater mass, hence are not be affected by the magnetic field and can be accelerated out of the channel by the electric field. A schematic representation of the ionization and acceleration region is shown in Fig. 2.3. The ions Larmor radius therefore needs to be greater than the channel depth:

$$r_{i,L} = \frac{v_i}{\omega_{c,i}} = \frac{M}{qB}\sqrt{\frac{2qV_b}{M}} >> L \tag{2.3}$$

where the ion energy is approximated as the beam energy, $M$ is the ion mass and $V_b$ represent the potential through which the ions are accelerated. The average velocity of the ion beam can be expressed as:

$$v_i = \sqrt{\frac{2qV_b}{M}} \tag{2.4}$$
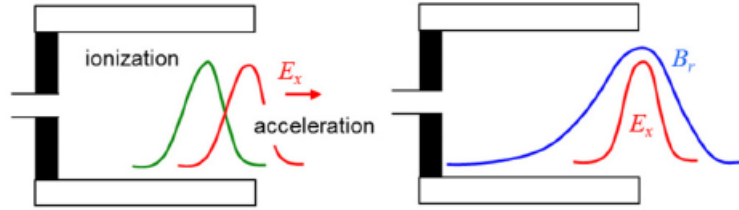


**Figure 2.3:** Schematic representation of the acceleration and ionization regions and of the radial magnetic field profile [16].

Since ionization is mainly due to electron-neutral collisions, there is no need for an ionization device. The axial electric field generated inside the plasma thanks to the magnetic field, means there is no need for an acceleration grid which brings two advantages: the absence of the grid saves weight, and the absence of the grid means no need for a Power Processing Unit (PPU) which in turn saves weight [17].

## 2.1  Plasma oscillations

Numerous oscillations and instabilities have been detected in Hall thrusters, in a large frequency range, from kHz to tens of MHz. These oscillations have been studied with powerful diagnostic techniques [16]. The amplitude and frequencies of observed oscillations were found to be strongly dependent on operating conditions [18]:

- mass flow rate and propellant type;

- applied voltage;

- initial and time-evolving geometry;

- degree of contamination of the discharge chamber;

- cathode characteristics (mass flow rate and location);

- PPU characteristics and configuration;

- the magnetic field profile and magnitude.

In the following a very brief description of the various type of oscillation is given [16], [18].

*Ionization oscillations* are low frequency oscillations. Due to strong ionization of the atom flow in the large magnetic field region, the neutral atom front moves upstream (toward the anode) in a lower magnetic field region where ionization is less efficient because the electron mobility is larger. This leads to a decrease of the current till the neutral atom front moves back to the exhaust region where intense ionization can take place again. This oscillation, also called *breathing mode*, should be related to the time necessary for neutral atoms to replenish the ionization region.

There are azimuthal oscillations in the low-medium frequency range, due to different reasons however. The low frequency oscillations act as rotating spokes and are related to ionization processes in the anode region. Are characterized by regions of higher plasma emission rotating at high velocities. Higher frequency azimuthal modes, or gradient-iduced oscillations, are caused by drift-type instabilities associated with the gradients of density and magnetic field. They typically appear in the exhaust region, where the magnetic field is stronger.

Higher frequency axial oscillations, called in fact *axial transit time oscillations*, are associated with the transit time of ions in the acceleration region. Their amplitude distribution over the channel strongly depends on the profile of the radial magnetic field. In particular, they are quasi-axial electrostatic waves, tend

18

to be relatively turbulent and are presumed to play an important role in regulating the plasma transport.

One more instability, characterized by large amplitude, small wavelength azimuthal oscillations of the azimuthal electric field, called *E × B electron drift instability*, is the result of the coupling between electron Bernstein waves and ion acoustic waves. This instability is present in the acceleration region, and seems to contribute significantly to anomalous electron transport.

## 2.2   Plasma-wall interactions

A very important aspect for HETs is the interaction of the plasma, both as a fluid and as single particles, with the walls of the thruster. Due to a phenomenon called *sputtering*, highly energetic particles may collide with the walls eroding it. During operation the erosion goes on exposing the electrodes and ultimately ending the thruster's life. The next two sections will explain the process in more details.

An interesting aspect of plasma-wall interaction is that surfaces act both as sink, when an ion hits the surface and is retained on it for a time sufficiently long to recombine with the electrons, and sources for the plasma as the newly formed neutrals are usually weakly bounded to the surface, and are re-emitted into the plasma. Subsequently, these neutrals can be re-ionized, generally by electron impact. The re-ionization process can take place close to the surface of further into the plasma bulk [19].

A second effect caused by the presence of a surface is the formation of the plasma sheath, as described in the next section.

### 2.2.1   Plasma sheath

Quasineutrality of the plasma, as introduced in chapter 1, can be considered true in the bulk of the plasma where if any charge imbalance were to happen at a certain time in the bulk of a plasma, the surrounding charges would rapidly act to exclude the charge imbalance and limit its electromagnetic field to a length comparable with the Debye length $\lambda_D$. However, in any plasma bounded by surfaces, a ceramic insulator in HETs walls, this quasineutrality is violated in close proximity of the wall and a space charge region with a very high electric field, the plasma boundary sheath, or *Debye sheath* [19], is formed [13]. Ions and electrons hit the wall at different speeds, related to their thermal velocities. Since electrons have a much higher speed, due to their lower mass, they are lost to the walls faster, leaving the plasma with a net positive charge. At the same time a negative charge develops on the wall, so an electric field builds up in that region until the equilibrium of electron and ion fluxes towards the surface is established (Fig. 2.4). The function

of a sheath is to form a potential barrier so that the more mobile species, usually electrons, is confined electrostatically [14].
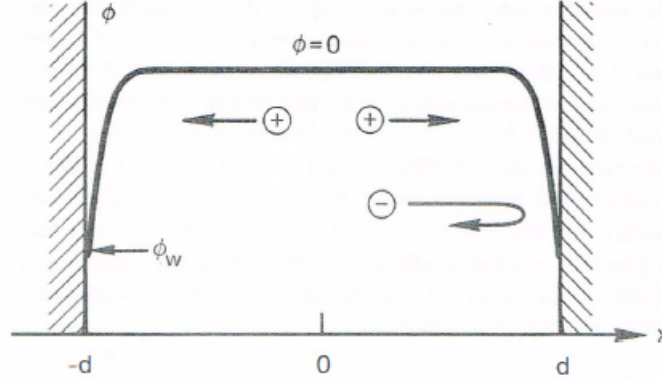


**Figure 2.4:** Plasma potential $\phi$ forms sheaths near the wall so that electrons are reflected. The potential barrier adjust itself so that equal numbers of ions and electrons reach the walls per second [14].

The *Debye sheath* (*DS*), essentially collisionless, cannot be directly connected to the unperturbed plasma. It is preceded by a quasineutral region, characterized by collisions and ionization, called the *presheath*. The role of the *presheath* is to accelerate the ions to a critical velocity at the entrance of the *DS*. Such a condition is called the *Bohm's criterion* and is a conerstone of plasma-wall interactions.

The violation of quasi-neutrality in the sheath requires the use of Poisson's equation for its description. Assuming that the potential energy is small, the linearized Poisson's equation becomes:

$$\frac{\partial^2 \phi}{\partial x^2} = \frac{1}{\lambda_D^2} \left( 1 - \frac{k_B T_e}{M_i u_0^2} \right) \phi \tag{2.5}$$

where $M_i$ and $u_0$ are respectively the mass and velocity of ions.

The solution of Eq. 2.5 is an exponential function with a characteristic decaying length close to the Debye length. The potential drop will be appreciable in a region of thickness $\lambda_D$ in front of the wall, hence the name *Debye sheath* [19]. A monotonically decreasing potential has, therefore, to be found towards the wall, as shown in Fig. 2.5 where ion and electron densities are shown, along with the potential close to the wall.

This translate to the so-called *Bohm criterion* (Eq. 2.6) which states that the ion mean velocity at the entrance of the sheath must be larger than the acoustic velocity $c_s$ (assuming ions temperature negligible as $T_e \gg T_i$), in the order of few km per seconds, much higher than the thermal velocity of ions. This velocity needs to be acquired before the entrance in the sheath, therefore a finite electric field
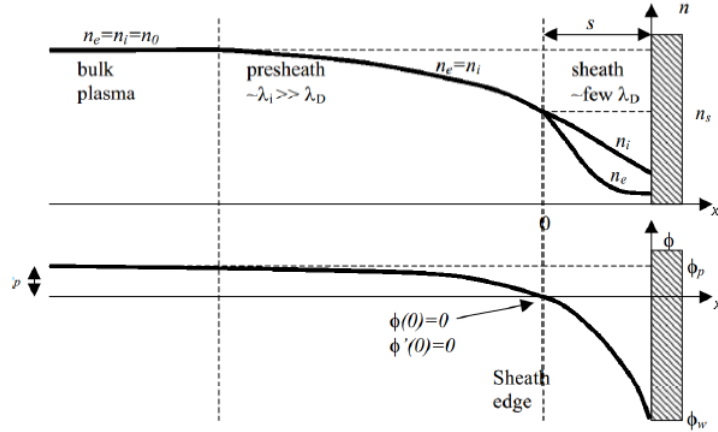
**Figure 2.5:** Two region model of plasma behaviour near walls [20].

is needed to act before it. The boundaries of the acceleration region, namely the *presheath*, are not well defined and might extend to the entire plasma.

$$u_0 \geq \sqrt{\frac{k_B T_e}{M_i}} \equiv c_s \tag{2.6}$$

## 2.2.2   Ion flux to walls

Vrebosch *et al.* [21] developed an erosion model where the ion flux to the walls depends on the three known mechanisms. In particular the program allows the evaluation of erosion via the three mechanisms, used individually or combined. They analyzed the contribution of the individual erosion mechanisms in order to determine the most influencing one. The result is reported in Fig. 2.6.

Ion flux to the channel walls is a combination of the three following mechanisms:

- *Sheath effect*: it is basically what has been presented in section 2.2.1. At the insulating boundaries of the channel a negative potential forms due to the flux of the more mobile species (electrons) which repels electrons and attracts ions, until the flux is balanced. Through the sheath ions continue to accelerate, until they reach the wall surface, on which they impact transferring their momentum and eroding the surface. This process will be further discussed in the next section. *Sheath effect* accounts as the dominant factor in the erosion process.

- *Particle scattering*: despite plasma being almost collisionless, collisions may occur between ions and neutral, while being accelerated, on the way out of the channel. After colliding they divert and may hit the channel walls, eroding

it. The number of particles that are scattered depends on the collision cross section, which is a factor on the particles relative velocity and their size. As seen in Fig. 2.6 this accounts for barely 5% of the global erosion rate, which is almost negligible, especially after few hundreds of hours of operation.

- *Flow divergence due to magnetic field*: this effect can arise from a misalignment of the magnetic field. Since equipotential lines tend to align themselves to the magnetic field lines, and the electric field is orthogonal to the equipotential lines, the ion beam will diverge towards the exit if the magnetic field is not aligned. Such divergence may cause ions to impact the surface, ultimately wearing it away. This problem does not present if the thruster's circuit is properly designed, hence often is considered as negligible and not taken into account.
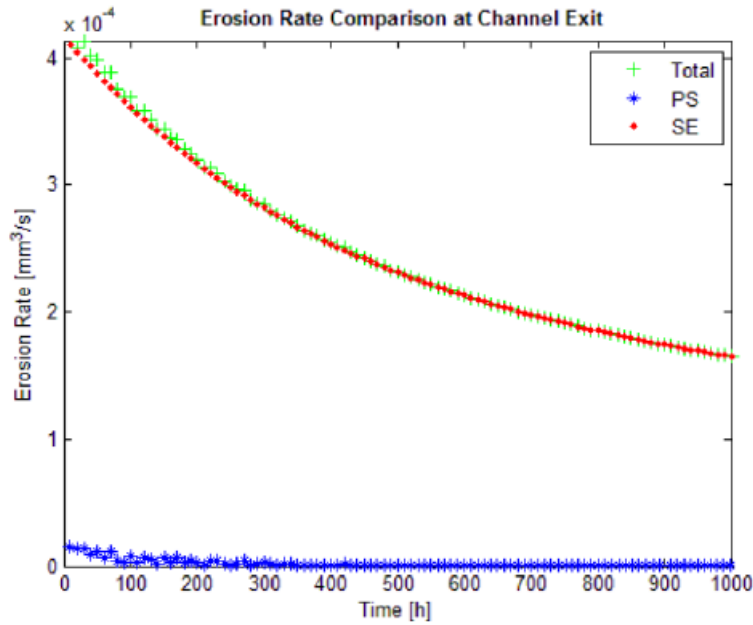


**Figure 2.6:** Erosion rate contribution for Particle Scattering (PS) and Sheath Effect (SE) to total erosion. [20]

## 2.2.3 Sputtering

In previous sections sputtering was introduced as the main factor influencing erosion. Sputtering will now be analyzed in more depth.

Sputtering is the ejection of microscopic particles from a surface of a solid material via bombardment of highly energetic particles, generally ions of noble

gases, such as Argon or Xenon.In some cases, as for Hall Effect Thrusters, sputtering is detrimental since components that are subject to it will erode, ultimately causing the end of life of the component, as exposed before. However, in can be used in proactive ways in science and industry - can be used to clean samples for surface analysis, for surface analytical methods (i.e. secondary ion mass spectrometry), and to deposit thin film layers in the manufacture of optical coatings, semiconductor devices and nanotechnology products. An extensive overview of the aforementioned process can be found in the overview paper by Smentkowski *et al.* [22]. Sputtering is best described by the *Sputtering yield*, which is the quantity of material removed per incident ion. Sputtering occurs when incident ions, given enough energy, collide with the solid surface and the energy they carry is spent to break the bond between target atoms, leading to their removal. This process, which is dominant for sputtering with low ion energies (<10 keV) [22], takes place via three fundamental mechanisms of energy transfer, as schematically shown in Fig. 2.7. Direct knock-on (Fig. 2.7a) happens when the incoming particle directly knocks out a target atom from the surface. Figure 2.7b shows the removal of an atom via impact of the particle on a neighboring atom. Similarly, linear cascade regime occurs when the incident particle initiates a collision cascade through the material, and sputtered atoms are ejected via secondary recoil (Fig. 2.7c).



**(a)** Direct knock-on regime   **(b)** Single recoil regime   **(c)** Linear cascade regime
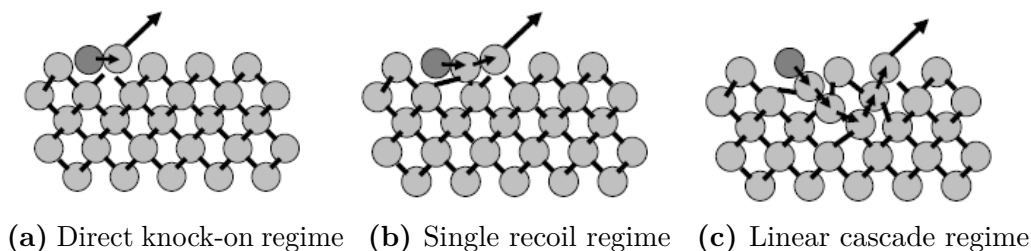
**Figure 2.7:** Energy transfer mechanisms during sputtering [23].

The exact means by which atoms are sputtered can be very complex and depend on a variety of factors, and sputtering by all three mechanisms may happen concurrently, hence the sputter yield is used to describe their net effect.

Different ways have been used over the years to experimentally measure sputtering yield. The classical method consists in weighing the target before and after sputtering and to calculate the change in target mass. Others have placed the sample to be sputtered onto a quartz crystal microbalance (QCM) and measured the change of resonant frequency during sputtering as matter gets deposited on it. Also direct determination of crater volume via optical profilometry can be used to determine sputtered material. Many elements are to be taken into account to minimize erroneous readings, such as performing tests under ultra high vacuum conditions, a stable and well-characterized ion source and a precise measurement of

the beam current striking the surface. An ion source with known energy distribution and orientation is essential to characterize the dependence of sputtering with angle.

Computational modeling of sputtering has been performed using molecular dynamics and binary collision approximation codes, which are able to simulate ion bombardment in solids. Using these methods, effects on sputtering of lattice structure of solids, different incident angle, and species can be studied.

Sputtering yields of monoatomic solids is well described in literature - many can be found in Ref. [24]. For multicomponent materials research is not as deep, but some trends may be identified, as described in the following summary.

- In the energy region of interest for Hall Effect Thrusters (<600 eV) sputtering increases with increasing energies. Must be noted, however, that for higher ion energies (>10-100 keV) sputtering will decrease as ions penetrate deeper in the solid and less energy gets deposited at the surface, where sputtering occurs.

- Sputtering yield strongly depends on the angle of incidence of impacting ion beam with respect to surface normal, $\theta$ (Fig. 2.8). As $\theta$ increases, the sputtering yield increases as well. This behaviour is attributed to the penetration depth of the impacting particle which, as the angle grows, decreases, and atoms close to the surface are more easily ejected. The sputtering increases up to a certain maximum value, $\theta_{max}$, after which it start to decrease since the energy transfer of impacting ions becomes less efficient. $\theta_{max}$ depends on many factors, such as impacting and target species, but tends to be in a range between 50° and 70°. At grazing incidence ($\theta \sim 90°$) sputtering will be null as the repulsive action of surface atoms is strong enough to prevent ions from penetrating into the target. In the case of HETs the entire range of incidence angle must be considered as the flow is not homogeneous, and the surface geometry may not be aligned with the bulk velocity of the plasma.
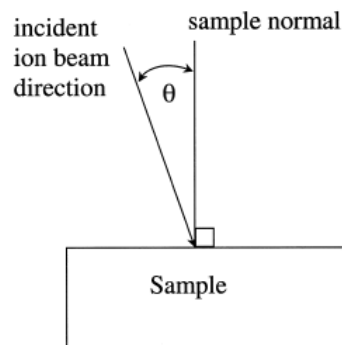


**Figure 2.8:** Schematic representation of incident angle [22].

- As the energy of the impacting particle decreases, sputtering will eventually cease. The energy below which this occurs is called *Threshold energy* ($E_{th}$). Experimental measure of this energy is very difficult, as it requires techniques sensitive enough to detect minuscule amount of sputter. A lower limit for $E_{th}$ was defined as the energy at which the maximum transferable energy equals the binding energy of the surface material. However, more experiments are needed to characterize very low energy sputtering yield, since the majority of impacting ions in HETs have energy close to threshold.

- Temperature of target material also influences sputtering. This may be due to different causes, like decrease in bond strength in the material if it is affected at elevated temperature or structural weakness which arise due to thermal oscillations [25]. At elevated temperature, around 30% of melting point, yield increases as the surface rids itself of any accumulated damage and levels outs, since smoother surfaces tend to erode more than rougher ones.

- In multicomponent sample, as in $BNSiO2$, the material commonly used in HETs, different erosion rates are observed for the different components. For HETs with ceramic insulators the specific material should be studied in order to be characterized.

A lack of experimental data regarding sputtering has been found both for monoatomic solids and composites such as BNSiO2. This is often overcome by using fitting formulas based on different sputtering theories which are generally developed for monoatomic solids [26]. Perhaps the most used semi-empirical formulas are those proposed by Yamamura *et al.* [24] valid only for monoatomic solids, but often extended to composite materials via adjustment of parameters based on experimental data.

## 2.3   Plasma Modeling in Hall Effect Thruster

Computational modeling of plasma in HET has resulted interesting for several reasons. It can be used to predict thrusters' operative life, ultimately determined by the erosion of channel walls, without the need for expensive and time consuming tests. Can help to understand better the physics of these devices and how operating parameters influence performance. Lastly, these computational codes could useful as design tools for the next generation of thrusters.

The main approaches to model HET plasma are fluid modeling, kinetic modeling, and hybrid modeling.

Fluid modeling [27] considers electrons, ions and neutrals as three independent fluids which make up the plasma. Quasi-neutrality is assumed, hence the electrons number density is taken equal to the ions density ($n_e \simeq n_i$). It resolves the

equations for particle, momentum, and energy conservation of the three species. This approach is computationally efficient but the main drawback is the inability to model the velocity (VDF) and the energy distribution function (EDF).

Kinetic modeling (or Particle-In-Cell) [28] considers electrons and ions as discrete particles while neutrals can be modeled alternatively as a fluid or as particles. Each simulated particle is representative of a large number of real particles, hence the name, and their trajectory is followed in the phase space considering both electric and magnetic fields. The "specific weight" represents the number of real particles in each macro-particle; it varies among the particles and changes over time. The discrete particles automatically model VDF and EDF but the computational cost for this approach is very high.

Hybrid modeling [29] offers a good compromise between fluid modeling and kinetic modeling processing in different ways heavy particles and electrons. In this approach, ions and neutrals are typically modeled as discrete particles and electrons are modeled as a fluid. The advantages of this approach are to be able to capture non-Maxwellian features for the heavy species (so VDF and EDF) and having a computational cost between fluid and kinetic. The main drawback is that this approach is not self-consistent: it requires empirical parameters for the anomalous electron transport, especially in the exhaust region where the magnetic field is maximum and intense ionization is present, hence the collisions between electrons and neutral are not sufficient to explain electron transport [15].

In the present work **HYPICFLU** (**HY**brid **PIC-FLU**id ), the hybrid code developed at the Italian Aerospace Research Centre (CIRA) in the framework of the activities on space electric propulsion, has been used. A brief description of the model is given in the following, while detailed information can be found in papers [30], [31] and [15].

HYPICFLU is formed by two different modules: the Particle-In-Cell (PIC) module for the heavy species (neutrals and ions), coupled with the fluid model for electrons.

All variables are time dependant, except the magnetic field. The two modules communicate iteratively each other because the outputs of a module are the inputs of the other and vice-versa. In particular, Fluid electrons equations require as input the number density of both ions and neutrals ($n_n$, $n_i$), the velocity of ions ($\vec{u_i}$) and the ionization rate ($\dot{n_i}$) and return the electron temperature ($T_e$) and the plasma potential ($\Phi$), from which the electric field ($\vec{E}$) that accelerates ions in the channel is computed. On the other hand, the heavy species sub-model needs as inputs electron temperatures and electric fields and gives back both the number density of ions and neutrals, the velocity of ions and the ionization rate.

Figure 2.9 shows the aforementioned iterative cycle, where $\vec{B}$ is the magnetic field, given as input.

26
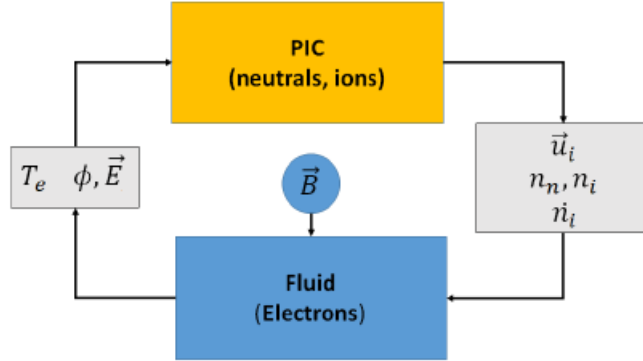
**Figure 2.9:** Hybrid model: interaction between PIC and Fluid modules. [15]

## 2.4 Erosion modeling

Predicting Hall Thrusters channel erosion is a difficult task, as it requires a precise characterization of wall materials, discharge plasma properties, plasma wall interactions and the ability to simulate the impact of microsecond-scale events over the course of thousands of hours of operation. This far no model has been able to successfully predict wall erosion because of the uncertainties of experimental data available and limited computational power. Current model strongly rely on tunable parameters which must be adjusted according to pre-existing erosion data [32].

The simplest models consist in curve-fitting available erosion data in order to extrapolate erosion trends and predicting thrusters life without complete life tests data. Recent work has improved prediction by using machine learning to analyze multiple thruster life test datasets [33]. This approach is limited however, as it requires a thruster to be constructed and tested, before any lifetime estimation can be made, hence not enabling study of parameters effect during early design stages.

Other models introduced fluid equations to describe the plasma in the channel and determine the ion flux to the walls. Coupled with a sputtering model could give prediction on erosion rates.

Later efforts included plasma wall interactions and applied semi-empirical models based on experimental models. These semi-empirical models can make estimations of the erosion profiles and thruster lifetime from a more limited set of experimental data [34]. Many authors fitted variations of the formulas proposed by Yamamura and Tawara [24], for monoatomic solids, to experimental sputtering data available, like from Garnier *et al.* [35, 36]. Yamamura's formula can be written in the general form as in Eq. 2.7, where $F$ is a function that describes the dependence of sputtering on impacting particles and target material properties [32]. $E$ is the energy of the impacting ion, $E_{th}$ is the threshold energy and $b$ is a fitting parameter. Threshold energy also works like a fitting parameter, being very difficult to define as discussed

above, but is typically assumed to lie between 30 and $70eV$.

$$Y = F(...) \left(1 - \sqrt{\frac{E_{th}}{E}}\right)^b \qquad (2.7)$$

It is clear that the parameters in Yamamura's formula depends on sputtering ions as well as surface material and require ad-hoc measurements to find the best fitting parameters.

Gamero *et al.* [37] have applied the simplified Yamamura and Tawara formula to Garnier's data in order to compute erosion rate given plasma properties. They considered experimental data of $Xenon$ ion bombardment on $BNSiO_2$ ceramic. Their approximation seems to work well for the lower energies tested by Garnier and uses a cubic fitting for the angle dependence, as shown in Eq. 2.8, where they used a value of 58.6 as threshold energy. However, Garnier data shows a low dependence of sputtering on incidence angle, hence the model developed by Gamero *et al.* will also show a lack in angle dependency since it approximates Garnier's data.

$$Y(E, \alpha) = (0.0099 + 6.04 \times 10^{-6}\alpha^2 - 4.75 \times 10^{-8}\alpha^3) \times \sqrt{E} \left(1 - \sqrt{\frac{58.6}{E}}\right)^{2.5} \qquad (2.8)$$

Coupling Eq. 2.8 with ion fluxes to the wall, in their case derived by HPHall code, they were able to obtain erosion rates.

Others, like Cheng and Martinez-Sanchez [38] have fitted data from Yalin [39], who analyzed sputtering of various ceramics on a wider range of energies, starting at 80 eV, and angle of incidence. Cheng used a semi-empirical formula, shown in Eq. 2.9, that fitted the Yamamura's formula to experimental normal sputter yield data of boron nitride ($BN$) by $Xenon$ ions via coefficients ($A$ and $B$) which depend on the threshold energy considered.

$$Y_n(E) = \frac{AE^{0.474}}{1 + AE^{0.3}} \left(1 - \sqrt{\frac{E_{th}}{E}}\right)^{2.5} \qquad (2.9)$$

He then multiplied the normal sputter function to a function depending on the angle of incidence, though very different to that of Gamero. Then the angular sputtering yield may be computed as shown in Eq. 2.10, where $Y_n$ is the normal sputter yield, $E$ and $\theta$ are the energy and angle of the incident particles. Here the function will not be shown in detail, but it must be noted that $F$ is a function that depends on energy, while $G$ is a function of the angle. Both $F$ and $G$ contain more empirical parameters used to fit experimental data.

$$Y_\theta(Y_n, E, \theta) = Y_n \times cos^{-F}(\theta) \times e^G \tag{2.10}$$

Cheng and Martinez-Sanchez also used HPHall to obtain information about the plasma in the channel.

A very different approach was taken by Yim [34] who developed a Molecular Dynamic Sputter Model to be coupled with an Hydrodynamic Plasma Model. Molecular dynamics (MD) is a deterministic particle simulation where the motion of each atom is governed by Newton's law of motion while the forces acting on the particles are modeled through inter-atomic potential functions. MD has been successfully used in the past, however sputtering in the case of HETs is particularly difficult, since wall material contains more than one component species. Yim dealt with BN, modelling an hexagonal lattice structure comparable with that of graphite and then overlaying the sheaths to simulate depth. This approach allowed for an erosion model which was not based on an empirical or semi-empirical approach.

The models presented work well to predict the overall erosion depth but lack a deep insight in the erosion process since they are 2D models that treat the material as homogeneous. They don't have the complete picture of the problem and can't simulate the different erosion for the different components. In an effort to model more complicated effects of erosion, Schinder *et al.* [40] have developed a 3D model for the sputtering of heterogeneous solids, in particular $BNSiO_2$. Boron nitride silica is an anisotropic material, where grains of $BN$ and $SiO_2$ can be clearly discernible in SEM images. Their model was able to reproduce the non homogeneous erosion profiles observed, caused by the different sputtering rates of boron nitride and silica, producing a cliff-and-valley like structure, increasing the roughness of the surface. Average erosion rate is biased towards the element with the lowest sputtering rate in the material mixture.

## 2.5   Motivation and objective of thesis

As already mentioned, during the thruster's operation the plasma, interacting with the channel walls, erodes their surfaces, commonly made of ceramic composites. As the erosion proceeds it will eventually expose the electrodes, ultimately ending the thruster's life. Generally speaking, in space propulsion, the mission is defined by the $\Delta V$ required to accomplish it, hence by the time of firing of the motor being related to the amount of propellant required, which determines its state of wear. A key difference between Earth or atmospheric propulsion and space propulsion, is that in space is often impossible to check, repair or modify any device once it leaves the Earth surface. It is of key importance, then, to know in advance the lifetime of the thruster, in order to match the thruster and the mission in the best possible way.

One possible way to evaluate thruster's life is to bench test them. However, that is a very expensive and time consuming way of characterising their durability - it's enough to think about the *Deep space* 1 mission mentioned in chapter 1.1 - having lifespan exceeding the tens of thousands of hours. This makes bench test almost absurd for thrusters lifetime characterization. This is the reason why, in the past decades, as electric propulsion increased in popularity, many have tried to develop computerized models to predict the erosion of the inner surfaces of the thruster in order to predict its expected lifetime. This would allow for a characterization of the thruster's lifetime avoiding the costly bench tests. Moreover, it may be possible to study different combination of ceramic composites and propellants before building the thruster itself.

The current thesis shares the objectives just mentioned, trying to develop an erosion model able to predict the erosion of $BNSiO_2$ in Hall Effect Thrusters using $Xe$ as propellant. The model developed will use new data available in literature, and may be adapted to different materials and propellants provided the related sputter yield data.

## 2.6 Outline of thesis

Having given an introduction about space propulsion and explained the concepts of erosion via plasma wall interactions, in the following chapters will be described the erosion model developed. In particular, chapter 3 will explore the current sputter yield data available regarding *borosil*, impacted by $Xe$ ions, and its dependence on angle and energy, as well as on temperature. A simulation using a modified version of the Gamero-Castano's erosion model is reported, with particular emphasis on the effect of $E_{th}$. Then an erosion model, based on sputter yield data of *borosil* impacted by $Xe$ ions from Ref. [41] is developed, and its coupling with the HYPICFLU plasma model is explained.

In chapter 4 the erosion model is applied to a simulated version of the SPT-100 thruster, since it is the most studied and there is widespread experimental data available. The erosion is simulated up to 1020 hours of operation. The results are then compared to experimental ones and commented. Then, in chapter 5 are reported the simulated eroded profiles of an hypothetical *magnetically shielded* version of the SPT-100, developed at the Italian Aerospace Research Center. The results are compared to the $un-shielded$ configuration to comment the erosion reduction.

# Chapter 3

# Channel Erosion Model

In this thesis the main focus is toward the modellization of boron silica ceramic with Xenon based plasma. $BNSiO_2$ has a higher sputtering yield rate compared to pure $BN$, but it is most commonly used, in various concentrations, thanks to better machinability and ease of forming over boron nitride [40].

An erosion model based on sputtering data for borosil ceramics, impacted by $Xe$ ions will be presented.

## 3.1 BNSiO$_2$ Sputtering

As already mentioned, sputtering of pluriatomic material is not yet well understood and is difficult to characterize. While further study is needed at low energies, high temperature and angles of incidence, an overview of current knowledge is presented.

### 3.1.1 Normal sputter yield

Normal sputter yield refers to the sputtering yield caused by ions impacting the surface from an orthogonal direction, parallel to the surface normal, at various energies. Many tests have been done on solids at high energies, but few have been conducted at low energies, in the range concerning HETs. Considering a 300 V discharge voltage, common for SPT thrusters, the maximum energy which single ionized ions can reach is $\sim$ 300 eV. Double ionized atoms will have energies up to twice the energy of a single ionized one, but generally are a minor part of the overall ionized particles. In our model only single-charge ions are tracked by the PIC module of HYPICFLU [15]. Most atoms will be ionized close to the exit of the channel, towards the latter part of the potential gradient, hence will possess energies well below this limit. Prior research that has been done to characterize sputter yield at various energies, is shown in Fig. 3.1, in the energy range of interest

($E < 600eV$). Both Ranjan [41] and Garnier [35] have conducted experiments on $Xe^+$ ions impacting on $BNSiO_2$ ceramics. Garnier *et al.* measured the sputter yield via weight loss, while Ranjan *et al.* measured it via QCM.

Yalin performed sputtering measurements of various materials, including $BN$ and quartz ($SiO_2$), impinged by $Xe^+$ ions, which are shown in Fig. 3.1. Yalin *et al.* also measured sputtering via weight loss.

Kim *et al.* also performed tests of $BNSiO_2$ sputtering by $Xe^+$ ions and measured it via weight loss. However their results are reported in $mg/C$, hence have been converted using average density and composition of borosil, considered to be $2.32mg/mm^3$.
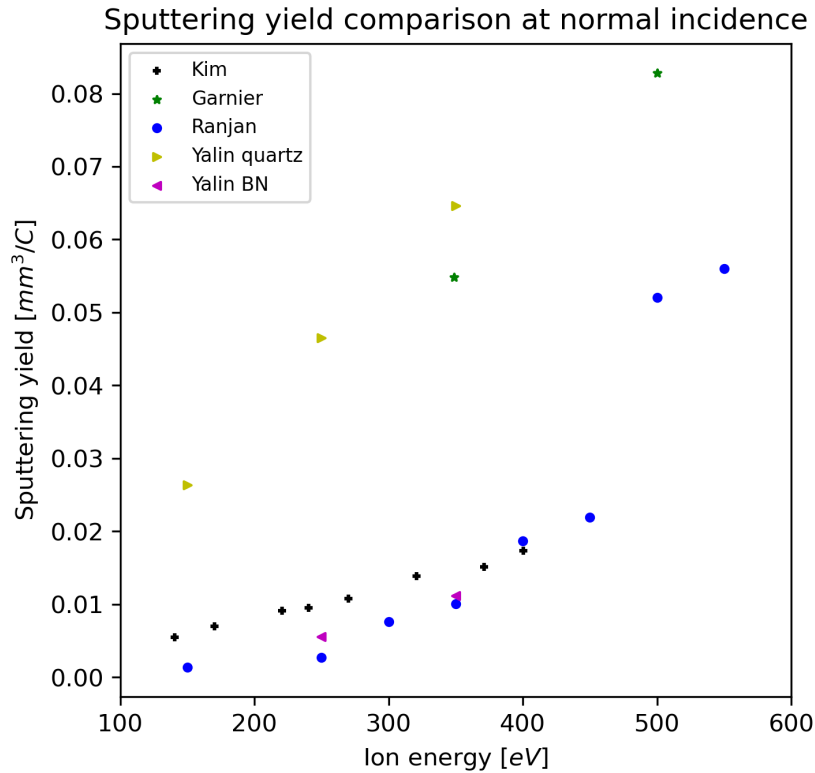


**Figure 3.1:** Normal sputter yield comparison, by $Xe^+$, at various impacting ion energies published by [35],[39],[41],[42].

### 3.1.2 Angular sputter yield

All the papers cited above, explore the dependence of the sputter yield with incidence angle, at different energies. In Fig. 3.2 the data taken from references [35],[39],[41] and [42] are collected. In order to better show the angular dependence,

all data has been normalized with its respective sputter yield at normal incidence. All data clearly show an increase in yield from normal incidence until an angle of $\theta_i = 55 - 65°$ where it begins to decrease. Garnier comments that the incident angle dependence in the ceramics tested is weaker than observed in literature. This can be seen also in Fig. 3.2 where Garnier data shows a weaker angular dependence than the others. Simulation of sputter yield also show similar pattern as presented here.
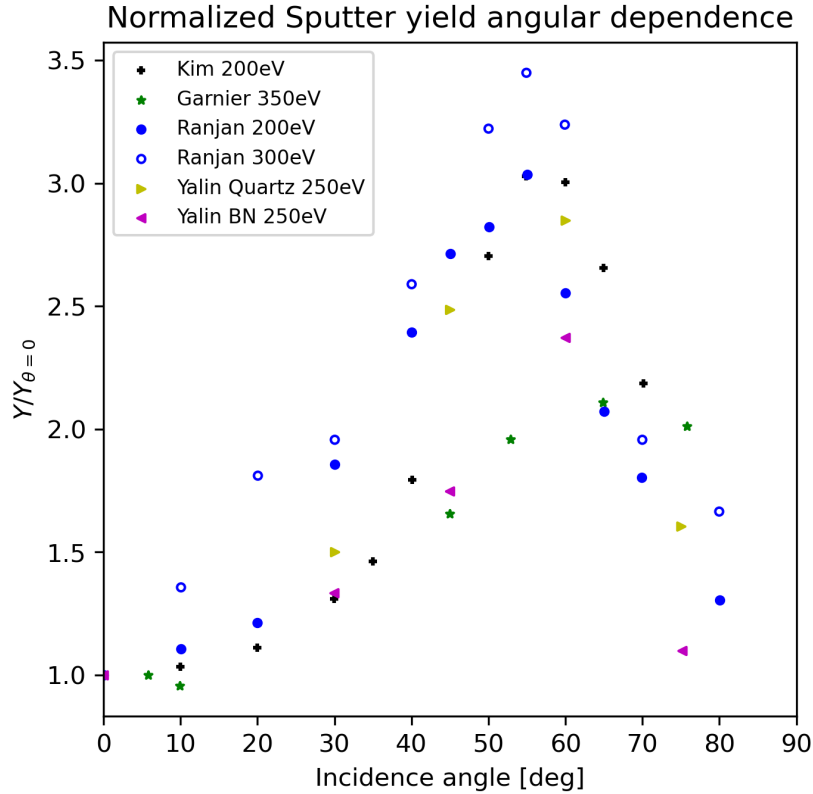


**Figure 3.2:** Normalized angular sputter yield comparison by $Xe^+$, [35],[39],[41],[42].

### 3.1.3 Temperature dependence of sputter yield

Originally, the total erosion was thought to be the contribution of material which is physically sputtered and from material that is directly sublimated. Physical sputtering is independent of target surface temperature, and is related only to incident ion flux and particle energy. The second, sublimation rate, which strongly

increases with surface temperature, does not depend on incident particles and becomes dominant at very high temperatures. Experimental evidence shows, however, that the erosion yield is temperature dependent and a strong increase in the erosion rate happens well below the temperature expected by thermodynamic sublimation, leading to think that other phenomena come into play. A few explanations have been suggested to describe this behaviour.

Doerner *et al.* developed a model using the surface adatoms concept [[43],[44]]. An adatom is an atom which has acquired energy from an impacting energetic particle. Such energy, enough to free the atom from its lattice, is not sufficient to sputter the atom from the surface but is enough to create a vacancy. Some vacancies are filled again as atoms recombine with the lattice, while others are left empty as the dislocated atom diffuses away from the site. Since the dislocated atom is not in a lattice site, its binding energy to the surface is less than those atoms in the lattice. A lower binding energy allows adatoms to be released from the surface at lower temperatures than those predicted via sublimation of the material. In Fig. 3.3 is schematically shown the Doerner *et al.* model, called *Radiation Activated Adatom Sublimation*, or *RAAS*, where on the right side can be seen the dislocated atoms, free from the lattice structure after the ion impact, depicted on the left figure.
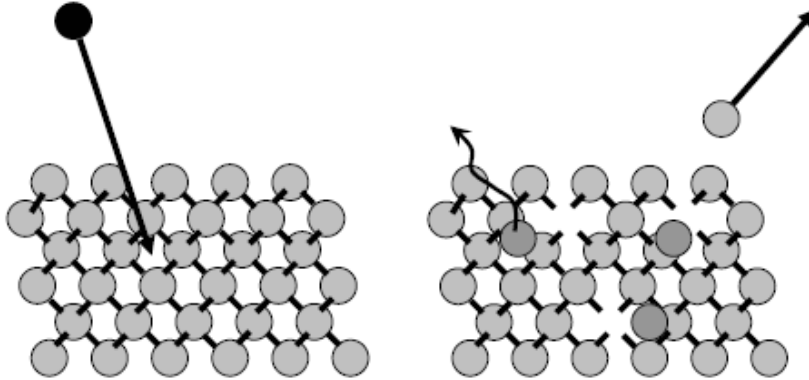


**Figure 3.3:** Schematic representation of the Radiation Activated Adatom Sublimation (RAAS), from Ref. [23].

In the suggested model, the effect with energy and incident angle may not be linear, since, as discussed in Ref. [43], adatoms are created at the surface, hence their effect may be more pronounced when impacting particles interact strongly with the surface. This means that for highly energetic particles with very long stopping distances the effect may be less pronounced. To the contrary, low energetic particles, which penetrate less, may have a stronger effect.

In Ref. [45] is discussed a model, called the *inclusion model*, which also suggests

a weakening in the lattice structure of the surface, but via different mechanisms. The inclusion model the impacting particle enters the lattice structure as an inclusion. As can be seen in Fig. 3.4, the implanted particle distorts the lattice reducing the binding energy of neighboring atoms. Having a lower binding energy, such atoms are prone to sublimate at lower temperature.
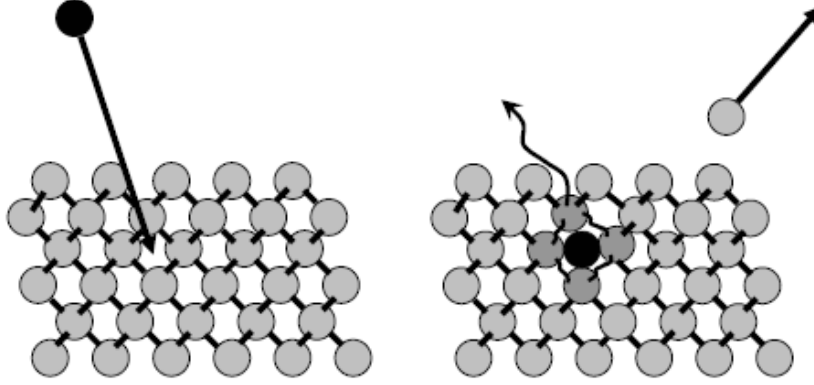


**Figure 3.4:** Schematic representation of the inclusion model, from Ref. [23].

Another model, put forward to explain the early increase in sputtering with temperature is the *Thermal Spike* (TS) model, which is generally associated with very energetic heavy particles. The basic concept of the *TS* model is that the small region of the surface where the highly energetic particle impacts undergoes a sudden increase in temperature, resulting in evaporation of atoms from the surface.

The latter model is proposed to be the reason of the increase in sputtering observed in the experiment carried out by Parida *et al.* [25] where M26 silica samples is irradiated by Xe ions at high surface temperature and for prolonged times. Their experiment was carried out only at ion energies of 500 eV and 55° of incidence angle. They observed an almost linear increase in sputter yield with temperature, and a stability of the yield with longer exposure times.

## 3.2    Gamero erosion model

In literature, the model developed by Gamero *et al.* looks to be the most used to predict erosion in HETs. It uses borosil sputter yield data, impacted by $Xe$ ions, from Garnier *et al.*, with an extrapolation of data below the energies evaluated by Garnier based on a semi empirical law proposed by Yamamura *et al.* The process behind their model can be found in Ref. [37].

They used a fitting function, in the form as shown in Eq. 3.1, where $Y_v$ is the sputter yield, expressed in $mm^3/C$, $\alpha$ is the angle of incidence of the particle with the surface, expressed in degrees, $E$ is the impacting ion energy, in $eV$.

$$Y_v(E) = (\beta_0 + \beta_1\alpha + \beta_2\alpha^2 + \beta_3\alpha^3) \times \sqrt{E} \times \left(1 - \sqrt{\frac{E_{th}}{E}}\right)^{2.5} \qquad (3.1)$$

$\beta_n$ and $E_{th}$ are the fitting parameters which, to fit Garnier's data for 350 and 500 eV sputter yield, are found to be:

| | |
|---|---|
| $\beta_0$ | 0.0099 |
| $\beta_1$ | 0 |
| $\beta_2$ | $6.04 * 10^{-6}$ |
| $\beta_3$ | $-4.75 * 10^{-8}$ |
| $E_{th}$ | 58.6 $eV$ |

**Table 3.1:** Fitting parameters of Gamero's formula [37].

Regarding $E_{th}$, Garrigues *et al.* evaluated its influence, using a similar fitting formula to that proposed by Gamero *et al.* They concluded that a change in threshold energy leads to a similar value of the sputter yield at high energies, but has great impact at lower energies. Our simulations also show that different $E_{th}$ lead to different points in the channel wall where erosion begins, since in the plasma simulations ion energy increases toward the exits, where higher velocities are reached.

The Gamero erosion model was applied to evaluate the erosion of channel wall geometry in the SPT-100 thruster. As Fig. 3.5 show, in this case limited only to the lower surface of the acceleration region, changing the threshold energy visibly changes the erosion depth.

This intermediate result led us to perform a small change in the model, with a change in $E_{th}$ as the key factor in it. The coefficients used in the equation proposed by Gamero, as shown in Tab. 3.1, were slightly modified to fit Garnier's experimental data of borosil sputtering by $Xe$ ions at 350 eV impacting ion energy accounting for the change in threshold energy. The coefficients found are reported in Tab. 3.2.

Both the approximations for $E_{th} = 20eV$ and $E_{th} = 35eV$ are accurate for Garnier's data [35] at 350 eV impacting ion energy and closely follow the original Gamero function, as shown in Fig. 3.6.

In some cases the threshold energy may be increased to fit erosion experimental data, like Giannetti *et al.* did [46]. In others, the threshold energy has been as low as 18.3 eV to fit experimental data of sputter yield for $BN$ and $SiO_2$ by Yalin *et al.* [40].

An energy threshold of 35 eV was chosen.

Predicted erosion profiles for different Eth
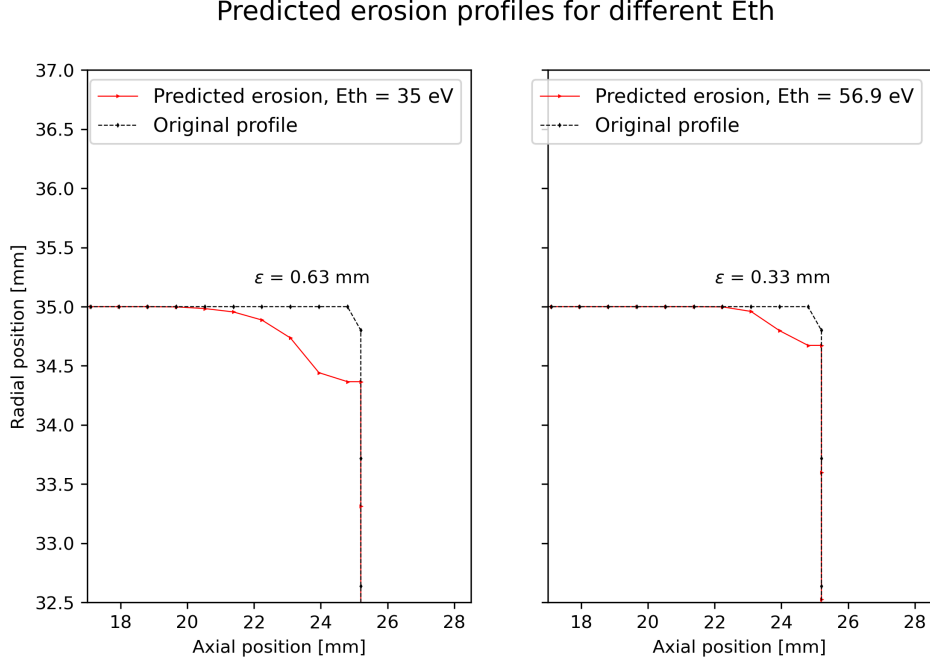


**Figure 3.5:** Erosion profiles of the inner surface using different threshold energies in Gamero's formula [37], for the first 60 hours of simulated operation.

|  | $E_{th} = 35 \ eV$ | $E_{th} = 20 \ eV$ |
|---|---|---|
| $\beta_0$ | 0.007 | 0.0053 |
| $\beta_1$ | 0 | 0 |
| $\beta_2$ | $4.45 * 10^{-6}$ | $3.47 * 10^{-6}$ |
| $\beta_3$ | $-3.55 * 10^{-8}$ | $-2.78 * 10^{-8}$ |

**Table 3.2:** Fitting parameters of Gamero's formula [37].

The erosion simulation was performed in 60 hours time-steps, up to a cumulative 300 hours of simulated operative time. As shown in Fig. 3.7, the erosion model, with the modified Gamero's equation, underestimates the erosion magnitude at the channel exit by 17.6% and 19.7% for the inner and outer surfaces. The erosion begins at about 18 mm from the anode, around where the experimental erosion begins. The curvature of the computed erosion is, however, strongly different, and the model fails to predict the regression of the channel walls closer to the anode. This may be due to the exponential characteristic of the sputter yield function at energies just above the threshold, as shown in Fig. 3.8, which may lack to predict
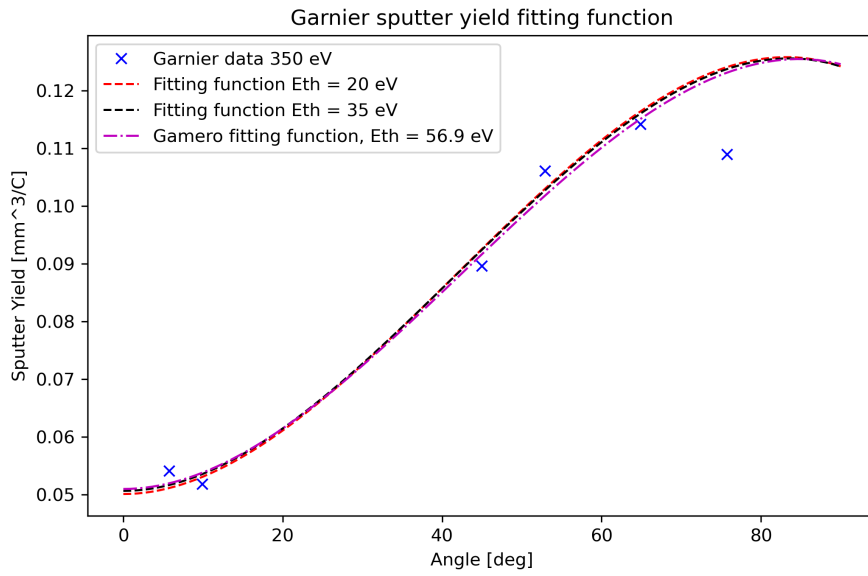
**Figure 3.6:** Fitting function for Garnier's data at 350 eV, considering different possible threshold energies.
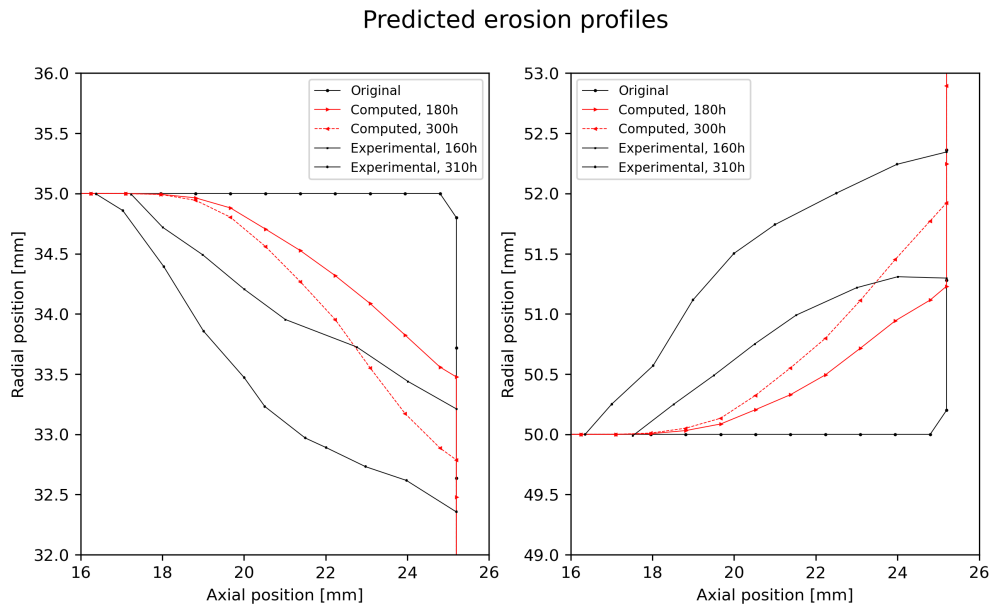


**Figure 3.7:** Computed and experimental erosion profiles for the outer and inner walls, for the first 300 hours of operation.

significant erosion at low energy.
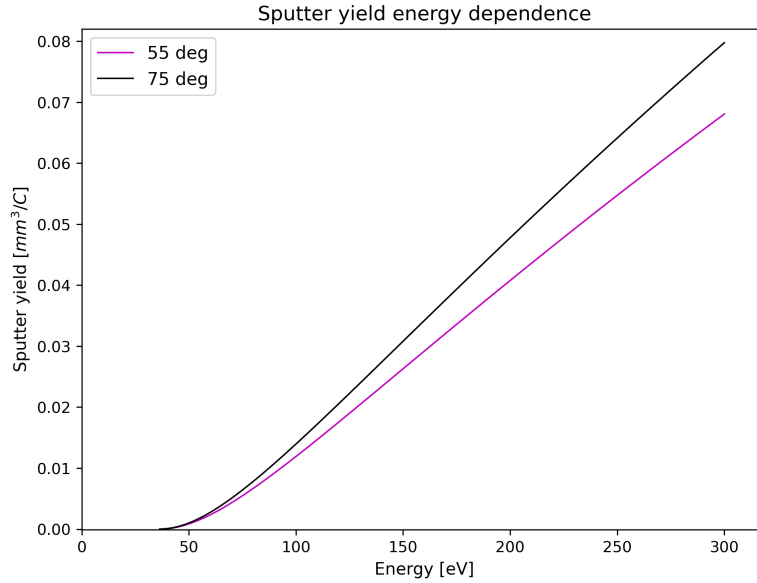
**Figure 3.8:** Sputter yield model, at different angles of incidence, for low energy projectiles, considering an $E_{th}$.

For the sake of comparison, a plot of the computed erosion profiles is shown in Fig. 3.9 where both the computed profiles, ours and Gamero's own, are compared. Again, like before, our code underestimates the erosion closer to the anode, especially at the inner surface, compared to that estimated by Gamero *et al*. For the outer surface the predicted erosion profiles are much closer.

A big limitation of the model, as shown above, is the presence of the threshold energy, which is a value difficult to characterize, and may be adapted to fit experimental results, like what was done, and others did. In the absence of experimental values on which to base the computational results, it may be difficult to fix a value for $E_{th}$. Also, with experimental data available at 350 eV as the lowest impacting ion energy, it is hard to predict how sputter yield will behave at lower energies.

## 3.3 Sputter yield model

In an effort to reduce the dependence on empirical data based on experimental erosion results, hence eliminating the need for experimentally eroded channel on which to base the erosion model, a deeper dive in literature was made to try and find sputter yield data for impacting ion energies as low as possible leading to further consideration of data from Ranjan *et al*. [41]. As mentioned before, Ranjan *et al*. explored sputter yield of borosil by $Xe^+$ at energies as low as 100 eV. Their

Comparison between computed erosion profiles
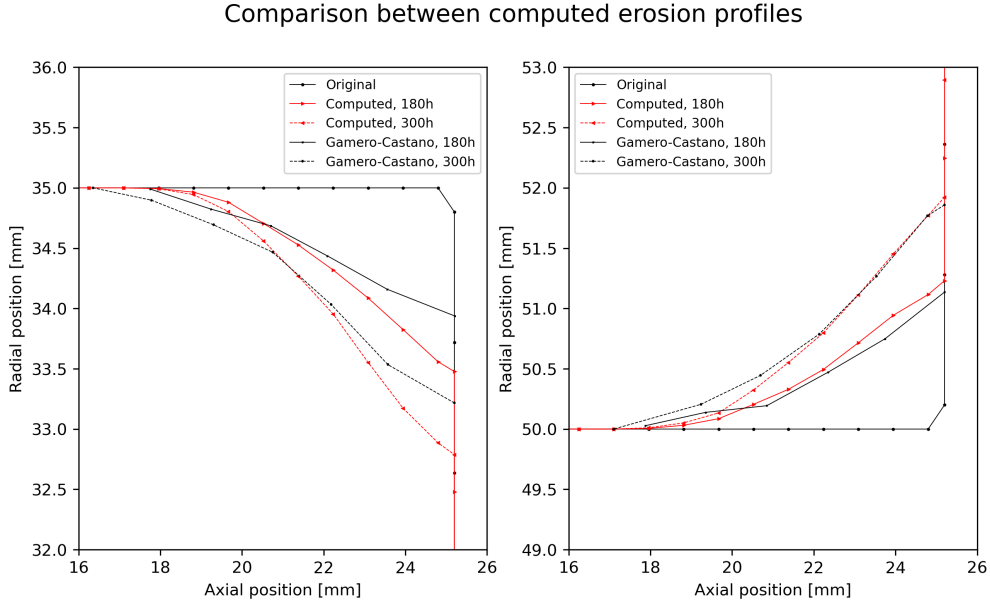


**Figure 3.9:** Comparison between computed erosion profiles, by Gamero-Castano [37] and our modified one.

data also explores the sputtering yield of $BNSiO_2$ via $Xe^+$ in the widest range angles available in literature to date.

Having reviewed the current state of borosil sputtering experiments, a sputter yield model is developed to try to predict channel wall erosion in HETs. In the process, simplifying assumptions will be made, to compensate for the limited available data.

### 3.3.1 Ranjan data erosion model

Ranjan's data is reported in Fig. 3.10 over a three dimensional plot, to make the dependence of sputter yield over incidence angle and energy clear. The sputter yield measurements lack data for energies lower than 100 eV and angles higher than 90 deg.

For what concerns the sputter yield at incidence parallel to the surface, which is an incidence angle of 90° with respect to the surface normal, the extrapolation is pretty straightforward, as the sputter would be negligible. For that reason, the sputter yield has been put equal to 0 for all energies.

For the extrapolation of data below the lowest energy available, the conclusion was not as easy to reach. In particular there is no clear value for $E_{th}$, and it may change due to composition of the material and grain orientation. Given the strong dependence of sputter yield on the angle of incidence, it was assumed that the
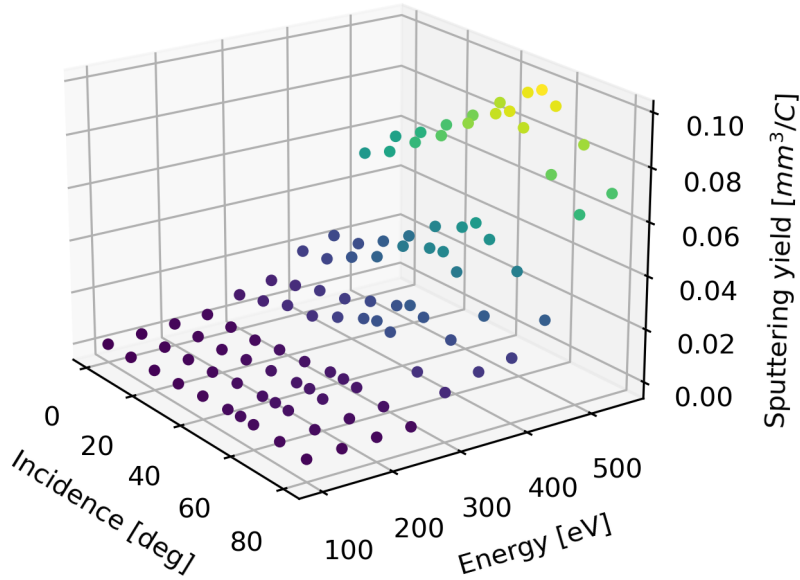
**Figure 3.10:** 3D representation of Ranjan's data [41] of sputter yield for $BNSiO_2$ by $Xe^+$.

threshold energy might as well be dependent on the incident angle of the impacting particle. This led us to not fit a single value, valid for all angles, as $E_{th}$, but instead extrapolate the available sputter yield data below 100 eV energies. Since the data considered is angular dependent, the threshold energy will be as well.

Due to the lack of data and the new approach followed, a very simple extrapolation was used, considering the average gradient between all the available data. That is a linear extrapolation below 100 eV, as shown in Fig. 3.11, for few angle of incidence. As can be seen, the energy where zero sputter yield is reached varies with the incidence angle.

In Fig. 3.12 is shown a curve derived by the extrapolation of sputter yield, from Ranjan's data, below 100 eV, at all the angles analysed by Ranjan *et al*. The energies at which the sputter yield nullifies are, however, quite higher than the energy range considered to be the threshold energy range. Must be noted that $E_{th}$ has been used as a calibrating tool to fit experimental data, and in one case was considered to be $E_{th} = 85eV$ [47], which is closer to what our model predicts. As mentioned before, it is not constant with angle, and it presents a minimum at an angle of 55°, the same angle where, given an energy, a maximum of the sputter yield is reached.

41
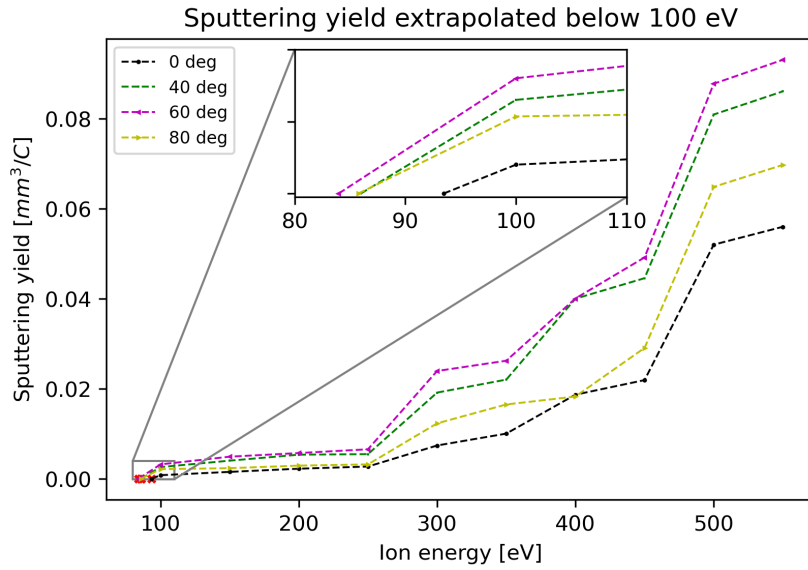
**Figure 3.11:** Linear extrapolation of sputter yield below 100 eV, for different angles of incidence.
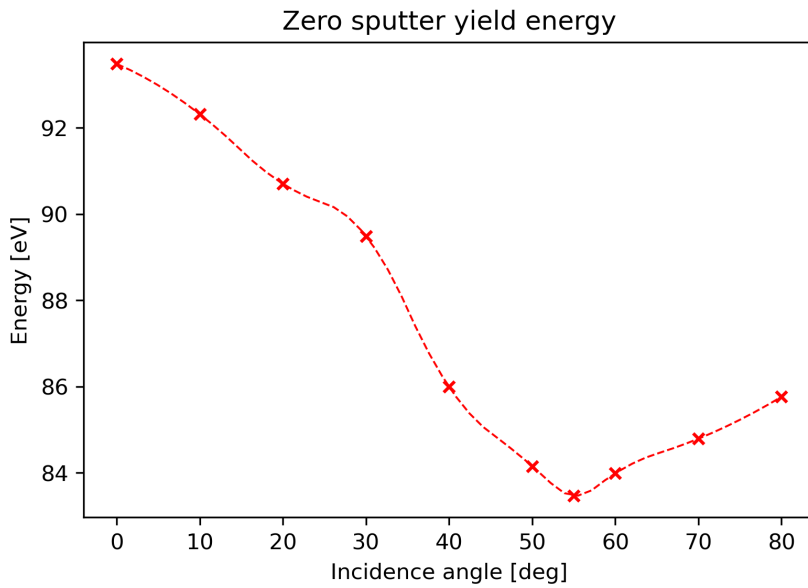


**Figure 3.12:** Zero sputter yield energy extrapolated from Ranjan's data for all available angles.

In order to relate all the available data, Ranjan's data and the extrapolated ones, a function already available in the *scipy* python library, called *CloughTocher2DInterpolator*

was used, which interpolates 2D data constructing a piecewise cubic interpolation using a Clough-Tocher scheme [48]. The gradients of the interpolant are chosen so that the curvature of the interpolating surface is minimized. The function built in this way, shown in Fig. 3.13, is a surface, where every point is defined by three coordinates. Two inputs are needed when calling the function, the angle of incidence and the energy of the impacting particle, and the output, coinciding with the $z$ coordinate, is the sputter yield.
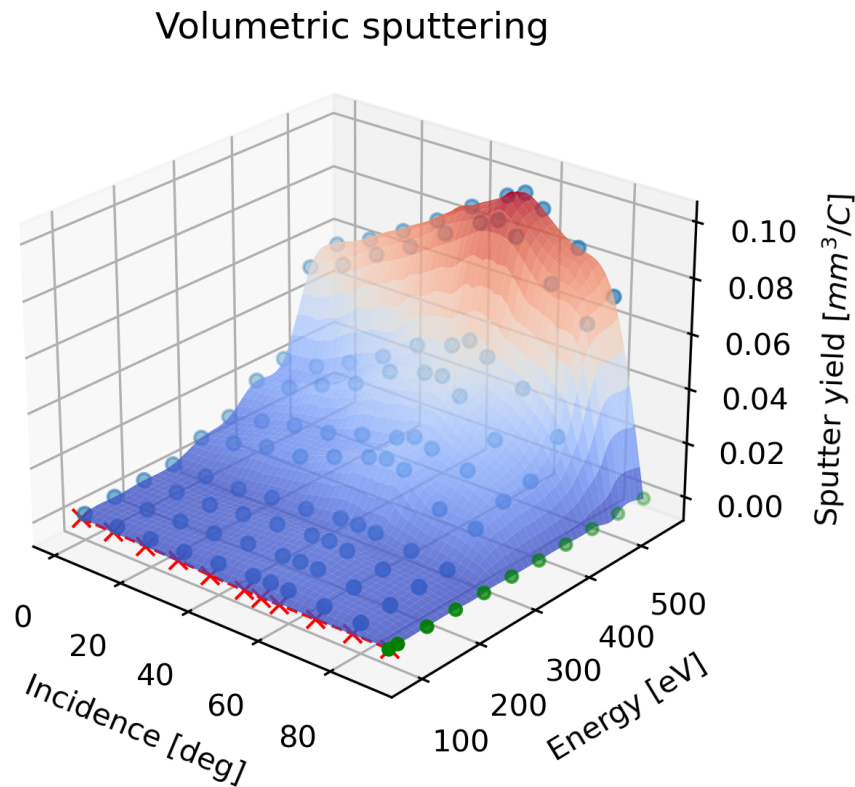


**Figure 3.13:** Representation of the sputter yield function. Red crosses are the data extrapolated below 100 eV, the green dots are the extrapolated sputter yields at 90° of incidence.

With the red crosses is represented the extrapolated zero sputter yield energy, while the green dots represent the sputter yield at 90°incidence.

With this function, the erosion of the channel was computed and compared with experimental data.

**Results**

Coupling the sputter yield function with plasma data provided by the HYPICFLU code, a prediction of the channel erosion was made. Like in the case with Gamero's model, the time steps to evaluate erosion were 60 hours. After that simulated operative time, the new grid was used to simulate the new plasma conditions in the channel and with them do a new erosion simulation. The results, up to 300 hours of operation, are shown in Fig. 3.14, with the experimental profiles after similar operating time.

It is clear, straightaway, that the erosion is strongly underestimated. The magnitude of the erosion at the channel exit is much less than the experimental one of about 85% for the inner surface and almost 90% for the outer one, and also than the erosion predicted with the previous model. Furthermore, the predicted erosion begins a lot closer to the channel exit, at around 23 $mm$ from the anode compared to the almost 16 $mm$ observed experimentally. This result is, most likely, due to the high zero sputter yield energy, which prevents any ion, with energy below $\sim 83$ $eV$ to cause any erosion.
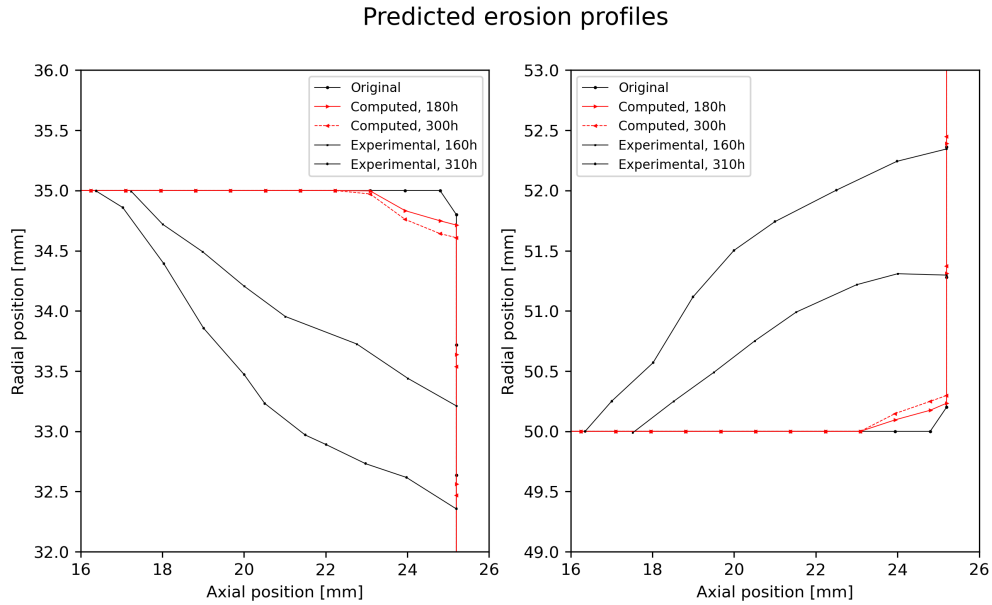


**Figure 3.14:** Simulated channel wall profiles after 300 hours of operation.

This is, in fact, not the result we were hoping for, and led us to investigate deeper the effect of surface temperature on sputter yield.

### 3.3.2 Sputter yield function with temperature effect

As mentioned before, most erosion models do not consider the effect of surface temperature in their sputter yield function. That is due to the fact that not many experiments have been conducted to evaluate such data, and the few that have noticed an increment in sputter yield at temperature generally higher that those experienced by HETs. For this reason, the erosion models developed up to this date, considered the effect of temperature negligible.

However, recent data from Parida *et al*. [25] analysed the effect on sputter yield of temperature, up to 600 °C, which can be reached by the ceramic surface inside the channel. In particular, they analysed the sputter yield of borosil (M26 Grade, Saint Gobain, the same used by Ranjan *et al*.) by $Xe^+$ at an incidence of 55°, where the sputtering yield is at its maximum, and an energy of 500 $eV$. The borosil samples were irradiated at different orientation of sintering, parallel and perpendicular, giving only slightly different results, but showing the same trend. The measurements were performed via QCM, again the method used also by Ranjan *et al*. The part of the experiment which is of particular interest to us, is the sputter yield measurements at increasing temperature (Room Temperature, 200 °C, 400 °C and 600 °C) for a constant irradiation time of 45 minutes. The results are shown in Fig. 3.15, along with sputter yield measurements from Gamero *et al*. and Ranjan *et al*.

The sputtering yield ranges from 0.09 to 0.13 $mm^3/C$ at room temperature, while at 600 °C it lies between 0.22 and 0.234 $mm^3/C$. The small difference depend, as mentioned above, on the direction of sintering. What must be noted is that, despite the small difference, both show an almost linear increment with temperature, and the difference seems to decrease with temperature. Another important point is the increase of sputter yield already at very low temperature, much lower that the temperatures at which sublimation should begin. The sputter yield at 600 °C is about twice the value at room temperature.

An effort was made to implement the effect of temperature on the previous model, presented in section 3.3.1, which would increase the sputter yield. There are, however, some key trends that are not investigated by the study of Parida *et al*.

There is no information on the effect of temperature at lower energy where, according to the adatom and the inclusion models mentioned above, the effect of temperature may be greater, hence the sputter yield may be more than doubled at 600 °C. Moreover, Parida *et al*. analysed the sputter yield only at an incidence of 55°, which leaves no information about how sputter yield may vary with angle. Again, since particles impacting with greater angles with respect to the surface normal may interact more with the lattice closer to the surface, the effect may be more pronounced at higher angles.
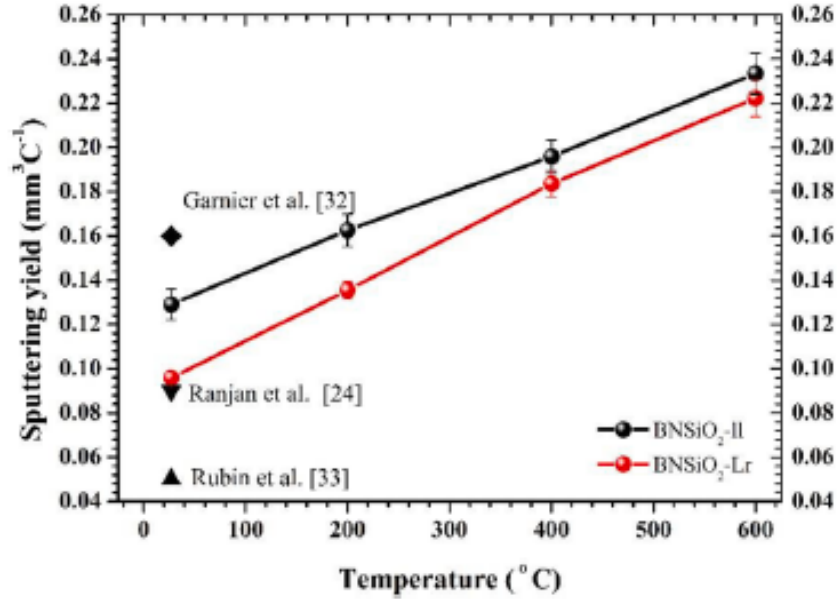
**Figure 3.15:** Sputter yield variation with temperature, from room temperature to 600 °C, for $Xe^+$ impacting on borosil ceramics at 55° angle of incidence, with an energy of 500 $eV$ [25].

Lacking those important information, a linear increment with temperature was assumed, as found by Parida *et al.*, which remains constant with both angle and energy. This means that each value of sputter yield measured by Ranjan *et al.* that was used in the previous model gets multiplied by a coefficient, which will be called *temperature coefficient* ($C_T$), that is equal for everyone. The result of this effect is shown in Fig. 3.16.

The dots in green represents the original sputter yield data by Ranjan *et al.*, while the ones in red are the sputter yield value multiplied by $C_T$ which is, in this case, equal to 2.5. At higher energies, being the sputter yield greater, the difference between the values by Ranjan *et al.* and the ones accounting for the temperature will be more pronounced.

For the extrapolation of data beyond the experimental ones, remains valid the hypothesis that at 90° angle of incidence the sputtering nullifies. Below 100 $eV$, however, it was maintained the average gradient already used before, that is the average gradient of Ranjan's data at any given angle, for two reasons:

- The effect of temperature at different energies is unknown, and changing the gradient would imply making assumptions on such effect. Also, Ranjan's data at room temperature is the only widespread data on which it is possible to rely on;

46
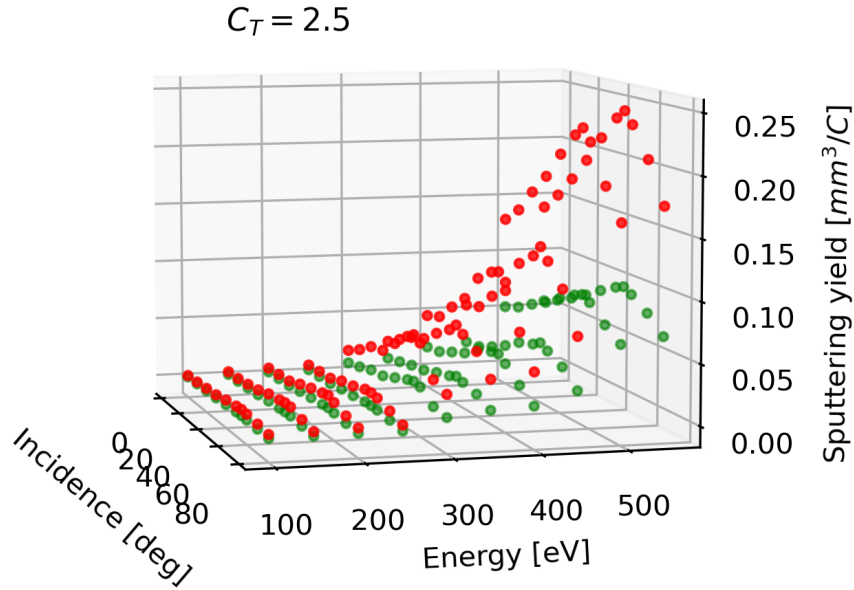
**Figure 3.16:** Comparison of sputter yield data by Ranjan *et al*. [41] in green dots. In red dots is shown the sputter yield considering a temperature coefficient $C_T$ of 2.5, hence the sputter yield data by Ranjan *et al*. multiplied by $C_T$.

- Maintaining the same gradient for the extrapolation below 100 *eV* implicates a reduction in the minimum energy at which sputtering first occurs as temperature increases. As mentioned above, as temperature increases the bond strength may decrease, allowing for atoms to be sputtered from the surface at lower energies. This is yet another assumption, but seen the uncertain value assigned to it in past models seemed a reasonable one.

**Effect of temperature coefficient**

The most obvious effect of temperature is the increase in sputter yield, an increase more pronounced at higher energies, as can be seen in Fig. 3.17, for different temperature coefficients at an incidence angle of 40°.

In the zoom window, can be seen how, extrapolating the sputter yield below 100 *eV* with a constant gradient independent of $C_T$, the energy at which zero sputter occurs lowers. This concept is shown, for all incidence angle in Fig. 3.18. As the temperature increases, hence the $C_T$, the energy at which sputtering begins decreases for every angle of incidence. The difference is greater at 55° of incidence, where the sputter yield is maximum at a given energy.
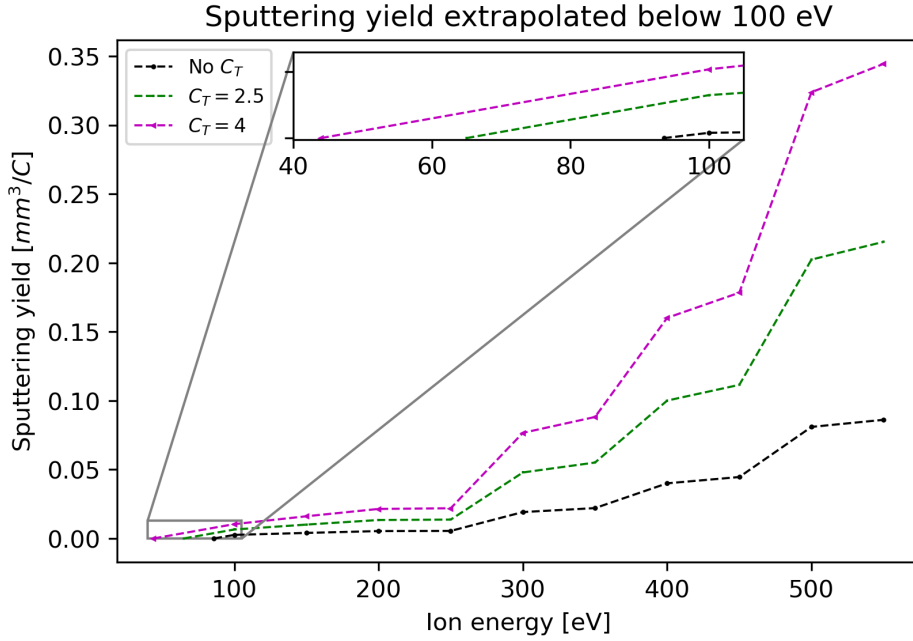
**Figure 3.17:** Representation of sputter yield with the effect of the different temperature coefficient for an ion incidence angle of 40°, and the extrapolation below 100 $eV$.

### 3.3.3 Sputter yield function

Now, considering the effect of temperature, the model used before is further developed accounting for it. The resulting function follows the curve in Fig. 3.19. Compared to the sputter yield function without the temperature coefficient (Fig. 3.13), can be seen that the surface extends further below 100 $eV$, due to the lowered threshold energy and that the sputter yield is increased.

With this function, the erosion simulations have been launched to predict the erosion profiles up to 1000 hours of operation.

## 3.4 Plasma model

As mentioned in chapter 2, the developed erosion model is based on the plasma model developed by Panelli *et al.* called HYPICFLU. Here, a little more detailed explanation of the code will be given to help understand the concept beind the erosion model, without going too deep on detailed formulas.

The code requires as input a 2D grid of the simulation region and the thruster's magnetic field, which is considered to remain constant. Heavy particles are modeled
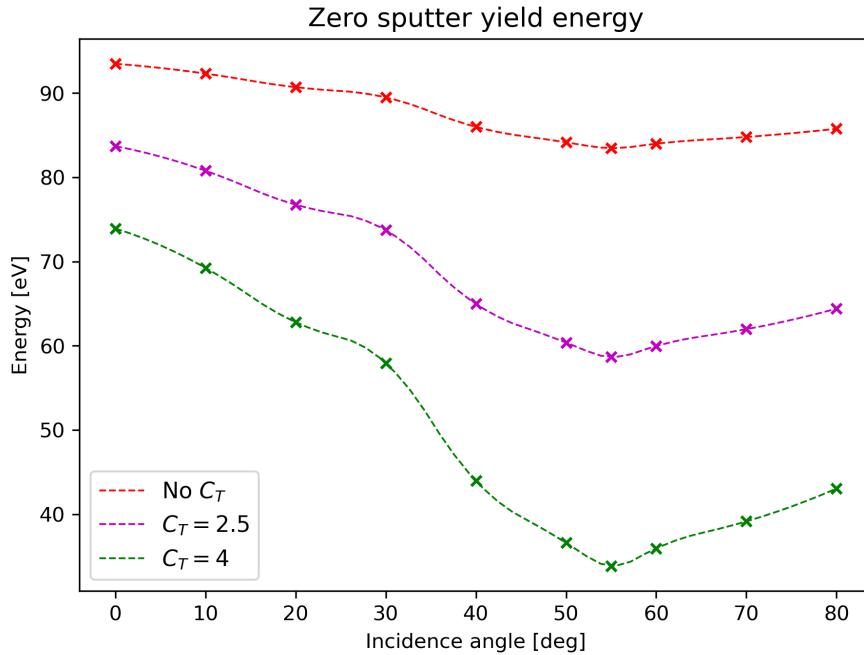
**Figure 3.18:** Extrapolated zero sputter yield energy for different temperature coefficients, for all available incidence angles.

with the PIC method, while the Fluid sub-model is used for electrons. Quasi neutrality is assumed, and a proper sheath model is used in the fluid equation to account for plasma interaction with the walls.

### 3.4.1 Heavy particles

Each simulated particle actually represents an agglomerate of real particles, ranging from $10^8$ to $10^{12}$, called macro-particle. Each macro-particle is characterized by a specific weight, representing in fact the number of particles contained, and in general varies among particles and in time. Only neutral-electron collisions are modeled, which is assumed to be the only contribution to ionization, and only single ionized ions are considered. Ionization rate, hence, depends on electron ($n_e$) and neutral number densities ($n_i$) - for quasi-neutrality $n_e \approx n_i$ - and on the ionization coefficient, which is a function only of the electron temperature. Neglecting neutral-ions collision excludes the possibility for charge exchange (CEX) which consideration would be computational demanding and would have a very limited effect on thruster's performance.

The governing equations are the laws of dynamics, in particular the second one, which determines the acceleration $\vec{a}$ of a particle subject to an electric ($\vec{E}$) and
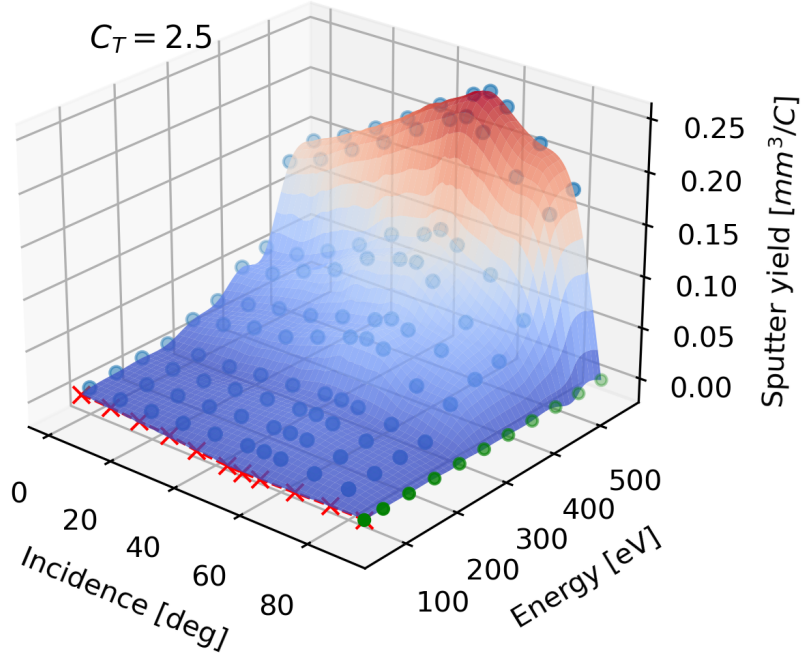
**Figure 3.19:** Representation of the putter yield function, accounting for a temperature coefficient of 2.5. Red crosses are the data extrapolated below 100 eV, green dots are the extrapolated sputter yields at 90° of incidence.

magnetic ($\vec{B}$) fields given its mass ($m$), initial velocity ($\vec{u}$) and charge ($q$). However, due to their high mass, ions may be considered not influenced by the magnetic field (their Larmour radius is much larger than the typical channel length) hence the equation may be reduced to:

$$\vec{a} = \frac{q}{m}\vec{E} \tag{3.2}$$

Neutrals, having no charge, have no acceleration.

The equation is then integrated over time in order to upgrade particles' velocity and position. The time step of integration is chosen such that the distance travelled by a particle is not grater than the typical length of a cell so that a particle will not cross more than one cell for each iteration. Electric field, required to push ions is calculated by a fluid sub-model, interpolated to the grid nodes and successively gathered to particle position. At the end of each time-step, particle velocity and mass are scattered to the grid nodes. This information, along with ionization rate, is used as the input to solve fluid equations.

### 3.4.2 Electrons

Electrons are modeled as a continuum and are defined via: the electrons momentum equation, current conservation and electron energy equations.

Electrons in the acceleration region are magnetized and can be assumed to reach thermal equilibrium along a magnetic field line. Integrating the electrons momentum equation in time it is possible to obtain:

$$\phi^*(\lambda) = \phi_0 - \frac{K_B T_{e,0}}{e} ln(n_{e,0}) \tag{3.3}$$

where $\phi$ is the plasma potential, $K_B$ the Boltzmann constant, $e$ the electron charge and $T_e$ the electron temperature. $\phi^*(\lambda)$ is known as the thermalized potential and is constant along magnetic field lines and allows to reduce the dimensions of the problem to quasi-one-dimensional. This means that both the potential and electron temperature are constant along the magnetic field lines ($\lambda$), while varying with them. Uniting Eq. 3.3 with electron diffusion across the magnetic field, which is assumed to obey generalized Ohm's Law, one can derive that the electron velocity across the magnetic streamlines depends on electron temperature and thermalized potential, hence it is a function of $\lambda$. However, the classical description of diffusion is not adequate to account for the observed anomalous transport, hence a term accounting for plasma turbulence and collisions with neutrals, ions and walls has been added. The electron energy equation is formulated considering both elastic and inelastic collisions. The electron equations are then solved iteratively while the quantities related to the heavy particles are kept constant. More details about the process can be found in the paper by Panelli *et al*. [15].

### 3.4.3 Mesh generation

The computational domain is chosen in order to include the channel walls, on which the erosion model is applied, the internal channel and part of the plume region for the plasma simulation. The area is meshed using a uniform Cartesian grid (via an elliptic mesh generation code), chosen for the simplicity it offers in its construction and computation of gradient fields and the sorting and weighting methods used. It can help avoiding undesired non-physical effects which may appear on highly deformed meshes. The finer the grid is, the smaller the cells, hence the grater the accuracy of the simulation will be. However, the smaller the cells in a given area, the more cells and nodes are needed, requiring a greater computational cost. A cell size was then selected as a compromise between accuracy and computational cost.

Having an axisymmetric geometry, only a section of the thruster may be modeled, as shown in Fig. 3.20a. The boundary of the domain is subdivided in intervals that defines the nodes on which the grid will then be generated. An example of a simulation domain is shown in Fig. 3.20b. The left boundary represents the anode,

where the inlet is. The bottom and top of the domain represents the wall, while the right limit represents the near plume region.
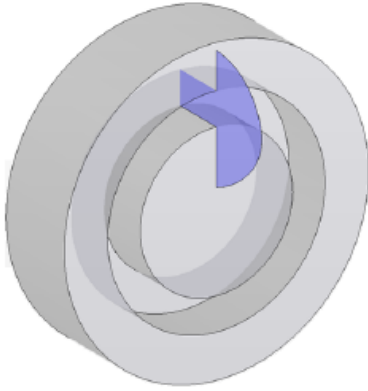


**(a)** Schematic section on an HET thruster [49]
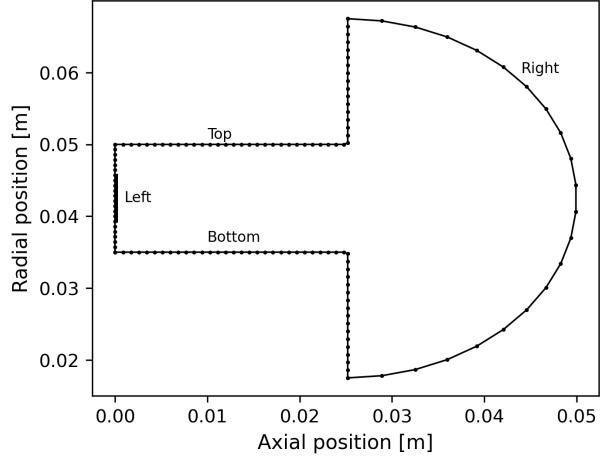
**(b)** Definition of boundary nodes.

**Figure 3.20:** Representation of the simulation region.

The initial computational mesh generated from the boundary of Fig. 3.20b is represented in Fig. 3.21. As the lifetime of the thruster is simulated, the mesh is updated at pre-defined intervals to reflect the regression of the ceramic channel walls. The eroded wall profile is used to refresh the boundary nodes on which the new mesh is generated. An example of an updated, eroded, mesh is shown in Fig. 3.22. The updated mesh is then used as input for the next plasma simulation.

### 3.4.4 Magnetic field calculation

The magnetic field of interest is reproduced using a FEMM (Finite Element Method Magnetics) software, adjusted until the trend of radial magnetic field along the channel centerline and the value at the exit section are in accordance with literature values. The knowledge of magnetic fields allows for the calculation of the magnetic field lines ($\lambda$), and to build fluid meshes. The magnetic field is then interpolated on the PIC grid and is updated each time the geometry is updated due to the erosion simulation. The magnetic field remains unchanged as geometry varies, however erosion expands the domain and the magnetic field needs to be evaluated in those new areas for the next simulation. An example of a magnetic field interpolated on the PIC, non-eroded, grid is shown in figure 3.23.
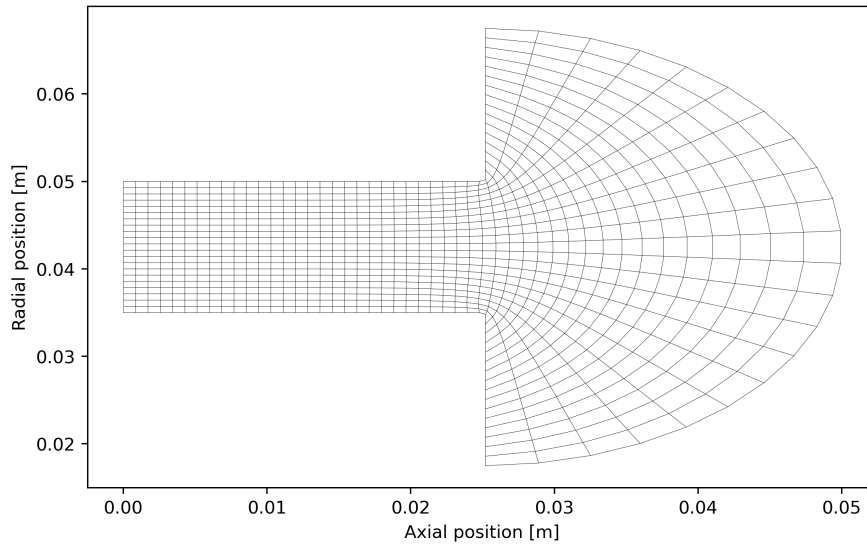
**Figure 3.21:** Example of initial computational mesh.
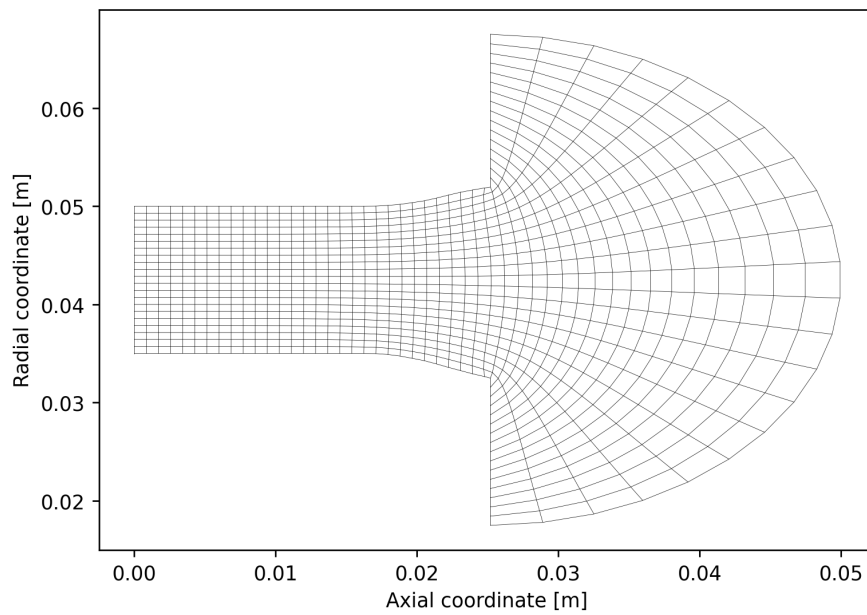


**Figure 3.22:** Example of eroded computational mesh.

## 3.5   Lifetime prediction model

To evaluate the erosion of the channel, a process similar to that used by Gamero-Castano [37] was followed.
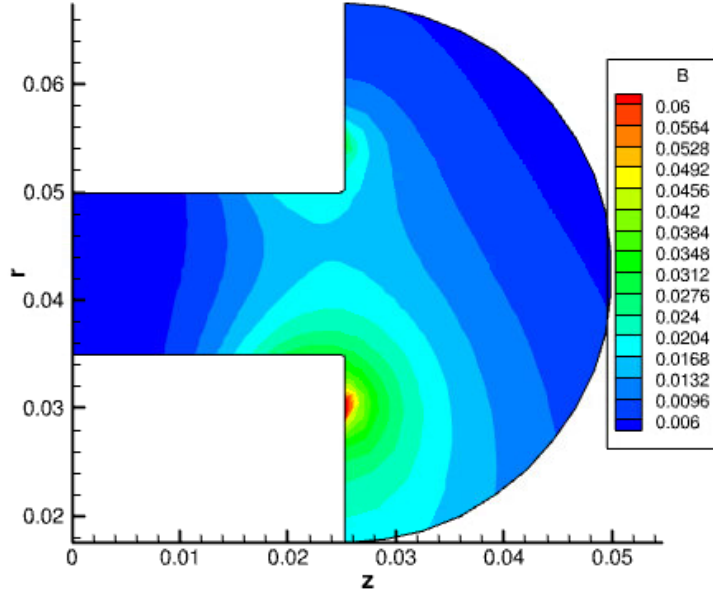
**Figure 3.23:** Representation of the magnetic field in the simulated domain.

An initial mesh, representing the computational domain is generated following a given geometry. Then the PIC and Fluid grid are generated and used as input to the HYPICFLU code for the plasma simulation. From the HYPICFLU code ion density at nodes and ion velocity are extracted and used as inputs to the erosion model, along with the grid file, containing the coordinates of the surface nodes. Given the ion velocities at nodes, already comprising the Bohm condition, which is modeled in the plasma code, and the surface normal it is possible to evaluate the incidence angle. It was decided to assign the incidence angle $\Theta_i$ to the $i_{th}$ node considering the normal to the surface section included between the $i_{th}$ and the $i_{th-1}$ nodes, as schematically shown in Fig. 3.24, where $v_i$ is the ion velocity. A condition has been set that, for $\Theta \geq \pi/2$, no sputtering occurs since the flow is either parallel to the surface or divergent.

Then, known the ion velocities at nodes, the ion energy can be easily computed via equation 3.4:

$$E_i = \frac{1}{2}\frac{m_{Xe}}{e}v_i^2 \tag{3.4}$$

where $m_{Xe}$ is the ion mass, $e$ the electron charge which, indeed, is identical to the ion charge. These two elements are then used as input in the sputtering function (section 3.3), which returns the volumetric sputter yield $Y$.
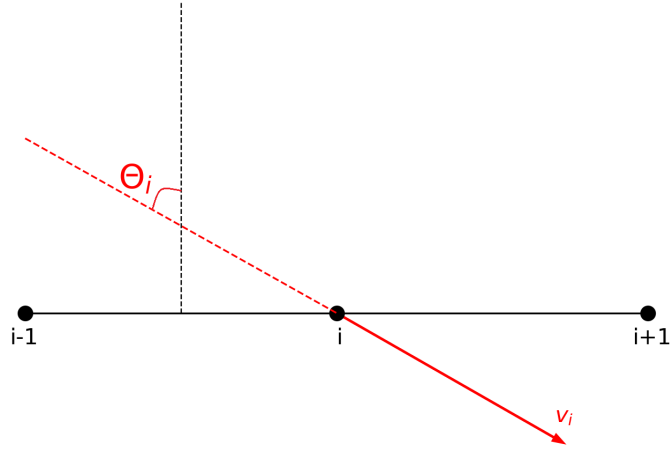
**Figure 3.24:** Schematic representation of how the incidence angle is calculated.

The ion flux associated with the channel wall node $J_{iw}$ is give by Eq. 3.5 where $n_i$ is the ion density at the nodes and $v_y$ is the ion velocity normal to the surface, which already considers the Bohm condition.

$$J_{iw} = n_i v_y e \tag{3.5}$$

With the ion flux and the volumetric sputter yield is possible to evaluate the erosion rate of the wall at a given node. Then, fixed an operation time $\Delta t$ of 60 hours per iteration, in accordance to Ref. [37], the nodes are moved to allocate the new channel wall profiles. The new geometry extracted is then used as input in HYPICFLU for a new plasma simulation.

The erosion simulation proceeds then as schematically shown in Fig. 3.25 until the desired operation time is reached.
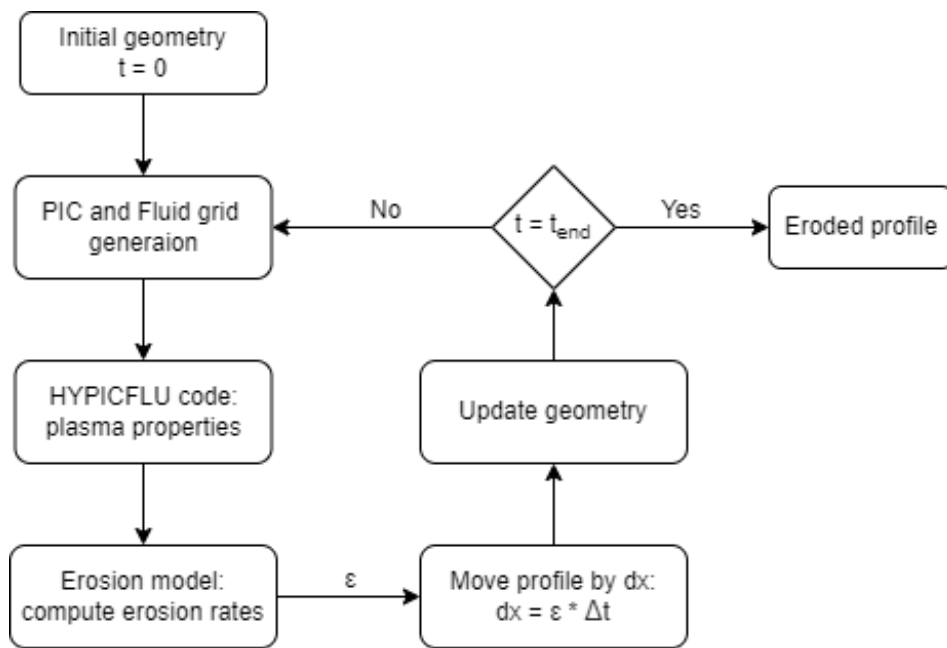
**Figure 3.25:** Flow diagram for the erosion simulation.

# Chapter 4

# Results

In this chapter are shown the results of the erosion simulation for the SPT-100 thruster. First the thruster and the tuning parameters are described. Then the erosion simulation is run to predict erosion profiles un to 1020 hours of operation, in time steps of 60 hours.

## 4.1 Reference Thruster: SPT-100



**Figure 4.1:** SPT-100 picture, from Ref. [50].

The SPT-100, where SPT stands for Stationary Plasma Thruster, is an Hall Effect Thruster manufactured by Russian EDB Fakel. It was first launched in 1994. In the following years, other versions of the SPT-100 were developed and were used in many spacecraft such as IPSTAR-II, Telstar-8, and Ekspress. It uses Xenon as propellant, and has an outer hollow cathode configuration (as schematically shown in Fig. 2.1a), and borosil as ceramic coating for the channel walls. Fig. 4.1 shows a picture of the SPT-100, while the main performance are shown in Tab. 4.1.

| Parameters | Value |
|---|---|
| Propellant | Xenon |
| Power [W] | 1350 |
| Discharge voltage [V] | 300 |
| Discharge current [A] | 4.5 |
| Thrust [N] | 0.083 |
| Specific impulse [s] | 1540 |
| Efficiency | 0.45 |
| Power-to-thrust ratio [W/mN] | 16,3 |
| Lifetime [hrs] | >9000 |
| Mass [kg] | $\sim 4$ |

**Table 4.1:** Main performance of SPT-100 [50].

SPT-100 has been chosen as the reference engine due to the large availability of data in literature and its great adoption. The main characteristics of the thruster are reported in Tab. 4.2.

| Parameters | Values |
|---|---|
| Channel length [m] | 0.025 |
| Channel width [m] | 0.015 |
| Inner radius [m] | 0.035 |
| Inner radius inlet [m] | 0.04 |
| External radius [m] | 0.05 |
| External radius inlet [m] | 0.045 |
| Mass flow rate [kg/s] | $5 \cdot 10^{-6}$ |

**Table 4.2:** SPT-100 channel dimensions and nominal operating condition.

## 4.2   Simulation parameters

In this section the initial parameters of the simulation are described, as well as the process followed to advance the erosion simulation through its virtual life test. The sputter yield data used are the ones by Ranjan *et al.* of *borosil* impacted by *Xe* ions.

### 4.2.1   Baseline mesh

The computational domain is a rectangle followed by a semicircle that, starting from the anode, includes the channel and part of the near plume region. From this, the mesh is generated. The initial mesh is a $47 \times 22$ cartesian grid based on the thruster's geometry, as shown in figure 4.2. The number of nodes on the upper wall coincides with the number of nodes on the bottom wall, and the same applies to the left and right boundary representing, respectively, the anode and the cathode. The bottom and upper surfaces of the channel are made of borosil, a mixture of $BN$ and $SiO_2$, and are subject to erosion during the lifetime of the thruster.
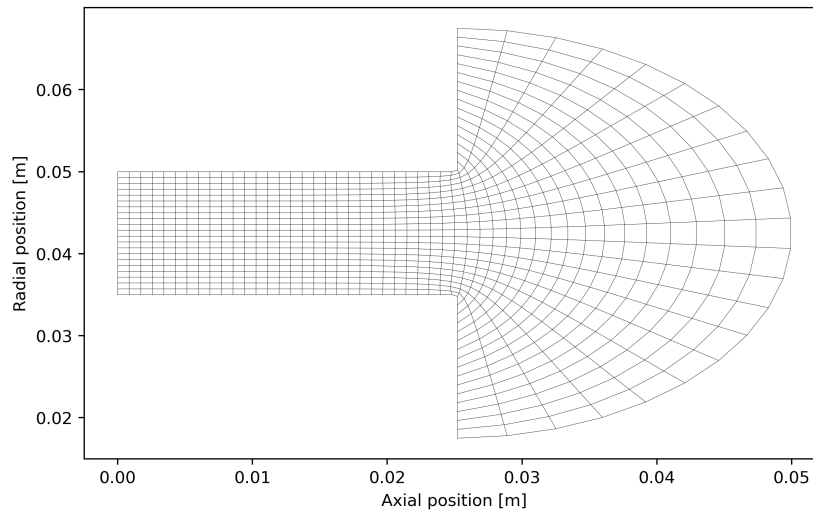


**Figure 4.2:** Baseline computational mesh.

### 4.2.2   Baseline magnetic field

The initial magnetic field is depicted in Fig. 4.3, where are shown both the magnetic field and the magnetic streamlines. The magnetic field is stronger towards the center of the thruster, where the magnetic lines converge. As the thruster's geometry

59

**(a)** Magnetic field.

**(b)** Magnetic streamlines.
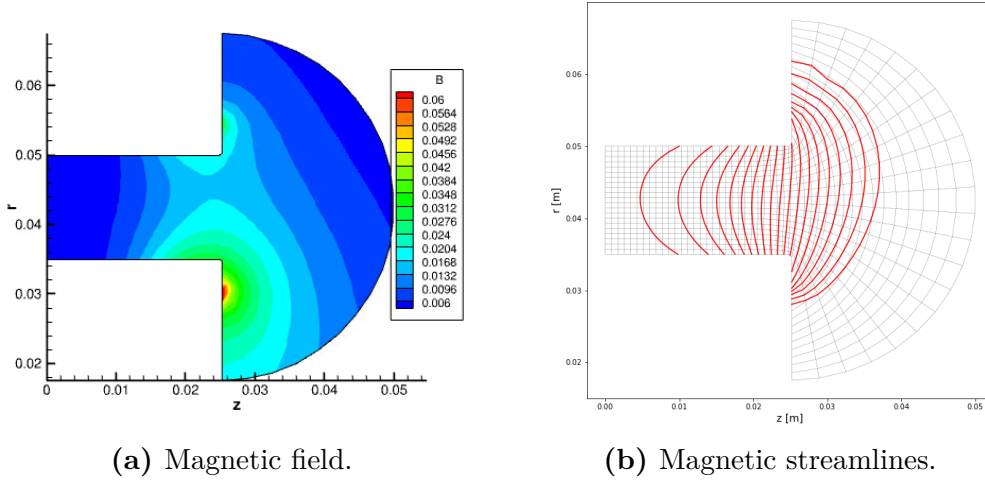
**Figure 4.3:** SPT-100: initial magnetic field and magnetic streamlines.

evolves the magnetic field is recomputed in order to account for the expansion of the computational domain.

The cathode is a magnetic streamline that represents the external boundary of the fluid domain.

### 4.2.3   Input parameters

Table 4.3 summarizes the main parameters used as input in Hypicflu that specify the simulated thruster operation. The PIC time-step is chosen such that one macro-ion does not advance more than one cell per each time-step, while the Fluid pseudo time-step is selected to ascertain that the fluid solver converges. The channel wall temperature is assumed to be 850 $K$, in accordance with what is reported in Ref. [51].

## 4.3   Influence of temperature coefficient

As seen in section 3.3.2, the temperature coefficient ($C_T$) influences the threshold energy and the sputter yield at all energies and angles. It has then, as will be seen, an effect on erosion as well. As mentioned in the previous chapter, the greater the temperature coefficient is the greater the sputter yield is. The effect, since it was assumed to be linear, is more pronounced towards higher energies, as shown in Fig. 3.16. Following the experimental results by Parida *et al.* [25] of the increase in sputter yield with temperature, as reported in Fig. 3.15, there is an increase of sputter yield by about a factor of two at 600 °C which is in the temperature range

| Parameters | Values |
|---|---|
| Grid | $47 \times 22$ |
| PIC time-step [s] | $5 \cdot 10^{-8}$ |
| Fluid time-step [s] | $2 \cdot 10^{-10}$ |
| Neutrals specific weight | $2.5 \cdot 10^{11}$ |
| Ions specific weight | $2.5 \cdot 10^{9}$ |
| Number of particles simulated | $\sim 45000$ |
| Anode temperature [K] | 750 |
| Wall temperature [K] | 850 |

**Table 4.3:** Main parameters of the test.

of HETs accelerating channel during operation. In particular, the samples which have a perpendicular orientation of sintering and are closer to the data reported by Ranjan *et al.* at room temperature, show an increase by a factor of $\sim 2.3$.

This value was chosen for the erosion simulation, and the erosion profiles obtained were compared to the experimental profiles. The simulation time-steps were of 60 hours, after which the plasma simulation was run with the new geometry and plasma values were updated accordingly. The erosion profiles predicted for the first 300 hours are shown in Fig. 4.4.

As can be seen, the erosion profiles are strongly under predicted. The experimental erosion begins much further up the channel, at around 17 *mm*, than what is predicted by the model, which is around 21 *mm*. The model also fails to capture the magnitude of the erosion.

In an effort to get closer to the experimental profiles, the temperature coefficient was increased, and the effect was noticeable. The profiles obtained varying $C_T$ are reported in Fig. 4.5. The temperature coefficients chosen were:

- $C_T = 1$: which means that there is no effect on the sputter yield magnitude;

- $C_T = 3$: is a value slightly higher than the one reported by Parida *et al.* at 600 °C;

- $C_T = 5.5$: a value that is approximately twice the value reported by Parida *et al.*

The simulation was run for five time-step of 60 hours, up to 300 hours of simulated lifetime and are shown at 180 and 300 hours, in order to evaluate the effect of $C_T$. This increment has an effect both on the erosion magnitude and on
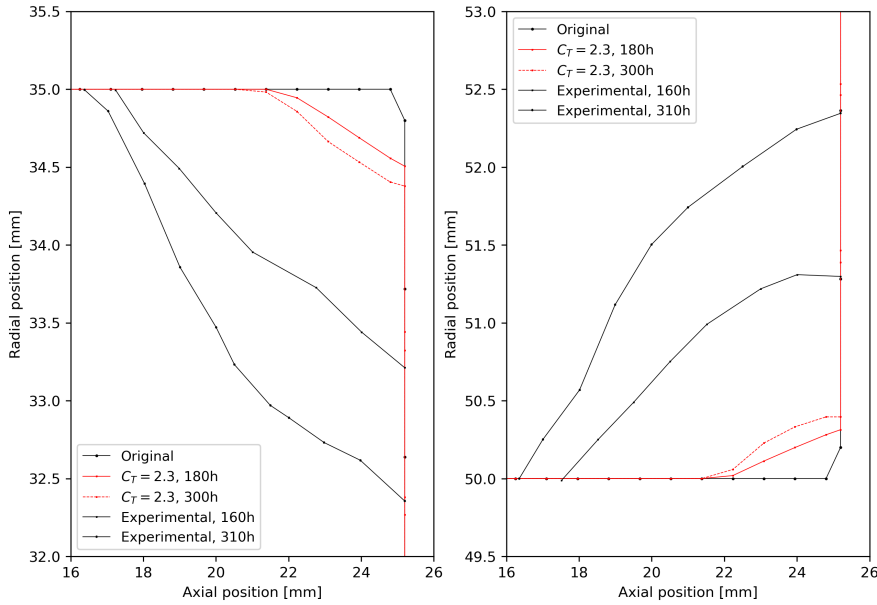
**Figure 4.4:** Predicted and experimental erosion profiles, for the first 300 hours of operation, with a temperature coefficient of $C_T = 2.3$.

the beginning of the erosion. As expected, the erosion increases as the temperature coefficient increases. In particular, for a $C_T$ of 5.5, the erosion magnitude increases from 0.35 to 1.17 $mm$ at the point of maximum erosion of the lower surface, that is the node just before the chamfer of the channel exit. For the upper surface it it increases from 0.25 to 1.01 $mm$ at the point of maximum erosion. The beginning of erosion retreats towards the anode by about 5 $mm$ for both the inner and outer surfaces, due to the fact that, since ions accelerate in the channel, their energy is greater towards the channel exit. As $C_T$ increases, the threshold energy decreases, hence erosion begins further upstream, towards the anode. Despite having almost doubled the value of sputter yield increase with temperature measured by Parida *et al.*, the erosion is still under predicted, but the point where erosion begins is more acceptable.

In theory should be possible to increase $C_T$ more, but a problem occurs, considering the linear increment which was assumed, regarding the threshold energy. In particular, as shown in Fig. 4.6, increasing too much the temperature coefficient results in a negative threshold energy which cannot be considered physical. One way to bypass this limitation would be to impose an $Eth = 0 \ eV$ where it becomes negative, but that would imply a strong assumption, not really based on scientific evidence.

In the end we opted to consider a temperature coefficient of 5.5, which leads to
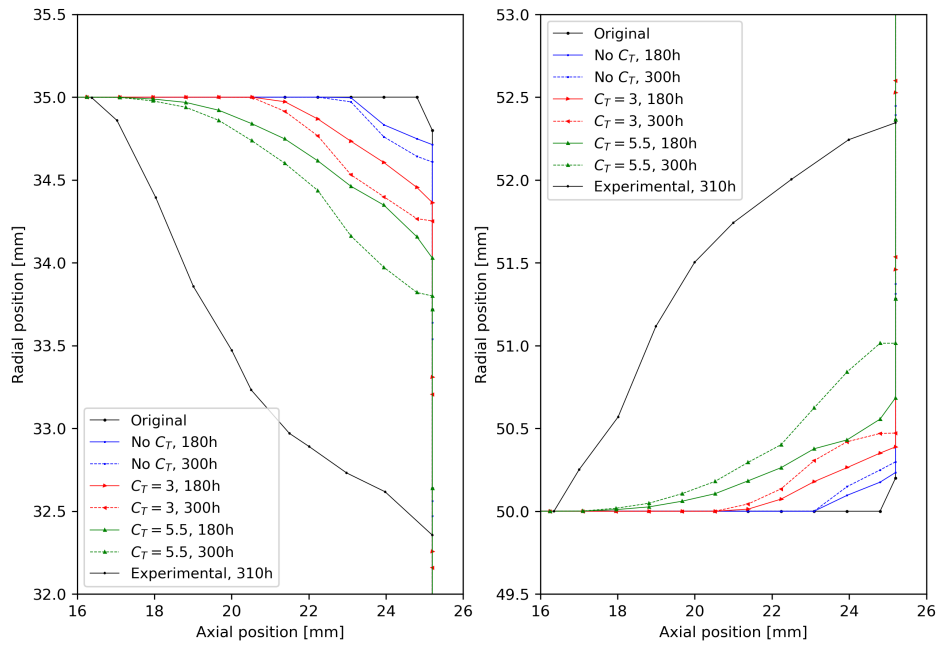
**Figure 4.5:** Predicted erosion profiles for different $C_T$, for the first 300 hours of operation.

a minimum threshold energy of approximately 9 $eV$ at 55° angle of incidence.
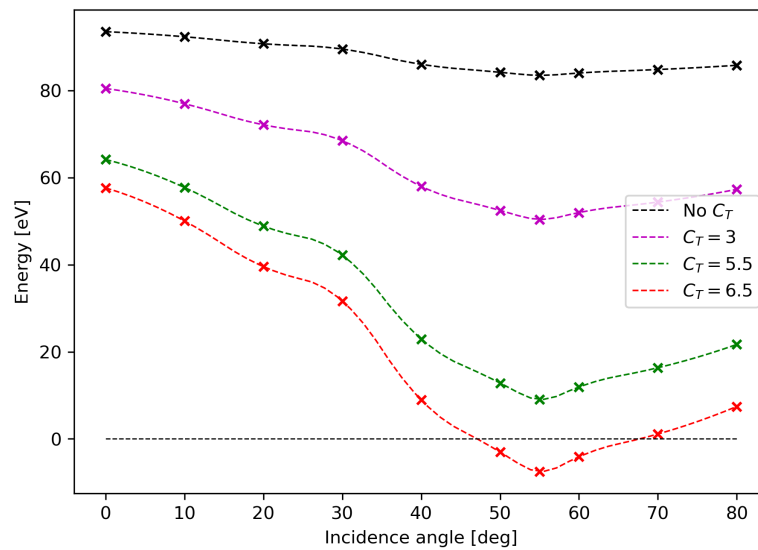


**Figure 4.6:** Threshold energy dependence on $C_T$. The dashed black line represents 0 $eV$.

63

# 4.4   Predicted erosion profiles

In the following section, the erosion profiles simulated considering a temperature coefficient of 5.5 are reported. They will later be compared both to experimental profiles by Absalamov *et al.* ([52]) and the profiles obtained by Gamero-Castano ([37]) since the erosion model used, despite being based on different sputter yield data, is similar. Again, the time-step for the erosion simulation is 60 hours until a cumulative 1020 hours of simulated operation are reached.

In Fig. 4.7 and Fig. 4.8 are shown the erosion profiles for every time-step, for the inner and outer surface respectively. In the first hours of operation the erosion is localized towards the channel exit. As the simulated operation continues the erosion moves further up in the channel, reaching around 17 *mm* from the inlet. The plasma seems to smooth out the unevenness generated by the previous erosion. The amount of erosion of the outer surface of the channel is less than the inner surface, as also observed experimentally. Towards the end of the simulated lifetime the erosion decreases in rate, as can be also seen in Fig. 4.9. The erosion rate increases again where the surface presents protuberances, as happens toward the channel exit in the latter stages of the erosion simulation. In Fig. 4.10 are shown the erosion rates for the outer surface of the channel as well.

In Fig. 4.11 is reported the computed evolution of the channel exit, in terms of erosion in time. As can be deduced from the channel evolution and confirmed by the erosion rates, also the wall recession shows a decrease in speed with time. This result is in accordance with experimental observations, which is characterized by a slowing of the recession in time. The trend is particularly pronounced on the bottom surface of the wall. Again, in the latter stages of the simulation, an increase of the recession is visible, and is due to the greater exposure to plasma of the protruding surface, which is then smoothed out.

A comparison between the experimental erosion observed by Absalamov *et al.* [52] is shown in Fig. 4.12. Despite the temperature coefficient, the erosion is still under predicted for both the inner and outer surfaces, by about 50.1% and 62% for the bottom and upper surfaces respectively. The point where the erosion begin is well predicted by the model for the first hours of operation, while fails to predict the regression of the erosion up the channel. This may be due to the energy of the ions being too low in that region of the channel, below the threshold energy, hence causing no noticeable erosion.

In Fig. 4.13 is also reported the comparison between the computed erosion profiles, the ones with our model and the ones by Gamero-Castano [37] at around 800 hours of simulated operation. The result, still under predicted, by about 52% and 62.2% for the bottom and upper surfaces respectively, is closer for the first few hundreds hours of operation, and shows a similar predicted curvature of the eroded profiles. The curvatures are, however, both different from the experimental

ones. This may suggest that the plasma codes may fail to model some important plasma physics, which may still be not fully understood.
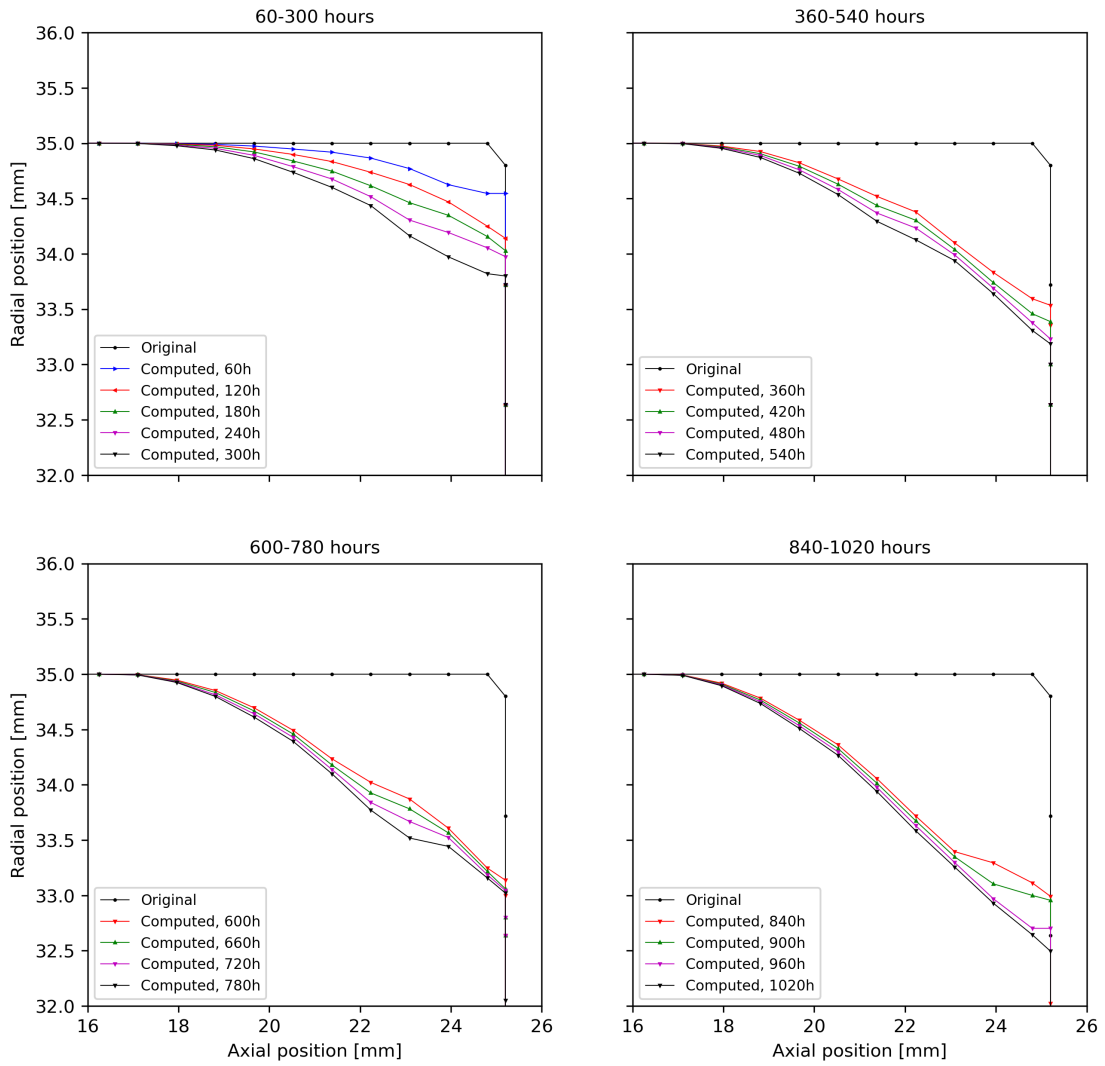


**Figure 4.7:** Erosion profiles for the inner channel surface, for every 60 hours time-step.
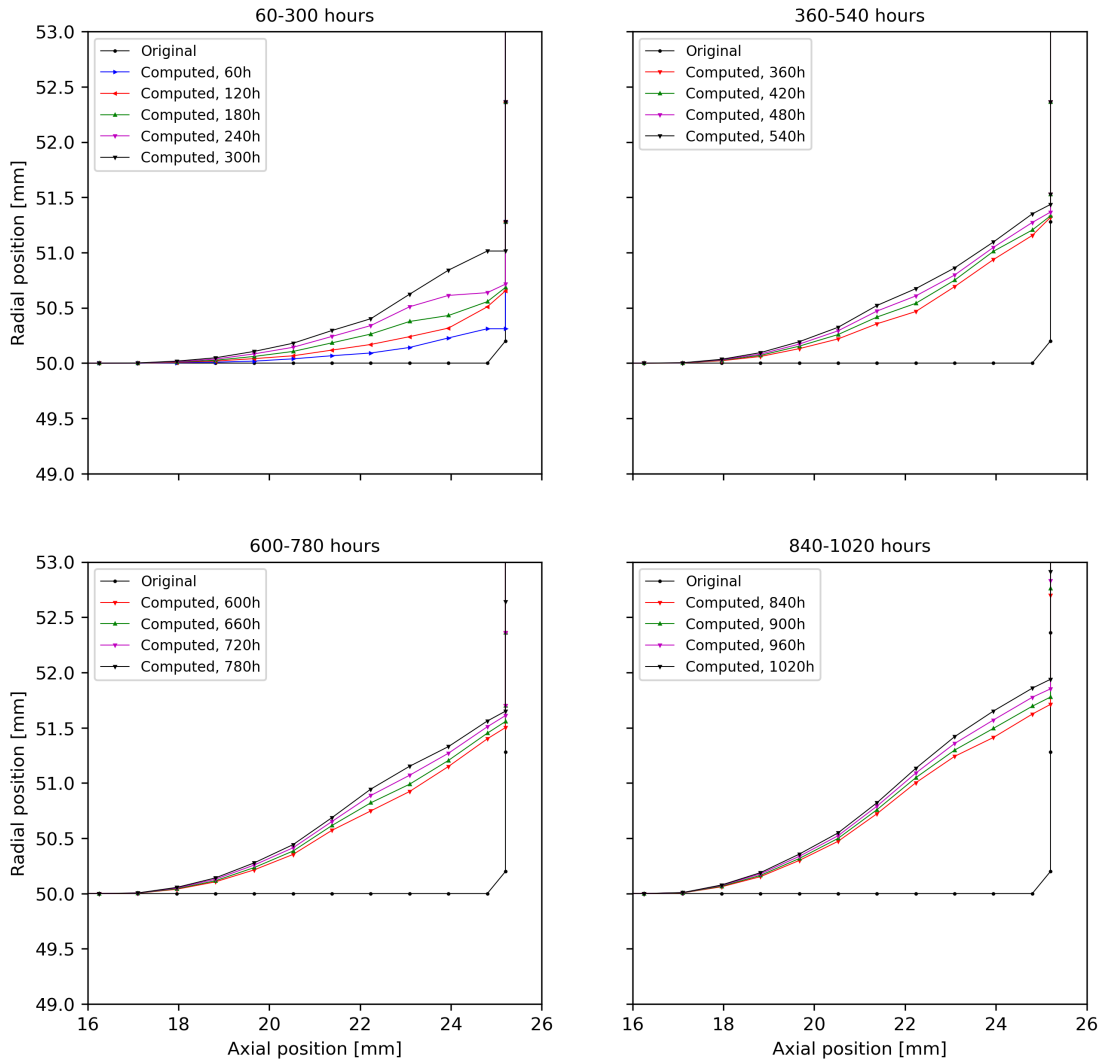
**Figure 4.8:** Erosion profiles for the outer channel surface, for every 60 hours time-step.
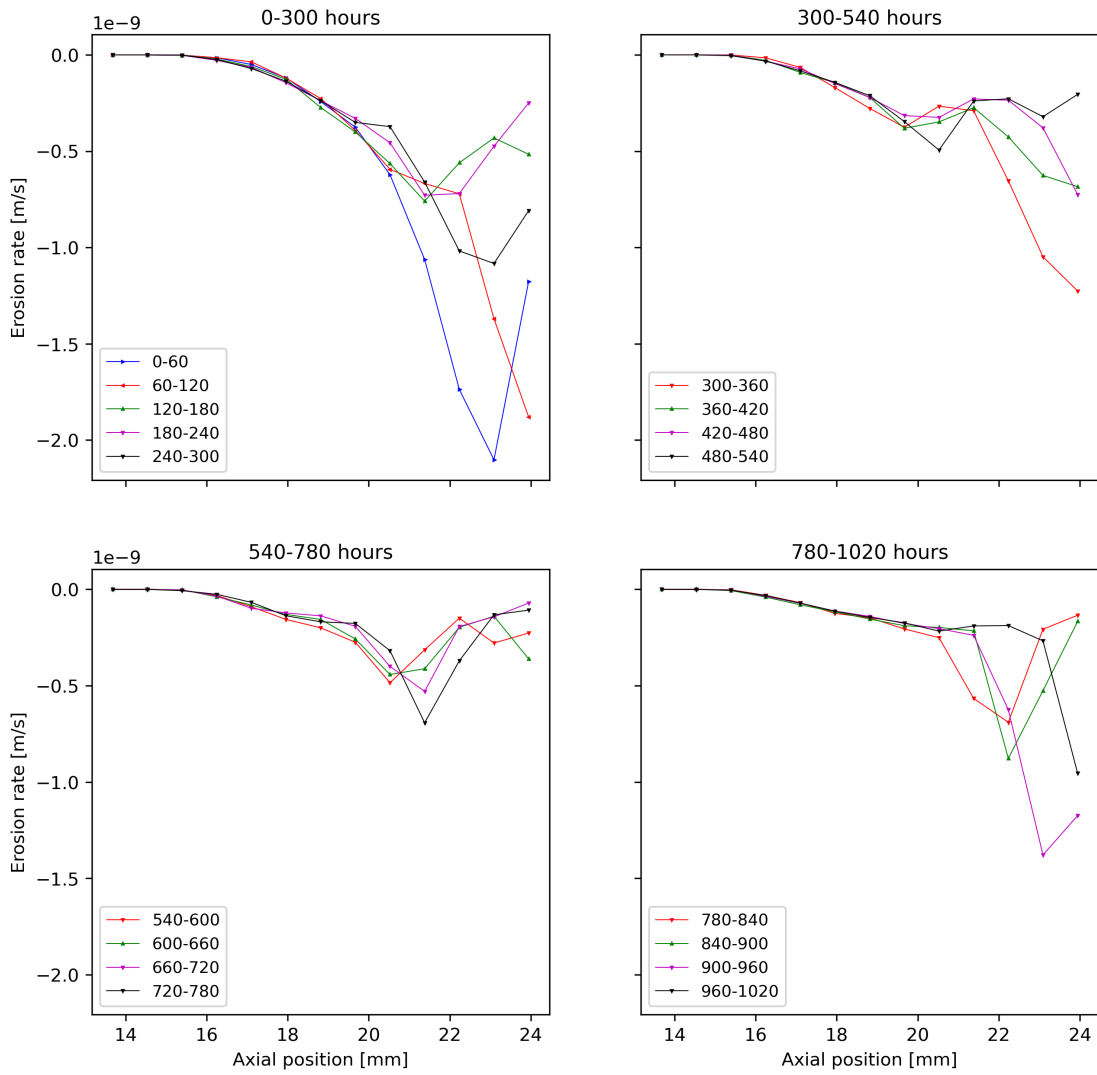
**Figure 4.9:** Erosion rates for the inner surface, in 60 hours time-step.
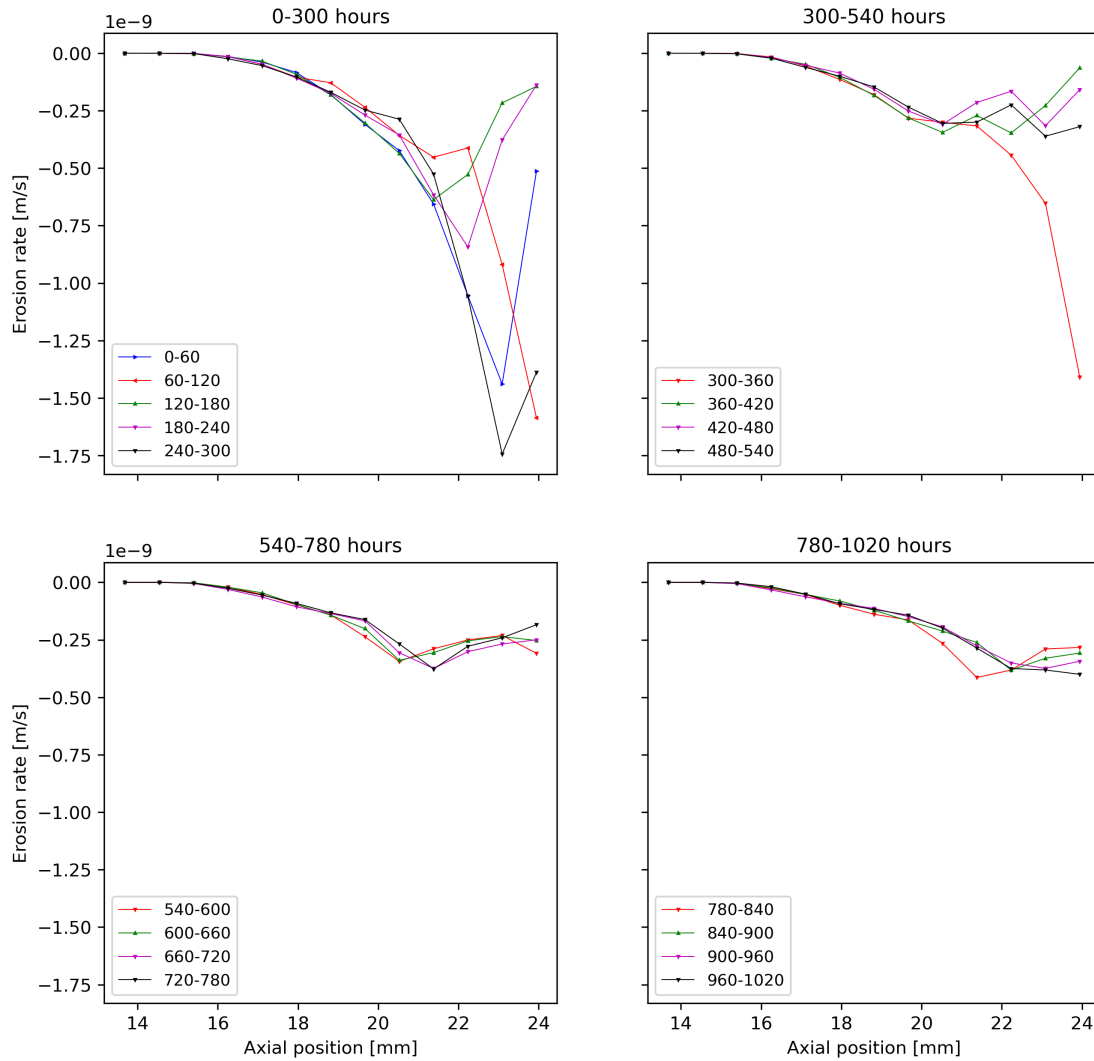
**Figure 4.10:** Erosion rates for the outer surface, in 60 hours time-step.
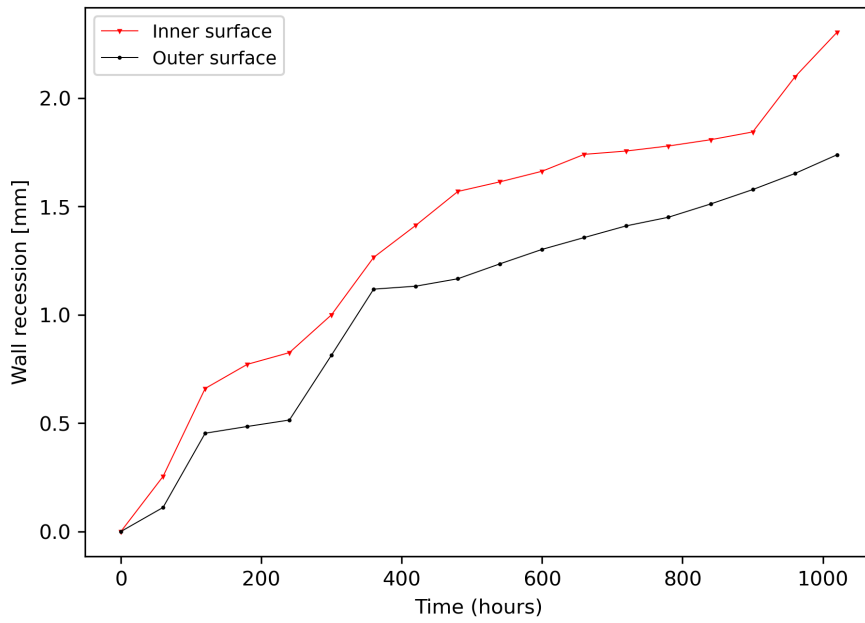
**Figure 4.11:** Computed evolution of channel exit, for the inner and outer channel surfaces.
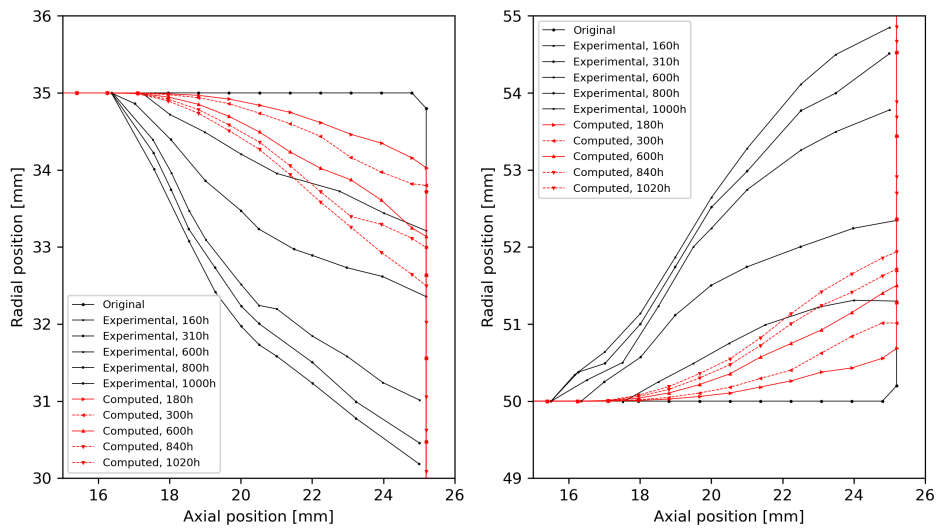


**Figure 4.12:** Comparison of computed and experimental erosion by [52].
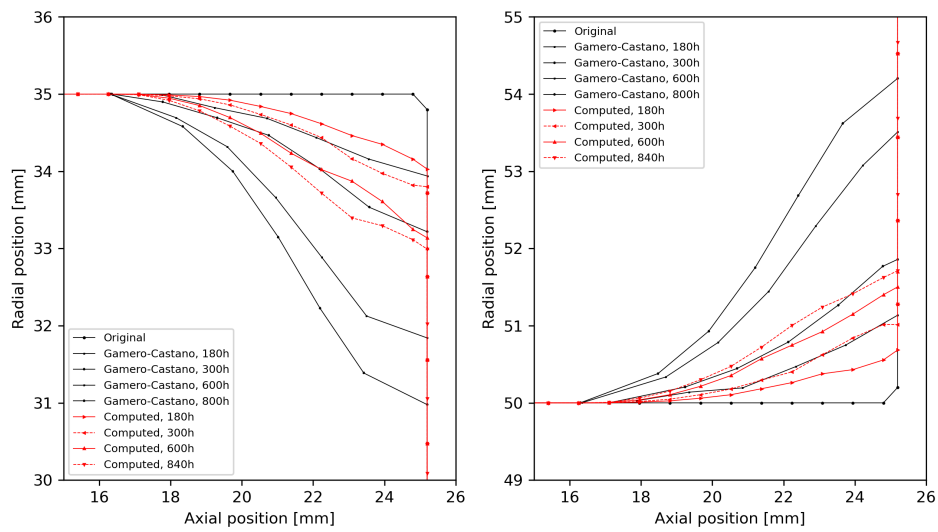
**Figure 4.13:** Comparison of computed erosion profiles, by Gamero-Castano [37] and ours.

### 4.4.1  Performance prediction

During the simulation, the thurster's performance was evaluated at every time-step. The results are shown in steps of 120 hours for compactness.

The discharge current $I_d$ is close to the nominal one, but decreases during simulated operation to settle in around 4 $A$. The efficiency ($\eta$) is a bit higher than the nominal value reported in Tab. 4.1. This may be due in part to the fact that double ionized ions are neglected even tough they may have a significant impact, as well as ions-neutrals and neutrals-neutral collisions, which may influence the performance. The specific impulse ($I_s$) is also slightly higher than nominal, while the thrust $T$ is slightly underestimated.

Overall the predicted performances remain stable during the simulated operation.

| time [hrs] | 0 | 120 | 240 | 360 | 480 | 600 | 720 | 840 | 960 |
|---|---|---|---|---|---|---|---|---|---|
| $I_d$ [A] | 4.12 | 4.08 | 4.01 | 4 | 3.98 | 3.95 | 4.01 | 3.95 | 3.98 |
| $T$ [mN] | 75 | 76.6 | 76.24 | 74.97 | 75.69 | 74.52 | 76.71 | 73.98 | 74.84 |
| $\eta$ | 0.5 | 0.52 | 0.53 | 0.52 | 0.53 | 0.53 | 0.54 | 0.52 | 0.53 |
| $I_s$ [$10^3$s] | 1.65 | 1.54 | 1.67 | 1.66 | 1.67 | 1.68 | 1.68 | 1.67 | 1.68 |

# Chapter 5

# SPT-100 MS results

In the MEMS project at CIRA, an effort was put into developing a methodology for the scaling of *magnetically shielded* (MS) configurations for HETs. The magnetically shielded configuration requires the magnetic field lines to be parallel to the channel surface, as depicted in Fig. 5.1, this way restraining the plasma radial flow, reducing the wall loss and beam divergence loss, improving both the thruster's life, strongly reducing the particle-wall interaction, and its performance. The design of an $MS$ configuration generally requires a trial and error approach, which is time consuming. To speed up the process, a methodology was developed for the design procedure focusing on thrusters with power levels lower than 5 kW [53].

The study of a magnetically shielded configuration of the SPT-100 thruster was conducted, modifying its magnetic circuit and testing its efficacy via plasma simulations with HYPICFLU. Indeed, the results were as expected. The peak of the magnetic field moved outside the channel exit, as shown in Fig. 5.2a, while the electron temperature and wall potential show an increment of the plateau (Fig. 5.2b), as suggested by the theory.

The differences are also on the electron temperature peak, as can be seen in Fig. 5.3 where for the magnetically shielded case the electron temperature peak is shifted towards the channel exit, and with a higher peak value. Must be reminded that, for the sake of comparison, 1 $K$ is equal to approximately $8.62 \times 10^{-5}$ $eV$. The electron temperature peak in the case of the un-shielded configuration is approximately 28-29 $eV$, while in the MS case is above 36 $eV$.

In Fig. 5.4 are reported some magnetic field lines in the domain. As can be seen, for the magnetically shielded configuration, the field lines are more bent in the channel, with a shape more parallel to the channel walls.

Ionization occurs further towards the channel exit in the $MS$ configuration, as can be seen in Fig. 5.5. The ionization also looks to be more concentrated, thanks to the confinement of the magnetic field.
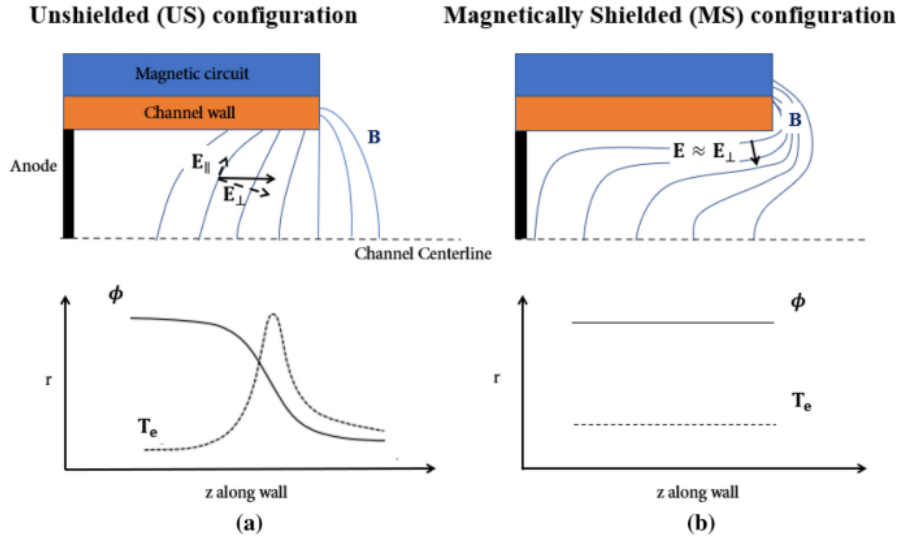
**Figure 5.1:** Comparison between magnetically shielded and un-shielded configurations [53], showing the magnetic field lines in the channel, as well as the potential and the electron temperature.
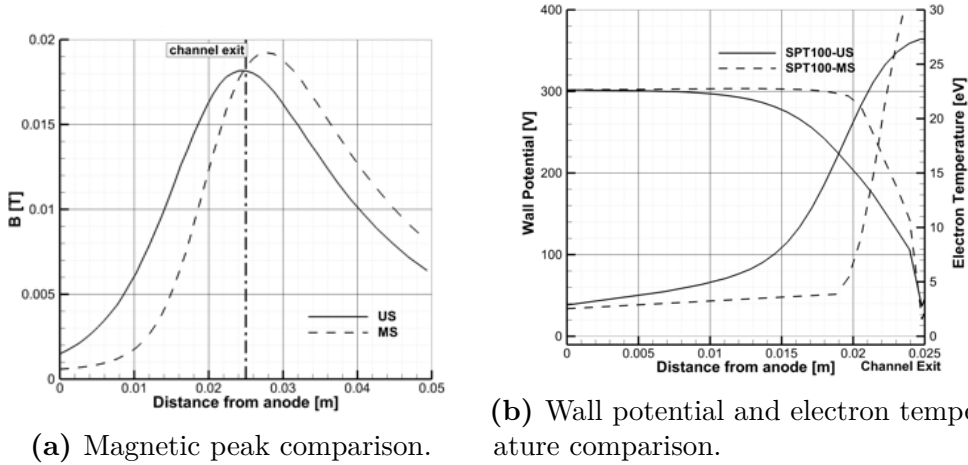


**(a)** Magnetic peak comparison.

**(b)** Wall potential and electron temperature comparison.

**Figure 5.2:** Evolution of magnetic field, wall potential and electron temperature in the channel for $MS$ and $US$ configurations [53].

## 5.1 Predicted erosion profiles

In the following section the simulation results for an hypothetical SPT-100 with magnetically shielded configuration are presented. The simulation parameters are the same used in the un-shielded configuration, reported in Tab. 4.1 and 4.2. The erosion model used is the same as the one used in chapter 4, with the same

**(a)** Electron temperature *US*.　　　**(b)** Electron temperature *MS*.
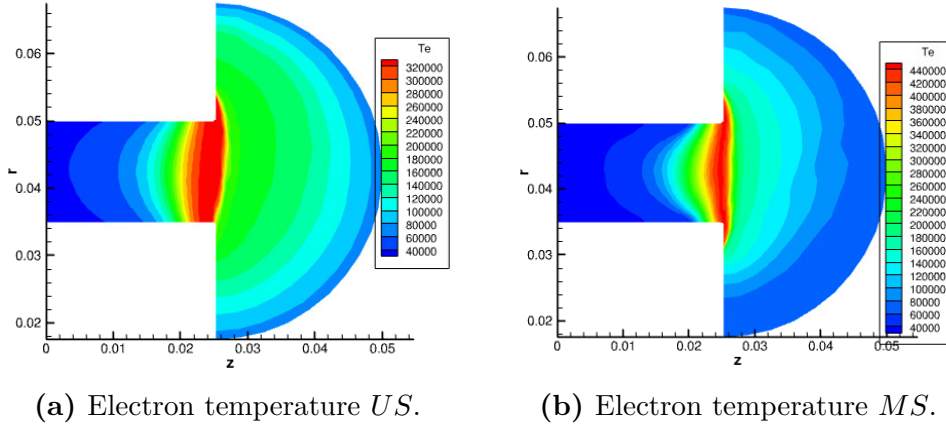
**Figure 5.3:** Comparison of electron temperature in the domain between *US* and *MS* configurations.



**(a)** Magnetic streamlines *US*.　　　**(b)** Magnetic streamlines *MS*.
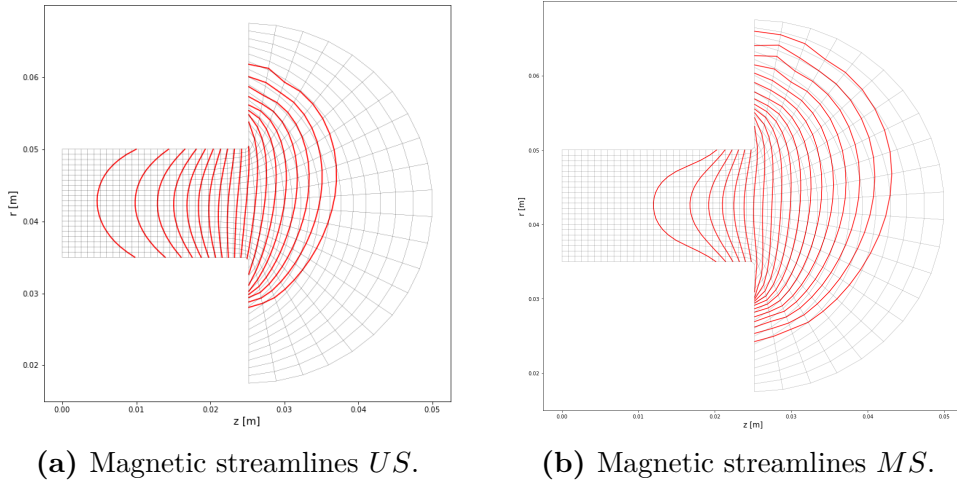
**Figure 5.4:** Comparison of magnetic streamlines between *US* and *MS* configurations.

temperature coefficient. What changes is the plasma inside the channel, due to the different magnetic field. The simulation follows time-steps of 60 hours, until a cumulative simulated operative life of 600 hours is reached.

In Fig. 5.6 and 5.7 can be seen, respectively, the simulated erosion profiles for the inner and outer surface of the channel. The erosion profiles shows a similar curvature to the previous case, but the erosion difference between the inner and outer surface is less pronounced. This may be due the fact that the electron temperature is higher and more concentrated, inducing a smaller difference in ion energy between the inner and outer surfaces. A comparison of the computed erosion

**(a)** Ion density *US*.          **(b)** Ion density *MS*.
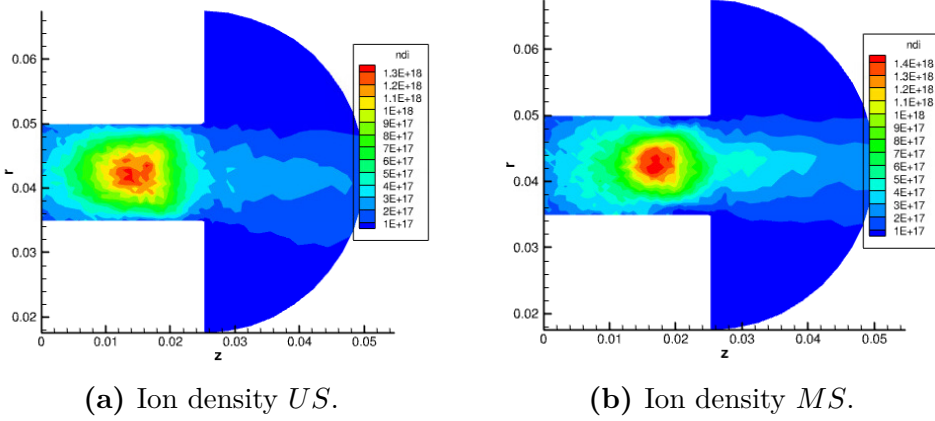
**Figure 5.5:** Comparison of ion density in the channel between *US* and *MS* configurations.

profiles for the Magnetically shielded and un-shielded configurations is shown in Fig. 5.8. It is clearly visible the lower erosion magnitude and that the erosion begins further downstream, that is toward the channel exit. As suggested by the theory, the erosion in the MS case is greatly reduced, from 1.75 *mm* to 0.65 *mm* on the bottom surface of the channel, which is a reduction of 63%, at 600 hours. For the upper surface the erosion in reduced from 1.4 *mm* to 0.68 *mm*, which is a 51.2% reduction. The given values are taken at the point of maximum erosion, that is the node just before the chamfer of the channel exit. Meanwhile, Fig. 5.9 shows the wall recession at the channel exit. Furthermore, the length of the erosion zone is significantly reduced compared to the previous case - it begins at around 21 *mm* from the anode, compared to 17 for the *US* case. That is in accordance with what is seen in literature as, for instance, in Ref. [49].

All what has been said is confirmed by the erosion rates, Fig. 5.10, which for the *MS* case are always lower than the *US* case, and show that the erosion begins further towards the channel exit. It can also be seen that the erosion rate difference between the inner and outer surfaces is less pronounced than the *US* case. This may be due to the fact that, since the electron temperature peak is more concentrated, may induce a lower dependence on radial position of ion energies. The drop of the erosion rate at the channel exit is due to the shape of the edge, which causes the last part of the channel, the one after the chamfer, to erode less in the first hours of operation, as can be also seen in Fig. 5.6 for the first 60 hours, for instance.
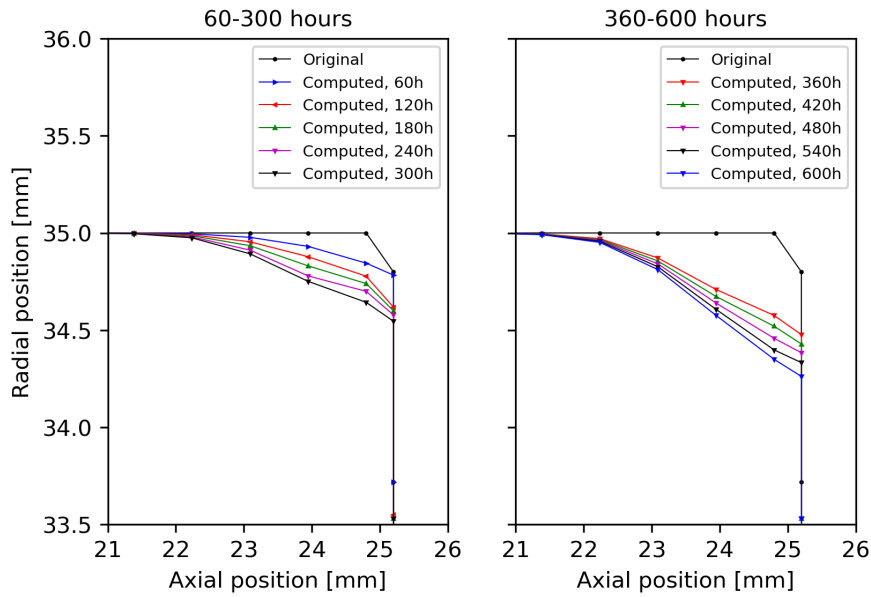
**Figure 5.6:** Eroded profiles for the channel's inner surface, for every 60 hours time-step up to a cumulative 600 hours of simulated operation.
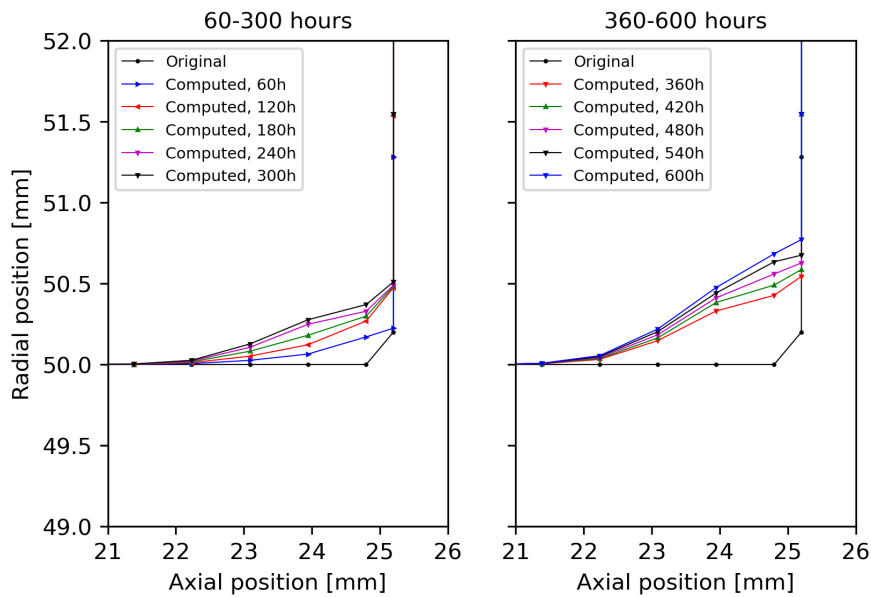


**Figure 5.7:** Eroded profiles for the channel's outer surface, for every 60 hours time-step up to a cumulative 600 hours of simulated operation.
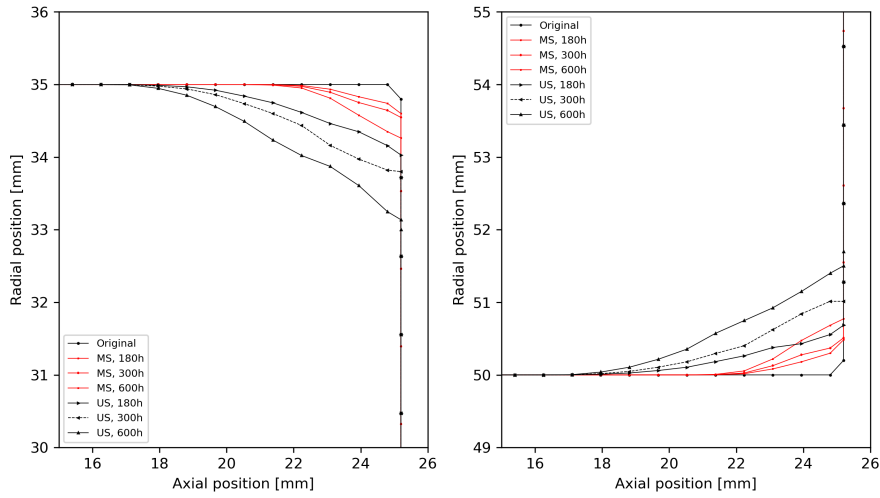
**Figure 5.8:** Eroded profiles comparison for the MS an US configurations, up to 600 hours of simulated operation.
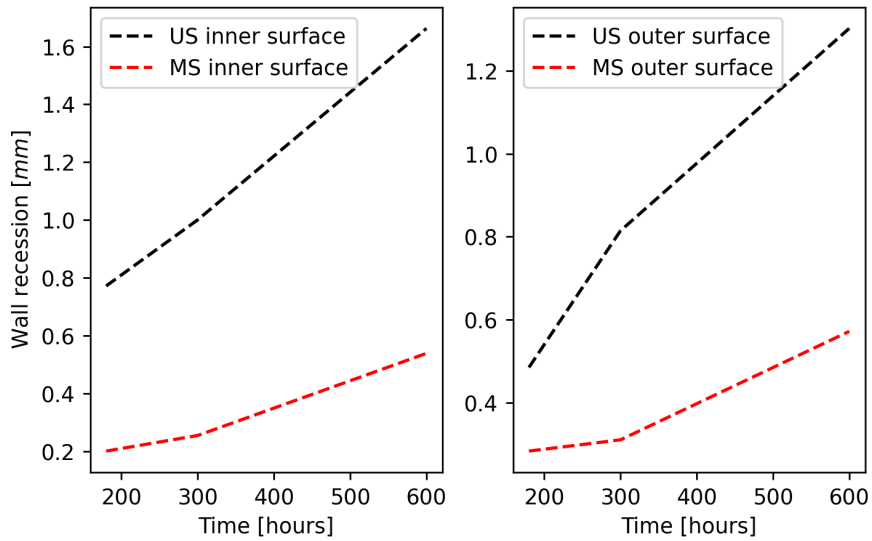


**Figure 5.9:** Wall recession, at the channel exit, comparison between $un-shielded$ and $shielded$ configuration, for both the inner and outer channel surfaces.
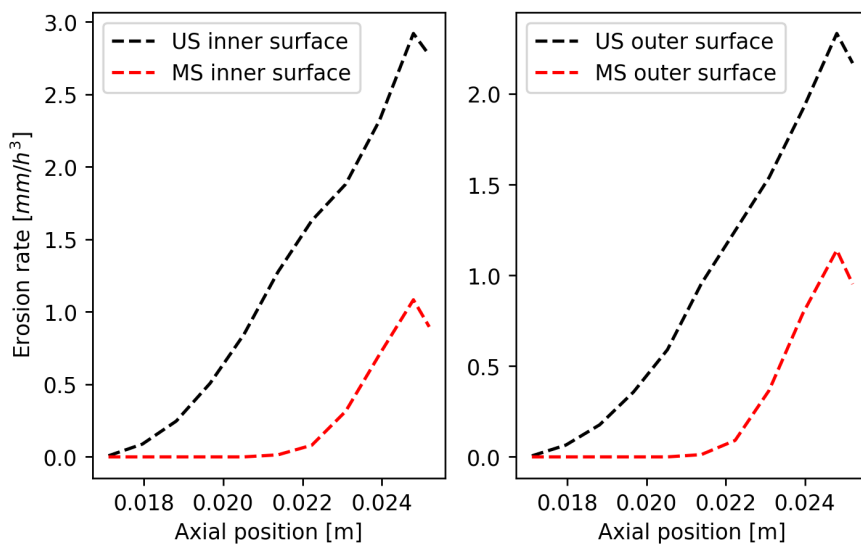
**Figure 5.10:** Erosion rates comparison between $un-shielded$ and $shielded$ configuration, for both the inner and outer channel surfaces.

## 5.2 Performance estimation

During the plasma simulations, also the performance parameters were evaluated, and are reported in Tab. 5.2. The values are similar to the ones obtained in the *US* case, but show a slight variation of a few percentage points, in particular an increase of specific impulse $I_s$ for a small decrease of thrust and total efficiency. This also seem to be in accordance with literature data ([54]).

| time [hrs] | 0 | 120 | 240 | 360 | 480 | 600 |
|---|---|---|---|---|---|---|
| $I_d$ [A] | 4.05 | 3.97 | 3.88 | 3.96 | 3.97 | 3.91 |
| $T$ [mN] | 74 | 72.9 | 70.8 | 72.4 | 72.8 | 71.1 |
| $\eta$ | 0.51 | 0.51 | 0.5 | 0.51 | 0.51 | 0.5 |
| $I_s$ [$10^3$s] | 1.69 | 1.7 | 1.69 | 1.7 | 1.7 | 1.69 |

# Chapter 6

# Conclusion and Future Steps

This thesis has described the development of an erosion model for the prediction of channel wall erosion in Hall Effect Thrusters based on experimental sputter yield data. The SPT-100 has been chosen as the reference thruster because of the amount of data available, both regarding previous erosion models and sputter yield values of borosil, the material mostly used in HETs, impacted by $Xe$ ions.

The model is implemented and coupled with the HYPICFLU code, and first the erosion model proposed by Gamero *et al.* was applied, with a slight modification accounting for the change in threshold energy. The erosion magnitude was still underestimated, by about 18% and 20% for the inner and outer surface of the channel. The point at where erosion begins is more closely predicted, differing of about 1 $mm$ from the experimental data. Later a similar model was applied, but considering a different function based on sputter yield data provided by Ranjan *et al.* The effect of temperature on sputter yield was also considered. Increasing the temperature coefficient to 5.5, which was considered to be the maximum reasonable $C_T$ value, the erosion improved by about 63% and 51% for the inner and outer surface respectively. The point at where erosion begins also improved, moving from about 23 $mm$ to 17 $mm$ for both the inner and outer surfaces.

The erosion model, improved with the temperature coefficient, was applied to the simulated SPT-100 thruster modeled by HYPICFLU, and cumulative 1020 hours of operation were simulated, with a time-step of 60 hours. The results were then compared with experimental results, showing a strong underestimation of erosion. In particular the erosion magnitude showed an underestimation of about 50% and 62% for the inner and outer surface respectively. Moreover, the point where the simulated erosion begins is shifted toward the channel exit by about 1 $mm$ for the inner surface, and 2 $mm$ for the outer surface. The underestimation of the channel erosion may suggest that the effect of temperature at low energy may be more pronounced than expected. Also, the plasma code may underestimate the velocities of ions close to the surface, which implies a lower impacting energy,

hence less erosion. Neglecting the influence of doubly charged ions and collision between ions and neutrals, which give rise to fast moving ions, may also have an effect on erosion.

A magnetically shielded configuration of the SPT-100 was also simulated, and the reduction of erosion compared to the standard SPT-100 confirmed the effectiveness of the magnetic shield in reducing the channel erosion. The erosion reduction was of 63% for the inner surface, and of about 51% for the outer surface, in accordance with literature. The point where erosion begins also shows a great improvement, moving from about 17 *mm* to 21 *mm* for both the inner and outer surfaces. The simulation for the *magnetically shielded* case, served the purpose of double checking the validity of the code in predicting the behaviour of plasma near the walls regarding erosion. Since the $MS$ version of the SPT-100 does not exist, there was no experimental data on which to compare the computational data, but the results are in accordance with what is seen in literature.

## 6.1   Future developments

This work gives rise to future possible works, both experimental and theoretical, such as:

- Further characterization of the influence of high temperature on sputter yield values. In particular would be important to know how the incidence and energy of the impacting particles influences the sputter yield at different temperatures.

- The improvement of the plasma code, accounting for doubly charged ions, and a better definition of plasma conditions near the wall.

- Coupling of the plasma code with the erosion model in order to improve the computational time and ease of work. A further, important step would be to include in the coupled model the possibility to consider the single impinging particles in time and the effect that they have on the erosion of the surface elements, with less averaged values.

In the end, as many others have said in the past, it would be great to have more data regarding the sputter yield of ceramics in the operating conditions of HETs, which coupled with a further improvement of our code, we reckon the prediction may get closer to experimental data.

# Bibliography

[1] E. Y. Choueiri. «A Critical History of Electric Propulsion: The First 50 Years (1906-1956)». In: *Journal of Propulsion & Power* 20 (2004), pp. 193–203 (cit. on p. 1).

[2] Dan M Goebel and Ira Katz. *Fundamentals of electric propulsion: ion and Hall thrusters.* Vol. 1. John Wiley & Sons, 2008 (cit. on pp. 2, 6, 15–17).

[3] *Deep space 1.* URL: https://solarsystem.nasa.gov/missions/deep-space-1/in-depth/ (cit. on p. 2).

[4] *SMART-1 lascia la Terra per un lungo viaggio verso la Luna.* URL: https://www.esa.int/Space_in_Member_States/Italy/SMART-1_lascia_la_Terra_per_un_lungo_viaggio_verso_la_Luna (cit. on p. 2).

[5] Dan Lev, Roger M. Myers, Kristina M. Lemmer, Jonathan Kolbeck, Hiroyuki Koizumi, and Kurt Polzin. «The technological and commercial expansion of electric propulsion». In: *Acta Astronautica* 159 (2019), pp. 213–227 (cit. on pp. 2, 6, 7).

[6] *What is electric propulsion?* URL: https://www.esa.int/Enabling_Support/Space_Engineering_Technology/What_is_Electric_propulsion (cit. on p. 3).

[7] Lorenzo Casalino. «Propulsione Spaziale». In: 2014 (cit. on p. 4).

[8] *In-Space Propulsion.* URL: https://www.nasa.gov/smallsat-institute/sst-soa/in-space-propulsion (cit. on pp. 4, 6, 15).

[9] Robert G Jhan. *Physics of electric propulsion.* Vol. 1. McGraw-Hill, 1968 (cit. on pp. 4–6).

[10] Stéphane Mazouffre. «Electric propulsion for satellites and spacecraft: established technologies and novel approaches». In: *Plasma Sources Science and Technology, IOP Publishing* 25 (3) (2016). DOI: 10.1088/0963-0252/25/3/033002 (cit. on pp. 6, 8).

[11] Manuel Martinez-Sanchez and James E Pollard. «Spacecraft electric propulsion-an overview». In: *Journal of propulsion and power* 14.5 (1998), pp. 688–699 (cit. on p. 8).

[12] *plasma state of matter*. URL: https://www.britannica.com/science/plasma-state-of-matter (cit. on p. 8).

[13] A Von Keudell and V Schulz-Von Der Gathen. «Foundations of low-temperature plasma physics—an introduction». In: *Plasma Sources Science and Technology* 26.11 (2017), p. 113001 (cit. on pp. 9, 10, 12, 19).

[14] Francis F Chen. *Introduction to plasma physics and controlled fusion.* Second edition. Springer, 1984 (cit. on pp. 10–14, 20).

[15] Mario Panelli, Davide Morfei, Beniamino Milo, Francesco Antonio D'Aniello, and Francesco Battista. «Axisymmetric Hybrid Plasma Model for Hall Effect Thrusters». In: *Particles* 4.2 (2021), pp. 296–324. ISSN: 2571-712X. DOI: 10.3390/particles4020026. URL: https://www.mdpi.com/2571-712X/4/2/26 (cit. on pp. 16, 26, 27, 31, 51).

[16] Jean-Pierre Boeuf. «Tutorial: Physics and modeling of Hall thrusters». In: *Journal of Applied Physics* 121.1 (2017), p. 011101 (cit. on pp. 17, 18).

[17] Tommaso Misuri, Francesco Battista, Christian Barbieri, Enrico Alessio De Marco, and Mariano Andrenucci. «High power Hall thruster design options». In: *Proceedings of the 30th International Electric Propulsion Conference (Florence), IEPC.* 2007, pp. 07–311 (cit. on p. 17).

[18] EY Choueiri. «Plasma oscillations in Hall thrusters». In: *Physics of Plasmas* 8.4 (2001), pp. 1411–1426 (cit. on p. 18).

[19] F. Valsaque G.Manfredi. «Plasma-walltransitionandsheathformation». In: *LeVide,Société française duvide* 306 (4/4) (2016), pp. 810–835 (cit. on pp. 19, 20).

[20] Vittorio Giannetti. «Plasma behaviour in a Hall effect thruster and plasma-wall interactions». PhD thesis. Università di Pisa, 2014 (cit. on pp. 21, 22).

[21] T.M.F. Vrebosch, T. Misuri, M. Andrenucci, and B.T.C. Zandbergen. «Model for Predicting the Lifetime of a Hall Effect Thruster». In: *Space Propulsion* (7-10 May 2012) (cit. on p. 21).

[22] V. S. Smentkowski. «Trends in sputtering, review». In: *Progress in Surface Science* 64 (2000), pp. 1–58 (cit. on pp. 23, 24).

[23] S. Y. M. Cheng. «Modeling of Hall thruster lifetime and erosion mechanisms». PhD thesis. Massachusetts Institute of Technology, 2007 (cit. on pp. 23, 34, 35).

[24] H. Tawara Y. Yamamura. «Energy dependence of ion-induced sputtering yields from monoatomic solids at normal incidence». In: *National Institute for Fusion Science* (1996) (cit. on pp. 24, 25, 27).

[25] Parida B. K. et al. «Sputtering yield and nanopattern formation study of BNSiO2 (Borosil) at elevated temperature relevance to Hall Effect Thruster». In: *Nuclear Inst. and Methods in Physics Research* B (2022) (cit. on pp. 25, 35, 45, 46, 60).

[26] E. Ahedo et al. «Simulation of wall erosion in Hall thrusters». In: *International Electric Propulsion Conference* September 17-20 (2007) (cit. on p. 25).

[27] E Ahedo, P Martınez-Cerezo, and M Martınez-Sánchez. «One-dimensional model of the plasma flow in a Hall thruster». In: *Physics of Plasmas* 8.6 (2001), pp. 3058–3068 (cit. on p. 25).

[28] F Taccogna, S Longo, M Capitelli, and R Schneider. «Particle-in-Cell Simulation of Stationary Plasma Thruster». In: *Contributions to Plasma Physics* 47.8-9 (2007), pp. 635–656 (cit. on p. 26).

[29] John Michael Fife. «Hybrid-PIC modeling and electrostatic probe survey of Hall thrusters». PhD thesis. Massachusetts Institute of Technology, 1998 (cit. on p. 26).

[30] F. Battista A. Petronelli M. Panelli. «Particle-In-Cell simulation of heavy species in Hall Thruster discharge». In: *Italian Association of Aeronautics and Astronautics* XXVI International Congress (2021) (cit. on p. 26).

[31] F. Battista M. Panelli. «Fluid simulation of electron discharge in Hall Effect Thruster». In: *Italian Association of Aeronautics and Astronautics* XXVI International Congress (2021) (cit. on p. 26).

[32] Nathan P Brown and Mitchell LR Walker. «Review of plasma-induced hall thruster erosion». In: *Applied Sciences* 10.11 (2020), p. 3775 (cit. on p. 27).

[33] Mishra A. Bhat S. «Prediction of liner erosion and life estimation of Stationary Plasma Thrusters using Machine Learning». In: *International Electric Propulsion Conference, Vienna, Austria* September 15-20 (2019) (cit. on p. 27).

[34] J. T. Yim. «Computational Modeling of Hall Thruster Channel Wall Erosion». PhD thesis. University of Michigan, 2008 (cit. on pp. 27, 29).

[35] Y. Garnier et al. «Low-energy xenon ion sputtering of ceramics investigated for stationary plasma thrusters». In: *Journal of Vacuum Science and Technology* 7, 3246 (1999). DOI: 10.1116/1.582050 (cit. on pp. 27, 32, 33, 36).

[36] J. F. Roussel Y. Garnier V. Viel. «Investigation of Xenon Ion Sputtering of One Ceramic Material Used in SPT Discharge Chamber». In: *26th International Electric Propulsion Conference* October 17-21 (1999) (cit. on p. 27).

[37] Manuel Gamero-Castano and Ira Katz. «Estimation of Hall thruster erosion using HPHall». In: (2005) (cit. on pp. 28, 35–37, 40, 53, 55, 64, 70).

[38] S. Y. Cheng and M. M. Sanchez. «Hybrid Particle-in-Cell Erosion Modeling of Two Hall Thrusters». In: *JOURNAL OF PROPULSION AND POWER* Vol. 24 (2008). DOI: 10.2514/1.36179 (cit. on p. 28).

[39] A. P. Yalin et al. «Sputtering Studies of MultiComponent Materials by Weight Loss and Cavity Ring-Down Spectroscopy». In: *42nd AIAA/ASME/SAE/ASEE Joint Propulsion Conference & Exhibit* July 9-12 (2006). DOI: 10.2514/6.2006-4338 (cit. on pp. 28, 32, 33).

[40] A. M. Schinder, M. Walker, and J. J. Rimoli. «3D Model for Atomic Sputtering of Heterogeneous Ceramic Compounds». In: *49th AIAA/ASME/SAE/ASEE Joint Propulsion Conference* (2013). DOI: 10.2514/6.2013-4127 (cit. on pp. 29, 31, 36).

[41] M. Ranjan, A. Sharma, A. Vaid, V. Nandalan T. Bhatt, M.G. Jamesand H. Revathi, and S. Mukherjee. «BN/BNSiO2 sputtering yield shape profiles under stationary plasma thruster operating conditions». In: *AIP ADVANCES* 6, 095224 (2016) (cit. on pp. 30, 32, 33, 39, 41, 47).

[42] V. Kim, V. Kozlov, A. Semenov, and I. Shkarban. «Investigation of the Boron Nitride based Ceramics Sputtering Yield Under it's Bombardment by Xe and Kr ions». In: *27th International Electric Propulsion Conference* 15-19 October (2001) (cit. on pp. 32, 33).

[43] R. P. Doerner, S. I. Krasheninnikov, and K. Schmid. «Particle-induced erosion of materials at elevated temperature». In: *JOURNAL OF APPLIED PHYSICS* 95 (2004). DOI: 10.1063/1.1687038 (cit. on p. 34).

[44] R. P. Doerner, M.J. Baldwin, S. I. Krasheninnikov, and K. Schmid. «High temperature erosion of beryllium». In: *Journal of Nuclear Materials* (2005), pp. 877–881. DOI: 10.1016/j.jnucmat.2004.09.025 (cit. on p. 34).

[45] K. Schmid, M.J. Baldwin, and R. P. Doerner. «Modelling of thermally enhanced erosion of beryllium». In: *Journal of Nuclear Materials* 348 (2006), pp. 294–301. DOI: 10.1016/j.jnucmat.2005.10.003 (cit. on p. 34).

[46] V. Giannetti, A. Leporini, T. Andreussi, and M. Andrenucci. «Theoretical Investigation of a 5 kW Class Hall Effect Thruster». In: *International Electric Propulsion Conference and International Symposium on Space Technology* July 4 – 10 (2015) (cit. on p. 36).

[47] V. Giannetti, T. Andreussi, A. Leporini, Denis Estublier, and M. Andrenucci. «LONG-LIFE LOW EROSION HALL EFFECT THRUSTER: MODEL AND SIMULATIONS». In: *SPACE PROPULSION* (May 2016) (cit. on p. 41).

[48] *scipy.interpolate.CloughTocher2DInterpolator*. URL: https://docs.scipy.org/doc/scipy/reference/generated/scipy.interpolate.CloughTocher2DInterpolator.html (cit. on p. 43).

[49] D. Pérez-Grande, P. Fajardo, and E. Ahedo. «Evaluation of Erosion Reduction Mechanisms in Hall Effect Thrusters». In: *Joint Conference of 30th ISTS, 34th IEPC and 6th NSAT* July 4 – 10 (2015) (cit. on pp. 52, 76).

[50] *Stationary plasma thruster SPT-100*. URL: `https://www.roscosmos.online/169.en.html` (cit. on pp. 57, 58).

[51] Richard Hofer, Ioannis Mikellides, Ira Katz, and Dan Goebel. «Wall sheath and electron mobility modeling in hybrid-PIC Hall thruster simulations». In: *43rd AIAA/ASME/SAE/ASEE Joint Propulsion Conference & Exhibit*. 2007, p. 5267 (cit. on p. 60).

[52] S. K. Absalamov et al. «Measurement of Plasma Parameters in the Stationary Plasma Thruster (SPT-100) Plume and its Effect on Spacecraft Components». In: *28th Joint Propulsion Conference and Exhibit* (1992). DOI: `10.2514/6.1992-3156` (cit. on pp. 64, 69).

[53] E. Lopedote, M. Panelli, and F. Battista. «Scaling of Magnetic Circuit for Magnetically Shielded Hall Effect Thrusters». In: *Aerotecnica Missili & Spazio* 102 (2023), pp. 109–125 (cit. on pp. 73, 74).

[54] R. Hofer, I. G. Mikellides, and I. J. Katz. «Magnetic shielding of a laboratory Hall thruster. II. Experiments». In: *Journal of Applied Physics* (2014). DOI: `10.1063/1.4862314` (cit. on p. 80).

# Ringraziamenti

Desidero ringraziare il professor Lorenzo Casalino, relatore di questa tesi, per il supporto offertomi durante questi mesi e gli ingegneri Mario Panelli e Francesco Battista per avermi dato l'opportunità di svolgere questo lavoro di tesi in collaborazione con il CIRA. Grazie a Nunzia Favaloro, per avermi messo in contatto con il reparto di propulsione spaziale in primis, e per aver fatto nascere in me l'interesse verso il CIRA. Un ringraziamento speciale va a Mario che mi ha guidato in questo percorso, aiutandomi ad entrare nel mondo della numerica senza schiantarmi contro il muro dell'incomprensione. Mi ha dato speranza, dandomi una mano a trovare la motivazione per continuare, anche quando i risultati erano molto distanti dalle aspettative. E grazie per avermi dedicato una grande quantità del suo tempo tutte le volte che ne ho avuto bisogno, per aver letto e riletto questa tesi, dandomi suggerimenti preziosi e contribuendo così, in prima persona, alla sua stesura.

Ringrazio naturalmente tutta la mia famiglia ed i miei amici, che mi hanno supportato, e *sopportato*, in questo lungo viaggio, non solo della tesi, ma di tutti gli anni passati all'università e chiusi in casa, fatto di alti e bassi. Hanno riso con me nei momenti felici e consolato nei momenti un po' più tristi.